Alma Mater Studiorum · Università di Bologna

Scuola di Scienze
Corso di Laurea Magistrale in Fisica del Sistema Terra

Role of humidity in the development and intensification of Mediterranean tropical-like cyclones (Medicanes)

Relatore:
Prof. Vincenzo Levizzani

Correlatore:
Dott. Mario Marcello Miglietta

Presentata da:
Daniele Carnevale

Sessione III
Anno Accademico 2018/2019

Alla mia famiglia

e alle nuvolette bianche

in un cielo azzurro

Abstract

In this work, two ”tropical-like cyclones” in the Mediterranean Sea, aka Medicanes, are analyzed by means of numerical simulations with the WRF model (version 4.1). Numerical simulations were carried out using the Cheyenne supercomputer at the NCAR-Wyoming Supercomputing Center (NWSC) and initialized with ERA5, the last generation meteorological reanalysis of ECMWF. These cases, which were recently analyzed in Miglietta and Rotunno (2019), are here reconsidered in order to focus on the origin of the humid low-level air that favorably preconditioned the environment where these cyclones developed. Simulations show a rather different behavior between the two cyclones. In the first Medicane, which developed over the southern Mediterranean near the coast of Libya, high humidity content was present at the low-levels already before the cyclone formation, due to the intense sea surface fluxes in the southern Mediterranean, associated with dry and cold airflow from the eastern Balkans. The second Medicane, which developed over the western Mediterranean near the Balearic Islands, strongly intensified when it benefited of the intense sea surface fluxes due to the outbreak of Tramontane and Cierzo winds near the cyclone location. Although limited to these two case studies, these results of simulation and sensitivity tests identified different environmental conditions favorable to Medicanes intensification in the western and in the southern Mediterranean, and explain why these two areas are considered as *hot spots* for the development of these phenomena. Moreover, the role of upper-level dry air intrusions in cyclones development is analyzed. Sensitivity experiments were performed where a constraint on the minimum value of relative humidity (50%) was imposed in the initial and boundary conditions. In this way, while the humidity content was affected, the strong potential vorticity anomaly, which is generally associated with dry intrusions, is not altered. For both cases, we found that the increase of humidity had the effect of anticipating the cyclone development, and of producing stronger and longer-lasting vortices.

The work is organized as follows. In the first part, the first chapter gives an overview of all families of cyclones and a detailed description of Medicanes; the second chapter illustrates the main features of Numerical Weather Prediction models (NWPs), their types of parametrizations and main implementations; the third chapter describes the tools used to accomplish the analysis, as well as the working principles of the WRF model and post-processing tools used to plot the outputs of the model. The second part concerns the description of the simulations and sensitivity experiments of the two case studies. In the third and last part are gathered further discussion and conclusions.

Sommario

In questo lavoro sono stati analizzati due casi di ”tropical-like cyclones” nel Mediterraneo, anche noti come Medicane, facendo uso di simulazioni numeriche del modello WRF (versione 4.1). Le simulazione numeriche sono state effettuate usando il supercomputer Cheyenne dell'NCAR-Wyoming Supercomputing Center (NWSC) e inizializzate con i dati di ERA5, l'ultima generazione di reanalisi meteorologiche dell'ECMWF. Questi casi, che sono stati recentemente analizzati nell'articolo di Miglietta e Rotunno (2019), sono stati riconsiderati qui per porre l'attenzione sull'origine dell'aria umida nei bassi strati atmosferici che precondiziona favorevolmente l'ambiente dove i cicloni si sviluppano. Nel primo Medicane, sviluppatosi nel Mediterraneo meridionale vicino alle coste libiche, erano presenti alti valori di umidità nei bassi strati atmosferici già prima che il ciclone si formasse, a causa degli intensi flussi superficiali dal mare nel Mediterraneo meridionale, associati ad aria secca e fredda proveniente dai Balcani orientali. Il secondo Medicane, sviluppatosi sul Mediterraneo occidentale vicino alle isole Baleari, si intensifica fortemente nel momento in cui beneficia degli intensi flussi superficiali dal mare generati dall'irruzione dei venti di Tramontana e Cierzo vicino alla zona di formazione del ciclone. Benché limitati a questi due casi studio, i risultati delle simulazioni e dei test di sensibilità hanno identificato differenti condizioni ambientali favorevoli all'intensificazione dei Medicane nel Mediterraneo occidentale e meridionale, e dimostrano perché queste due aree sono considerate come *hot spot* per la formazione di questi fenomeni. Inoltre, è stato analizzato il ruolo dell'intrusione di aria secca d'alta quota nello sviluppo dei cicloni. Sono stati effettuati test di sensibilità dove è stata posta una condizione di minimo valore di umidità relativa (50%) nelle condizioni iniziali e nelle condizioni al contorno. In questo modo, mentre viene modificato il contenuto di umidità, la forte anomalia di vorticità potenziale, che è generalmente associata ad intrusioni secche, non viene alterata. Per entrambi i casi, è stato trovato che l'aumento di umidità ha l'effetto di anticipare la formazione del ciclone, producendo vortici più intensi e duraturi.

Il lavoro è organizzato nel modo seguente. Nella prima parte, il primo capitolo dà una panoramica sulle famiglie di cicloni e una dettagliata descrizione dei Medicane; il secondo capitolo illustra le principali caratteristiche dei modelli di previsione numerica, i loro tipi di parametrizzazioni e le principali implementazioni; il terzo capitolo descrive gli strumenti usati per effettuare le analisi, come i principi di funzionamento del modello WRF e gli strumenti di post-elaborazione usati per elaborare graficamente gli output del modello. La seconda parte riguarda la descrizione dettagliata delle simulazione e delle analisi di sensibilità dei due casi studio. Nella terza e ultima parte sono raccolte ulteriori precisazioni e le conclusioni.

Contents

Abstract i

List of Figures vii

List of Tables xi

Acronyms xiii

I General introduction and overview of analysis tools 1

1 Introduction to Cyclones 3

1.1 Tropical Cyclones . . . 3

1.2 Extratropical Cyclones . . . 6

1.3 Polar Lows . . . 9

1.4 Subtropical Cyclones . . . 9

1.5 Mediterranean Tropical-Like Cyclones . . . 10

2 Models 15

2.1 Overview . . . 15

2.2 Parameterizations . . . 17

2.3 Numerical Methods . . . 21

2.4 Data Assimilation . . . 23

2.5 Ensemble Forecasting . . . 25

3 Analysis tools 27

3.1 The WRF model . . . 27

3.2 Input Data . . . 30

3.3 Post-processing tools 30

II Case studies **33**

4 Medicane Zeo **35**

4.1 Initial conditions 36

4.2 Moist air masses analysis 38

4.3 Sensitivity tests without surface fluxes 42

4.4 Dry air masses analysis 46

4.5 Sensitivity tests with addition of water vapor 49

5 Medicane Cornelia **59**

5.1 Initial conditions 60

5.2 Moist air masses analysis 62

5.3 Sensitivity tests without surface fluxes 66

5.4 Dry air masses analysis 72

5.5 Sensitivity tests with addition of water vapor 74

III Final considerations and conceptual model **81**

6 Conclusions **83**

Bibliography **89**

List of Figures

1.1 Hurricane Michael, October 10, 2018. Image take from the NOAA website [50] 4

1.2 Simplified model of the structure of a TC in the Northern Hemisphere. Images taken from the Encyclopedia Britannica [65] 5

1.3 Powerful Nor'easter off the United States Atlantic coast on March 26th 2014. Image taken from Suomi NPP satellite [25] 6

1.4 Horizontal and vertical simplified cross section of an EC 7

1.5 Simplified model of the structure of an EC, from Cloud Dynamics book [58] . 8

1.6 Schematic representation of the Norwegian model, from Bjerknes and Solberg, 1922 [2]. 8

1.7 A PL off the NW coast of Norway on April 6th 2007. Image taken from NERC receiving station [48] 9

1.8 STC Katie at east-southeast of Easter Island at 21:25 UTC, May 2nd 2015. Image taken from Suomi NPP satellite [24] 10

1.9 Medicane Numa over the Ionian Sea at 09:25 UTC, November 18th 2017. Image taken from MODIS website [45]. 11

1.10 Number of medicanes per month (total number in the period 1948–2011). Image taken from Cavicchia at al. [8] 12

1.11 Locations of all the medicanes detected for the period 1948–2011. Images taken from Cavicchia at al. [8] 12

1.12 Summary of the general locations of various cyclone types. Images taken from Hart, 2003 [29] 14

2.1 Overview of sub-grid proceses, from ECMWF website [17]. 18

2.2 Earth's energy budget, from NASA website [46]. 19

2.3 Overview of microphysic processes that take place inside clouds, from Cloud Dynamics book [58]. 20

2.4 Overview of turbulence processes that take place in the atmosphere [62] . . 21

2.5 Assimilation Scheme [9] 24

2.6 Complete description of weather prediction in terms of a Probability Density Function (PDF) [18]. 25

2.7 Example of spaghetti plot relative to 500 hPa geopotential heights of GFS [7]. 26

2.8 Ensemble tropical cyclone storm track [49]. 26

3.1 WRF Modeling System Flow Chart, from the WRF User's Guide. 28

4.1 Medicane Zeo satellite images taken from the MODIS AQUA satellite 35

4.2 Simulated trajectory of Medicane Zeo - points every 3 hours 36

4.3 Control run temperature field at 500 hPa and sea level pressure surfaces . . 37

4.4 Control run θ_e field at 700 hPa and water vapor mixing ratio at 700 hPa . . . 37

4.5 Moist air back-trajectory analysis at 950 hPa 39

4.6 Moist air back-trajectory analysis at 850 hPa 40

4.7 Moist air back-trajectory analysis at 700 hPa 41

4.8 Isobaric and geopotential height differences between the control run and the No Fluxes test 43

4.9 Integrated water vapor and water vapor mixing ratio at 1000 hPa in the control run and No Fluxes test. 44

4.10 Sea level pressure isolines in the control run and No Fluxes test 45

4.11 Sea level pressure minimum values (every 3 hours) in the control run and in No Fluxes test. 45

4.12 Dry air back-trajectory analysis at 500 hPa 47

4.13 Dry air back-trajectory analysis at 700 hPa 48

4.14 Dry air at 850 hPa. Comparison with simulation and aerosol reanalysis. . . 49

4.15 Relative humidity field at 300 hPa and θ cross section at $39°$ N for 00Z11-RH50 test. 50

4.16 Integrated water vapor with sea level pressure isolines in the control runs and RH50 tests 52

4.17 Sea level pressure surfaces in the RH50 tests. Surfaces are plotted every 2 hPa. 54

4.18 Sea level pressure minimum values (every 3 hours) in the control runs and in RH50 tests 54

4.19 Wind speed maximum values (every 3 hours) at 10 m in the control runs and in RH50 tests 54

4.20 θ_e fields at 700 hPa of control runs and RH50 tests 55

4.21 θ_e cross sections of control runs and RH50 tests 56

5.1 Medicane Cornelia images in the infrared bandwidth, from the METEOSAT-5 satellite 59

5.2 Simulated trajectory of Medicane Cornelia - points every 3 hours 60

5.3 Control run temperature field at 500 hPa and sea level pressure surfaces . . 61

5.4 Control run θ_e field at 700 hPa and water vapor mixing ratio at 700 hPa . . . 61

5.5 Moist air back-trajectory analysis at 950 hPa 62

5.6 Moist air back-trajectory analysis at 700 hPa 63

5.7 Moist air back-trajectory analysis at 950 hPa 64

5.8 Moist air back-trajectory analysis at 700 hPa 66

5.9 Isobaric and geopotential height differences between the control run and the I No Fluxes test 67

5.10 Integrated water vapor and water vapor mixing ratio at 1000 hPa in the control run and I No Fluxes test 68

5.11 Sea level pressure isolines in the control run and I No Fluxes test 69

5.12 Sea level pressure minimum value (every 3 hours) in the control run and in I No Fluxes test. Dotted part refers to simulation without surface heat fluxes. . . 69

5.13 Integrated water vapor and water vapor mixing ratio at 1000 hPa in the control run and II No Fluxes test 71

5.14 Sea level pressure isolines in the control run and II No Fluxes test. 73

5.15 Sea level pressure minimum value (every 3 hours) in the control run (solid blue line) and in II No Fluxes test (dotted+solid green line) and latent heat fluxes maximum values in the control run only (long dash line). Dotted green part refers to the sensitivity test when the heat fluxes have been turned off. 73

5.16 Dry air back-trajectory analysis at 500 hPa 74

5.17 Total suface heat fluxes with sea level pressure isolines and wind field at 1000 hPa in the control runs and RH50 tests of 4 October and cyclone simulated trajectories. 76

5.18 Sea level pressure minimum values (every 3 hours) in the control runs and in RH50 tests 77

5.19 Sea level pressure minimum values (every 3 hours) in the control runs and in RH50 tests 77

5.20 Total suface heat fluxes with sea level pressure isolines and wind field at 1000 hPa in the control runs and RH50 tests of 5 October and cyclone simulated trajectories. 78

5.21 θ_e fields at 700 hPa and cross sections of control runs and RH50 tests . . . 79

6.1 Hart's diagrams of the 00Z12-CTL run and 00Z12-RH50 test cyclones. Colors are referred to the intensity of the sea level pressure. One point every 3 hours.. . 85

6.2 Hart's diagrams of the 12Z05-CTL run and 12Z05-RH50 test cyclones. Colors are referred to the intensity of the sea level pressure. One point every 3 hours.. . 86

6.3 Conceptual model of the detrimental role of upper-level dry intrusions in the Mediterranean tropical like-cyclone formation. 87

List of Tables

1.1 Saffir-Simpson Hurricane Scale 4

2.1 Space and time scales 17

Acronyms

ABL Atmospheric Boundary Layer

AOD Aerosol Optical Depth

ARW Advanced Research WRF

BOLAM Bologna Limited Area Model

CCN Cloud Condensation Nuclei

CFL Courant–Friedrichs–Lewy condition

CISK Convective Instability of the Second Kind

CISL Computational and Information Systems Laboratory

CNR Consiglio Nazionale delle Ricerche

CPS Cyclone Phase Space

DWD Deutscher Wetterdienst Wetter und Klima aus einer Hand

EC Extratropical Cyclone

ECMWF European Centre for Medium-Range Weather Forecasts

EOS Electro-Optical System

EPS Ensemble Prediction System

ERA5 ECMWF Reanalysis 5th Generation

FDM Finite Difference Method

FT Fourier Transform

GCM General Circulation Model

GEOS-5 Goddard Earth Observing System Data Assimilation System

GFS Global Forecast System

GOCART Goddard Chemistry, Aerosol, Radiation and Transport

GrADS Grid Analysis and Display System

GRIB General Regularly-distributed Information in Binary form

HDF Hierarchical Data Format

IFS Integrated Forecasting System model

IMEX Implicit-Explicit Method

IPCC Intergovernmental Panel on Climate Change

ISAC Istituto di Scienze dell'Atmosfera e del Clima

ITCZ Intertropical Convergence Zone

IWV Integrated Water Vapor

LAM Limited Area Model

LES Large Eddy Simulations

LSM Land Surface Model

MEDICANE MEDIterranean hurriCANE

MERRAero Modern Era Retrospective analysis for Research and Applications Aerosol Reanalysis

MM5 Mesoscale Meteorological Model, Version 5

MODIS Moderate-resolution Imaging Spectroradiometer

MOLOCH Modello Locale in Hybrid coordinates

NASA National Aeronautics and Space Administration

NCAR National Center for Atmospheric Research

NCL NCAR Command Language

NERC Natural Environment Research Council

NetCDF Network Common Data Form

NHC National Hurricane Center

NMM Nonhydrostatic Mesoscale WRF Model

NOAA National Oceanic and Atmospheric Administration

NWP Numerical Weather Prediction

NWSC NCAR-Wyoming Supercomputing Center

OI Optimal Interpolation method

PBL Planetary Boundary Layer

PL Polar Low

PV Potential Vorticity

RH Relative Humidity

RRTM Rapid Radiative Transfer Model

SLP Sea Level Pressure

SSHS Saffir–Simpson Hurricane Scale

SST Sea Surface Temperature

STC Subtropical Cyclone

TC Tropical Cyclone

TD Tropical Depression

TLC Tropical-Like Cyclone

TT Tropical Transition

VAPOR Visualization and Analysis Platform for Ocean, Atmosphere, and Solar Researchers

WISHE Wind Induced Surface Heat Exchange

WMO World Meteorological Organization

WPS WRF Pre-processing System

WRF Weather Research and Forecasting model

WSM3 WRF Single-Moment 3-class scheme

WSM5 WRF Single-Moment 5-class scheme

YSU Yonsei University scheme

I General introduction and overview of analysis tools

As we got farther and farther away, the Earth dimished in size. Finally it shrank to the size of a marble, the most beautiful marble you can imagine ... seeing this has to change a man.

- James Irwin, Apollo 15

1 Introduction to Cyclones

Following the World Meteorological Organization (WMO) official terminology [64], a cyclone is *an area of low pressure, with the lowest pressure at the center, commonly referred to as a Low*. Cyclones can form all over the word: above the sea, due to the high sea surface temperature (e.g., tropical cyclones) or large temperature difference between sea surface and the air above (e.g., polar lows) or also over land, between warm and cold air masses (e.g., extratropical cyclones). Cyclones are grouped into several families with respect to the formation mechanisms and physical features. This work focuses on the MEDIterranean hurriCANEs (MEDICANEs) initial and mature phases; this kind of cyclone is relatively rare with hybrid features typical of the two main cyclone families, tropical cyclones and extratropical cyclones. In this chapter we introduce the main families of cyclones and the necessary nomenclature and terminology in order to refer to these atmospheric phenomena.

1.1 Tropical Cyclones

A tropical cyclone is a rotating storm system with a low pressure center. The most remarkable features of TCs are the presence of an ”eye” of mostly calm weather (figure 1.1), the presence of a warm core, weak vertical wind shear and an eyewall with convective cells. These cyclones mainly form over the tropical oceans near the Intertropical Convergence Zone (ITCZ), within 15° to 30° latitude degrees from the Equator in both hemispheres. The area most favorable to their formation is 10°; occasionally they may form within 5° of latitude N or S. A starting, although not physics, distinction between the tropical cyclones concerns the place of the world where they form: tropical cyclones over the North Atlantic and Northeast Pacific Oceans are called *hurricanes*, while those over the Northwest Pacific Ocean are called *typhoons* and simply *cyclones* for the rest of the world.

The typical atmosphere where the TCs develop is called the *barotropic atmosphere*: it means that the density of the fluid (the air) is a function of pressure only, so the isobaric surfaces are also surfaces of constant density. Furthermore, the isothermal surfaces coincide with isobaric surfaces. From the thermal wind equation:

$$\frac{\partial \mathbf{V}_g}{\partial \ln p} = -\frac{R}{f}\mathbf{k} \times \nabla_p T \tag{1.1}$$

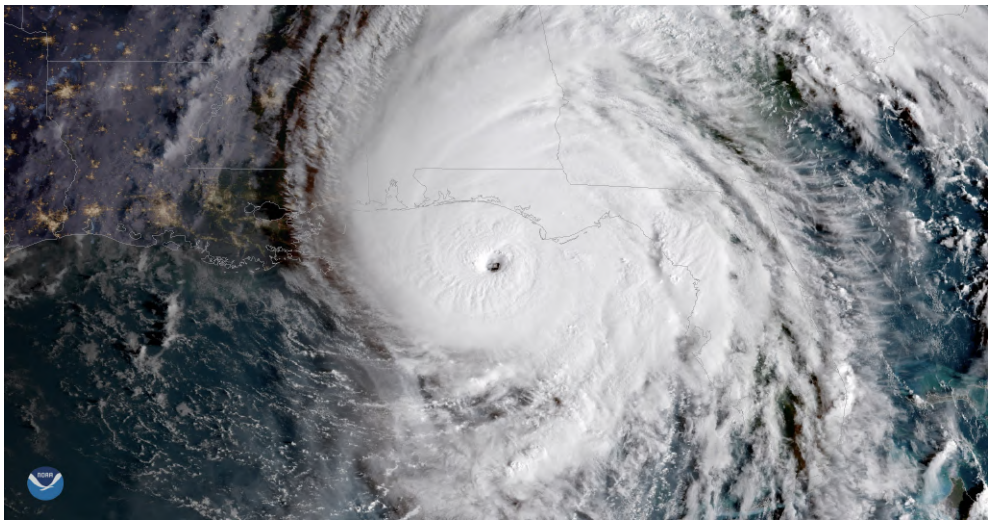

Figure 1.1 – Hurricane Michael, October 10, 2018. Image take from the NOAA website [50]

CATEGORY	WIND SPEED		
	m/s	km/h	TYPES OF DAMAGE
1	33-42	119-153	Very dangerous winds will produce some damage
2	43-49	154-177	Extremely dangerous winds will cause extensive damage
3	50-58	178-208	Devastating damage will occur
4	58-70	209-251	Catastrophic damage will occur
5	≥ 70	≥ 252	Catastrophic damage will occur

Table 1.1 – Saffir-Simpson Hurricane Scale

the geostrophic wind will not vary with depth in a barotropic atmosphere, because the term $\nabla_p T$ is zero, due to the absence of a temperature gradient along isobaric surfaces. It is not clear how tropical cyclones form but, according the observations, there are some conditions that are requested to create a favorable environment for the formation of a cyclone: sea surface temperature above 26.5° C in an ocean layer of 50 m of depth; a large vertical lapse rate; a distance generally of about 10° from the Equator so that the rotation can be derived from the Coriolis effect; finally, weak vertical shear. If the initial perturbation develops in a favorable environment, it will grow into a *Tropical Depression (TD)* and it may evolve further into a TC. The intensity and the potential impact on the human environment of the TCs is provided by the Saffir–Simpson Hurricane Scale (SSHS) (table 1.1).

Figure 1.2 shows the structure of a typical TC. The main energy sources of the TC are the sensible and latent heat fluxes from the surface of the tropical oceans and the latent heat released from the condensation of water vapor. In fact, these systems are characterized by a warm core due to the huge quantity of latent heat released by condensation. To explain how the

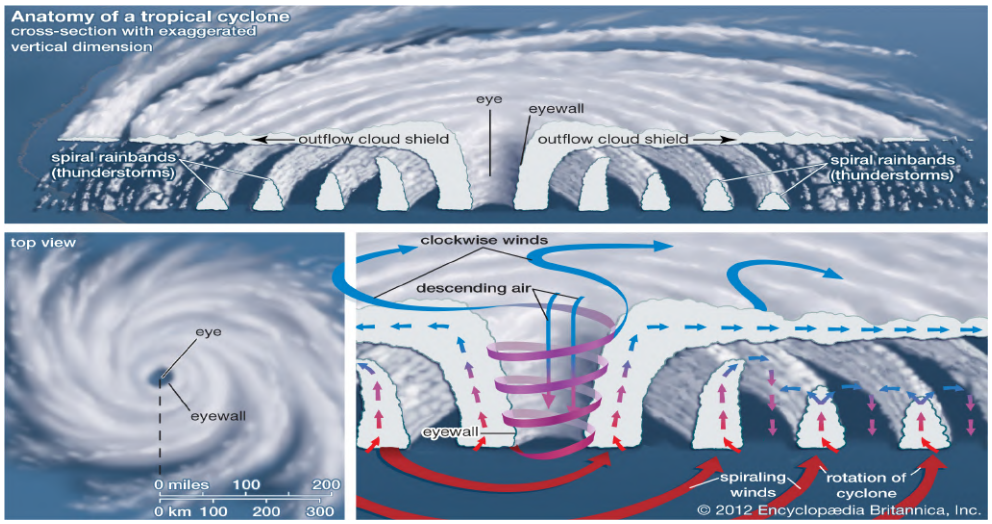

Figure 1.2: Simplified model of the structure of a TC in the Northern Hemisphere. Images taken from the Encyclopedia Britannica [65]

TCs develop and their main maintenance mechanisms, two fundamental approaches have been proposed. The first, by Charney and Eliassen, 1964 [11], is called the **Convective Instability of the Second Kind (CISK)** theory; CISK is a positive feedback mechanism that causes the amplification and the maintenance of the original disturbance. The convergence of winds toward a low pressure minimum at the surface triggers convection, which then causes cumulonimbus formation and the release of latent heat associated with the condensation of boundary-layer water vapor. Since the latent heat warms the air column, the warming causes an increased vertical destabilization of the environment and, together with the expansion of air, there is a reduction of the surface pressure. When the surface pressure decreases, a larger surface pressure gradient is formed and additional air converges towards the center of the storm. This mechanism can sustain itself until other factors, such as the advection of cold and dry air, or high wind shear act to weaken it. However, this theory does not take into account the heat fluxes from the surface. According to the CISK theory, TCs may form wherever the energy of the atmosphere can supply the ”fuel” for the cyclone formation. A second theory that takes into account the heat fluxes from the surface and completes the CISK theory was formulated by Emanuel and Rotunno in two papers [21, 59]. According to this air-sea interaction theory, aka the **Wind Induced Surface Heat Exchange (WISHE)** mechanism, a TC can be viewed as a heat engine that converts the heat stored in the water evaporated from the sea into mechanical energy. This kind of phenomenon is self-sustaining as long as it has warm water from which to gain the energy: the role of the TC vertical motion is to redistribute the heat acquired from sea surface to keep the environment locally neutral; the consequent decrease of the sea level pressure increases the intensity of the winds, promoting increased evaporation and condensation.

The result is a structure with spiral rainbands (figure 1.2) rotating in a counterclockwise

way in the Northern Hemisphere and vice-versa in the Southern Hemisphere. In a mature TC, air sinks rather than rises at the center, forming an ”eye” of clear air without wind; this feature is due to the descending air from the top of the troposphere, where the air goes down to the center becoming warmer and dissipating the clouds. The diameter of the eye is about 30-65 km while the typical size of the whole cloud structure of a TC is within mesoscale values, from 222 km to 888 km for a very large cyclone; the vertical extent reaches the tropopause, which is 15 – 18 km at tropical latitudes [6].

1.2 Extratropical Cyclones

The second main family of cyclones is formed by extratropical cyclones. As their name suggests, this class of cyclones forms outside the tropics, between 30° and 60° latitude in both hemispheres. Figure 1.3 shows a *nor'easter*, which is an extratropical cyclone in the western North Atlantic Ocean where the winds typically blow from the northeast along the US east coast. According to the glossary of the Intergovernmental Panel on Climate Change (IPCC) 5th Assessment Report, an EC is *a synoptic (of order 1000 km) storm in the middle or high latitudes having a low central pressure and fronts with strong horizontal gradients in temperature and humidity*. ECs can arise from cyclogenesis or by extratropical transition of TCs. Especially in winter, when the anticyclonic dominant patterns in summer (e.g., Azores High) lose intensity and the jet stream moves southward, cold and dry air masses can meet with warm and wet air masses, especially over the oceans. In these cases, a temperature and dewpoint gradient, called frontal zone, exists. Since the air density depends on both temperature and pressure, isobaric and isothermal surfaces are no longer parallel and the atmosphere is called *baroclinic*. The related *baroclinic instability* is of fundamental importance to understand midlatitude

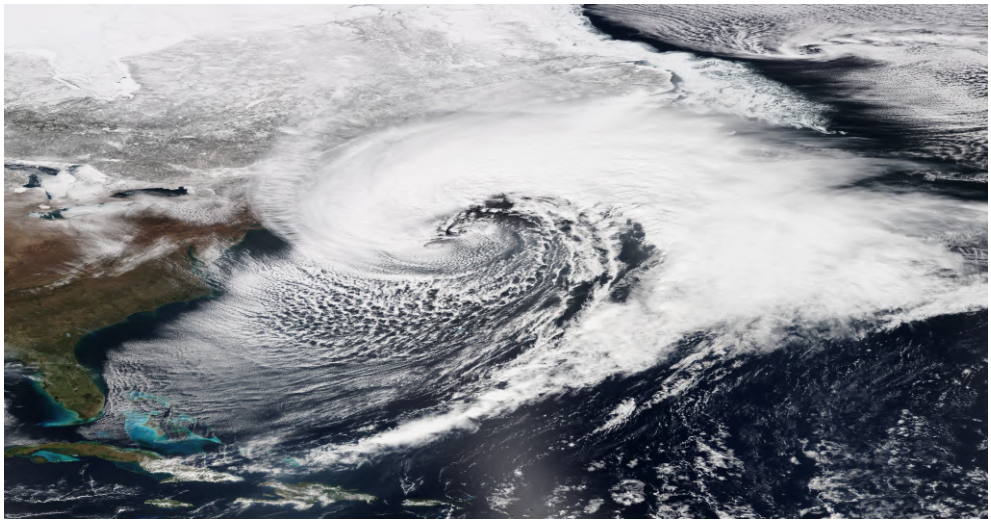

Figure 1.3: Powerful Nor'easter off the United States Atlantic coast on March 26th 2014. Image taken from Suomi NPP satellite [25]

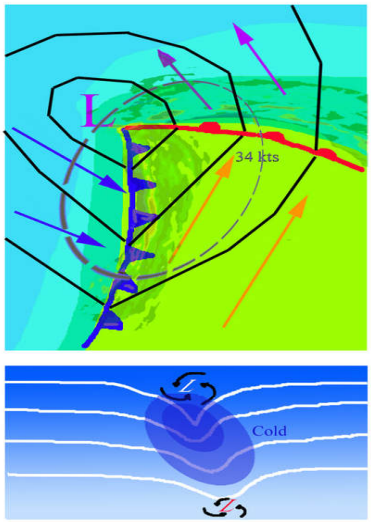

Figure 1.4: Horizontal and vertical simplified cross section of an EC

cyclogenesis. A typical environment favorable to EC development consists of an upper-level disturbance which is due to a downward undulation of the tropopause and a frontal zone in the lower-levels. In contrast to a barotropic atmosphere, in a baroclinic environment the geostrophic wind generally has vertical shear, related to a meridional temperature gradient by the thermal wind equation (equation 1.1). The presence of a jet stream in the upper level implies vorticity at its sides. The upper-level disturbance has an effect on the lower level flow such that a low (high) pressure is generated below a region of upper-level divergence (convergence). The circulation induces two regions of large thermal gradient (cold and warm fronts), rotating around the cyclone center. In the mature stage, the cold front reaches the warm front. The reason why the cold front is faster than the warm front is not trivial, because several dynamical and thermodynamic effects compete. However, in a first approximation, the heavier, denser, cold air can push the warmer, lighter air ahead of the cold front out of its way much more easily than the warm air (which is lighter and tends to move above the cold air) can push the cold air ahead of the warm front. The cold front wedges under the warm front: thus, warm and wet air is violently displaced (figure 1.5). The warm front in the upper levels wraps around the pressure minimum, which occurs in the later stages of the cyclone lifetime, while cold air blows into the minimum from lower levels. The stationary presence of both cold and warm fronts in the vicinity of the minimum takes the name of *occluded front*. The most intense precipitation phenomena are located just ahead of the cold front, while stratiform and lighter precipitation are found in the warm section.

One of the main differences between TCs and ECs is that the latter have an asymmetric and tilted cold core. In figure 1.4 are represented, in a very simplified way, a horizontal (upper figure) and a vertical (lower figure) section of an EC. In the lower figure, the white lines are geopotential heights at fixed pressure. To explain why ECs have a cold-core, we can use the hypsometric equation 1.2:

$$\Phi(z_2) - \Phi(z_1) = g_0 \left(Z_2 - Z_1\right) = R \int_{p_2}^{p_1} T d(\ln p) \tag{1.2}$$

where $\Phi(z)$ is the geopotential, $Z \equiv \frac{\Phi}{g_0}$ is the geopotential height (in the troposphere Z is numerically almost identical to the geometric height z). Equation 1.2 states that the variation in geopotential with respect to pressure depends only on temperature. Hence, the thickness of an atmospheric layer between two isobaric surfaces is proportional to the mean temperature of

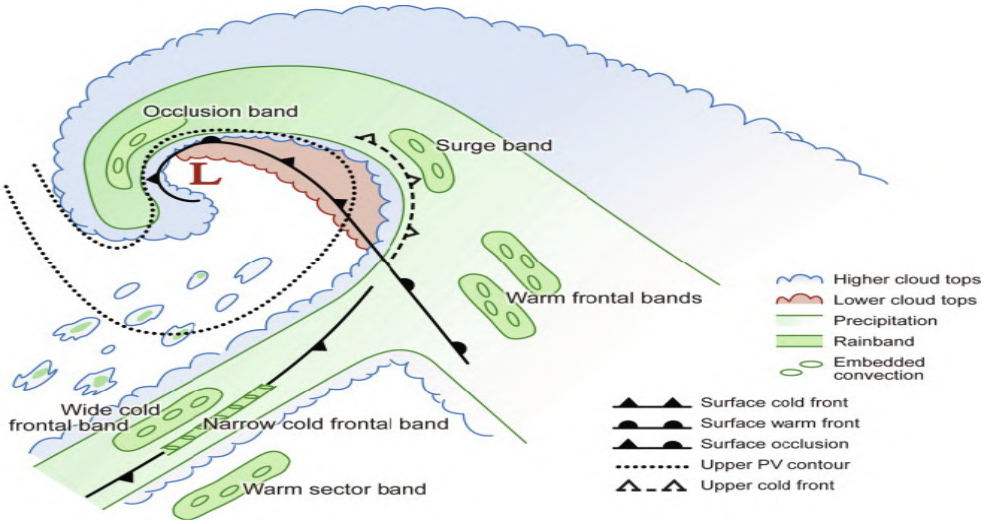

Figure 1.5 – Simplified model of the structure of an EC, from Cloud Dynamics book [58]

the layer. Thus, referring to the lower panel in figure 1.4, closely spaced geopotential isolines mean colder air.

The development and dynamics of ECs are quite complicated with respect to TCs and some models (e.g. the Norwegian model [1] - figure 1.6 or the Shapiro-Keyser model [60]) have been proposed to explain the extratropical cyclone life cycle. An interesting feature of ECs is the formation, in its later stages, of a region of warm air near the pressure minimum, called the *warm seclusion*. This area may have an eye-like feature, significant pressure falls and strong convection. These features look like the main characteristics of TCs. In the Mediterranean Tropical-Like Cyclones section, we will see that the warm seclusion may promote tropical-like features, such as a warm core and the presence of an "eye".

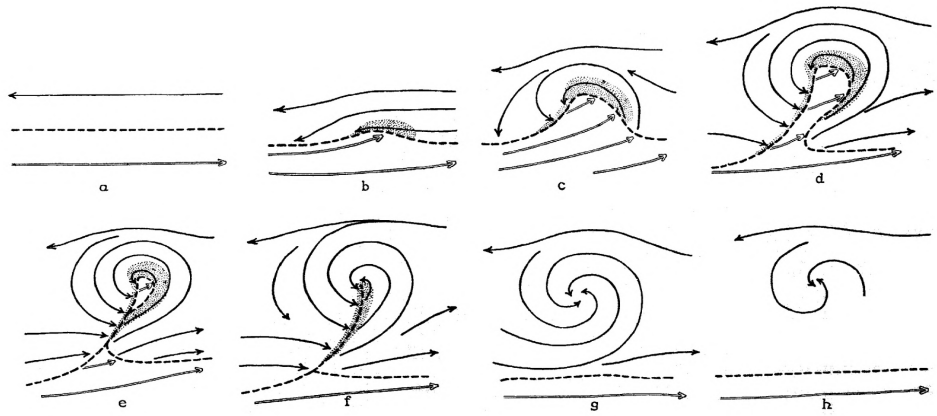

Figure 1.6 – Schematic representation of the Norwegian model, from Bjerknes and Solberg, 1922 [2]

1.3 Polar Lows

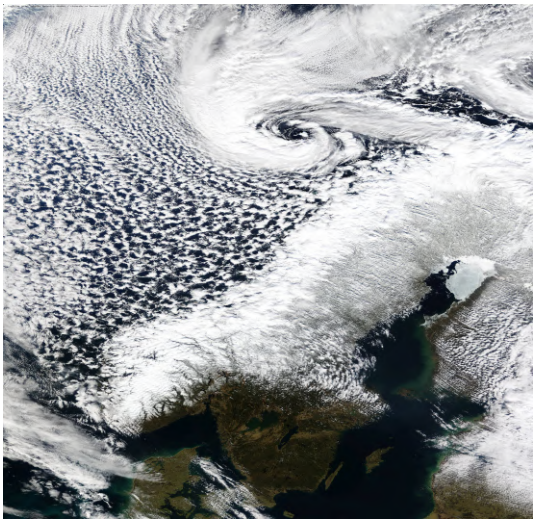

Figure 1.7: A PL off the NW coast of Norway on April 6th 2007. Image taken from NERC receiving station [48]

Businger and Reed, 1989 [4] define a Polar Low (PL) as *any type of small synoptic- or subsynoptic-scale cyclone that forms in a cold air mass poleward of major jet streams or frontal zones and whose main cloud mass is largely of convective origin*. In the early stage of formation, PLs can form a comma-shaped structure that is very similar to that of ECs. In their mature stage, PLs assume a Tropical-Like Cyclone (TLC) structure, with clouds surrounding a cloud-free "eye" and a warm core (Emanuel and Rotunno, 1988 [59]), which has given rise to the use of the term *Arctic hurricane* to describe some of the most active lows, as in figure 1.7. Due to the large values of the Coriolis parameter in the polar regions, PLs have smaller diameters than those of TCs. Reale and Atlas, 2001 [56] noted that in the Mediterranean TLCs latent-heat fluxes are much stronger than sensible-heat fluxes, while in the PLs latent and sensible fluxes are normally comparable. The underlying causes of polar lows are a combination of baroclinic and barotropic instabilities, which means that its energy derives from both the horizontal temperature gradient and the relatively warm ocean waters with respect to the cold air above; similarities with both TCs and ECs put PLs into a *hybrid cyclones category* and a rigorous formation and classification theory is still the subject of research.

1.4 Subtropical Cyclones

Following the definition of the National Hurricane Center (NHC), a STC is *a non-frontal low pressure system that has characteristics of both tropical and extratropical cyclones*. These hybrid cyclones generally form from an EC that moves toward subtropical latitudes above warm waters or when a cold upper level low is moving in over the subtropics, below 50° latitude in both hemispheres; because of the presence of cold air in the initial disturbance, STCs need lower sea temperatures than do TCs (around 23°C) to trigger deep convection. While the origin of a STC is mainly due to baroclinic instability and is characterized with an initial cold core center, in its mature stage, if the subtropical storm remains over warm waters for several days, it may sustain itself mainly through barotropic processes and acquire a warm core, as in a TC.

These storms have generally larger horizontal cloud extents with respect to TCs, weaker convection and a less symmetric wind field. Unlike traditional TCs, where the strongest winds are concentrated around the center (where the thunderstorm activity is more intense as well), in STCs these two features are displaced far from the center of circulation. If the maximum sustained winds are greater than or equal to 18 m/s they are called subtropical storms. The most famous STCs are: the *Australian east coast lows*, which affect the south coast of the island, the *Kona storms* which are a type of seasonal cyclone near the Hawaii, and the MEDICANEs.

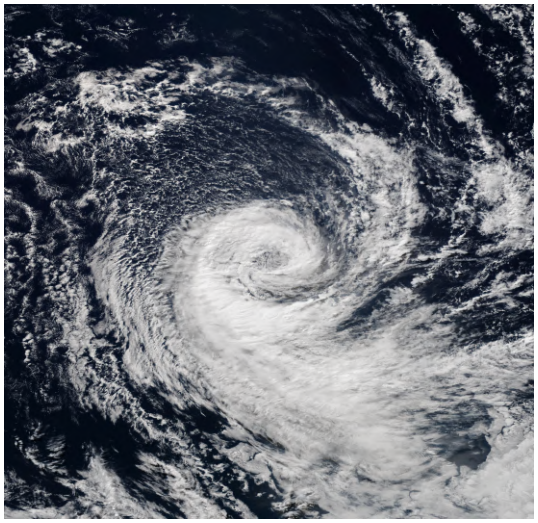

Figure 1.8: STC Katie at east-southeast of Easter Island at 21:25 UTC, May 2nd 2015.
Image taken from Suomi NPP satellite [24]

1.5 Mediterranean Tropical-Like Cyclones

These types of cyclone, often unofficially referred to *MEDICANEs* or Mediterranean TLCs, are meteorological phenomena observed over the Mediterranean Sea, that can occasionally reach category 1 on the Saffir-Simpson scale. There is no official meteorological definition of medicane, but the term is often used to describe a deep area of low pressure characterized by a warm core, deep convection around the pressure minimum, strong winds and thunderstorm activity that sometimes has the appearance of a hurricane. Figure 1.9 shows Medicane Numa after peak intensity, where the presence of an "eye", typical feature of a TC, is clearly visible over the Ionian Sea. MEDICANEs form a small class of subtropical cyclones, extract available potential energy through baroclinic processes in the early stages, as in an EC, but they receive some or most of their energy from condensational heating, as do TCs in their mature stage. Therefore, MEDICANEs form by Tropical Transition (TT), which is the dynamic and thermodynamic transformation of an EC into a TC.

The first studies of this type of cyclone are from Ernst and Matson, 1983 [22] and Rasmussen and Zick, 1987 [54], where the first satellite images showed the similarity with Atlantic hurricanes. Triggering mechanisms for the MEDICANEs are not yet well understood, but some aspects have been studied. MEDICANEs develop in the western and central Mediterranean basin, a geographic area surrounded by several mountain ranges (e.g., Alps, Pyrenees, Atlas Mountains); convection may be promoted by orographic lift (Buzzi and Tibaldi, 1978 [5]) or lee cyclogenesis (Moscatello at al., 2008 [44]). The Mediterranean basin is also a highly baroclinic region: ECs forming due to wind vertical shear over the sea may, occasion-

ally, create a favorable environment for mesoscale vortexes similar to hurricanes (Reale and Atlas, 2001 [56]); in that circumstance, if surface heat fluxes from the Mediterranean Sea are intense enough to provide moist air, convection will sustain itself, so that the environment becomes more barotropic and tropical features may eventually appear, due to diabatic heating of the midtroposphere.

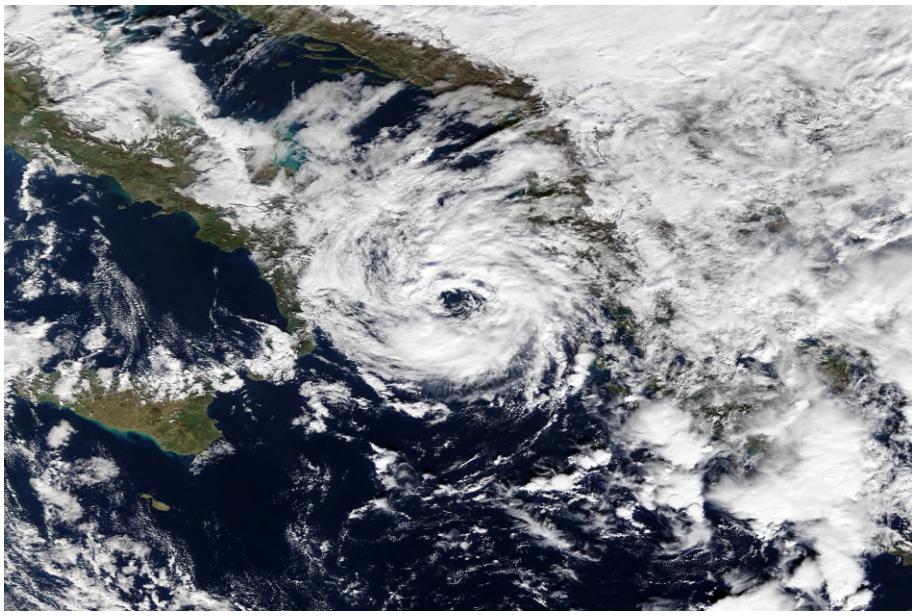

Figure 1.9: Medicane Numa over the Ionian Sea at 09:25 UTC, November 18th 2017. Image taken from MODIS website [45]

One of the most relevant differences in the MEDICANEs formation process with respect to that of TCs is the role of precursors in the higher troposphere. MEDICANEs generally form in correspondence to a deep upper-level cold cut-off low that destabilize the atmospheric column (Homar et al., 2003 [31], Moscatello et al., 2008 [44], Emanuel, 2005 [20]). This circumstance preferentially occurs during fall or early winter (figure 1.10), i.e. when the dominant summer anticyclonic pattern loses intensity and troughs from the polar vortex can reach southern regions, finding relatively warm and moist air below. So the main source of potential energy to trigger convection is the thermodynamic disequilibrium between the atmosphere and the underlying sea. A majority of MEDICANEs forms generally over two regions: the western Mediterranean north of the Balearic Islands and west of Sardinia and Corsica, and the Ionian Sea between Sicily and Greece down to Libya (figure 1.11). The frequency of MEDICANEs occurrence is extremely low, 1.57 ± 1.30 events per season, as such they can considered as rare events (Cavicchia at al., 2012 [8], Nastos et al., 2018 [47]).

Beside this remarkable difference with respect to TCs, surface-heat fluxes play the crucial role to allow the formation and especially the intensification of MEDICANEs; as in the case of TCs, the mechanism of air–sea interaction, expressed in the WISHE theory, is crucial for TLCs intensification. Part of the present work will show that if the sensible and latent heat fluxes from

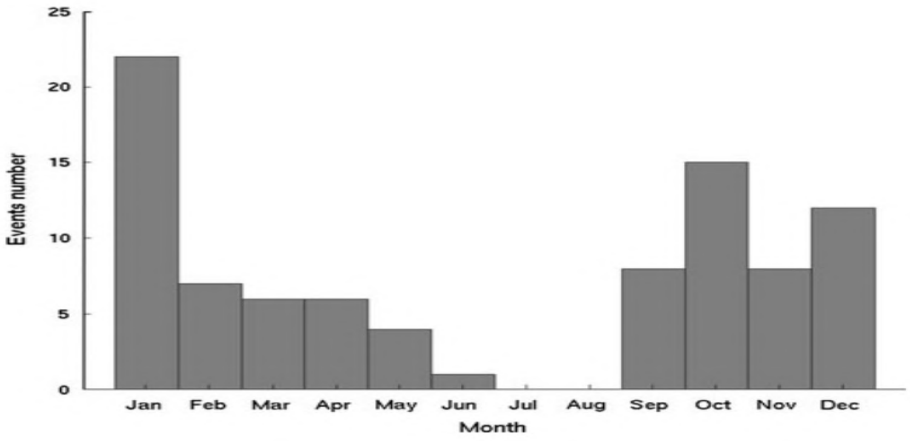

Figure 1.10: Number of medicanes per month (total number in the period 1948–2011). Image taken from Cavicchia at al. [8]

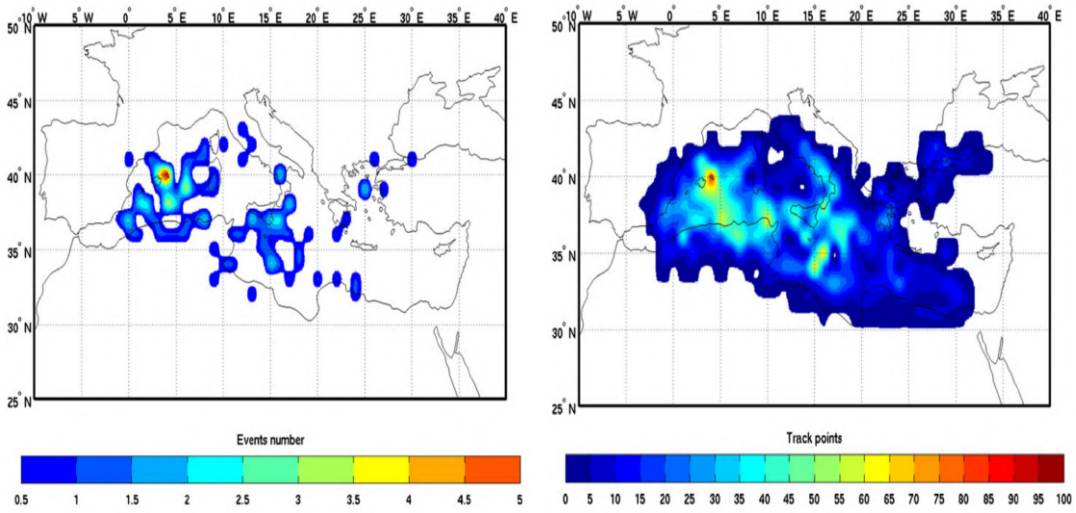

(a) Genesis density (first location in the track) per 1° × 1° box.

(b) Track density per 1° × 1° box.

Figure 1.11: Locations of all the medicanes detected for the period 1948–2011. Images taken from Cavicchia at al. [8]

the sea are turned off during the numerical simulation, the cyclone will not form at all. This fact is confirmed by several studies (Pytharoulis et al., 2000 [52], Miglietta et al., 2011 [40], Tous and Romero, 2012 [63] and others). A couple of recent papers (Fita and Flounas, 2018 [26]; Mazza et al., 2017 [38]) have raised some doubts concerning the mechanism of two Mediterranean TLCs, supporting the idea that the warm-air seclusion in the extratropical cyclone's inner core may be sufficient to explain the presence of a deep warm, core structure. Miglietta and Rotunno, 2019 [42] performed sensitivity experiments for the two TLCs without latent-heat release and/or sea-surface fluxes, showing that the air–sea interaction and the latent heating due to convection are necessary in order to explain the intensification of both cyclones,

and suggesting a key role for the WISHE mechanism in the cyclone development. However, the importance of air-sea interaction appears to be case dependent.

Another noteworthy similarity between MEDICANEs and TCs formation concerns the role of the Sea Surface Temperature (SST). Several papers focused on the SST: sensitivity tests performed by Fita et al., 2007 [27] and Miglietta at al., 2011 [40], Pytharoulis et al., 2018 [53] show that the cyclone loses intensity and typical tropical features disappear if the SST is progressively reduced with respect to the control run.

Concerning the classification algorithm, a unique and objective method to identify and classify a cyclone as MEDICANE does not exist. To understand the various types of synoptic-scale cyclones in a unified framework, Hart, 2003 [29] proposed a cyclone classification algorithm called Cyclone Phase Space (CPS), or *Hart's diagram*. The CPS assesses cyclone types objectively based on their geometric and thermal symmetry structure, once identified in atmospheric gridded datasets, such as reanalysis and model simulations: a TC is a deep warm-core, symmetric cyclone, whereas an EC is a deep cold-core, asymmetric cyclone. An STC is intermediate between a TC and an EC, since it has a shallow warm-core (a warm core in the lower troposphere, but a cold core in the upper troposphere) structure (Evans and Guishard, 2009 [23]). The CPS describes the cyclone phase using three parameters:

- the *storm-motion-relative 900-600 hPa thickness asymmetry across the cyclone within 500-km radius*:

$$B = h\left(\overline{Z_{600} - Z_{900}}|_R - \overline{Z_{600} - Z_{900}}|_L\right) \tag{1.3}$$

  where Z is isobaric height, R indicates right of current storm motion, L indicates left of storm motion, the overbar indicates the areal mean over a semicircle of radius 500 km, and h takes a value of +1 for the Northern and −1 for the Southern Hemisphere;

- the *cyclone thermal wind parameter* in the lower troposphere, defined as the vertical derivative of horizontal height gradient between 900 and 600 hPa:

$$\frac{\partial(\Delta Z)}{\partial \ln p}\bigg|_{900}^{600} = -\left|V_T^L\right| \tag{1.4}$$

  where $\Delta Z = Z_{MAX} - Z_{MIN}$ is the cyclone height perturbation and it is evaluated within a radius of 500 km, consistent with the radius used for the calculation of B; L means *"lower"*;

- the *cyclone thermal wind parameter* in the upper troposphere, defined as the vertical derivative of horizontal height gradient between 600 and 300 hPa:

$$\frac{\partial(\Delta Z)}{\partial \ln p}\bigg|_{600}^{300} = -\left|V_T^U\right| \tag{1.5}$$

  where ΔZ is the same as for the calculation of $-\left|V_T^L\right|$; U means *"upper"*.

Hart proposes also thresholds on the values of these parameters to distinguish between warm- and cold-core structures. He states that a cyclone has a warm core if:

- $B < 10$ m
- $-\left|V_T^L\right| > 0$
- $-\left|V_T^U\right| > 0$

This CPS provides an objective classification of the cyclone phase, *"unifying the basic structural description of tropical, extratropical, and hybrid cyclones into a continuum"* (Hart, 2003 [29]). Transitions between cold- and warm- core structure can be objectively identified, including extratropical transition, tropical transition, warm seclusions and the development of hybrid cyclones, all of which are summarized in figure 1.12.

This classification algorithm was used in the last few years by Gaertner et al., 2008 [28] in a future scenario of climate change over the Mediterranean region, by Chaboureau et al., 2012 [10], readapting the radius of the circles for the calculation of the diagram for Mediterranean storms to 200 km, and by Miglietta et al., 2011 [40] and 2013 [41], readapting the radius of the circle respectively to 100 km and to the extent of the warm core anomaly at 600 hPa for the MEDICANEs. Through this approach Miglietta et al., 2013 [41] drafted a list of tropical-like cyclones events in the Mediterranean region. Picornell et al., 2014 [51] used shallower depths for MEDICANEs, taking into account that their vertical extension, which is more limited compared to TCs.

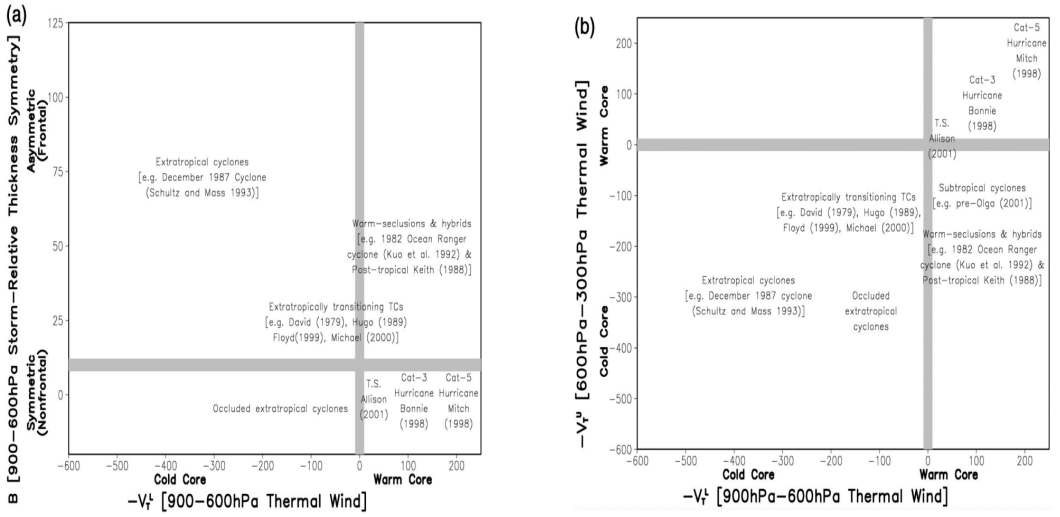

(a) $-V_T^L$ vs B (b) $-V_T^L$ vs $-V_T^U$

Figure 1.12: Summary of the general locations of various cyclone types. Images taken from Hart, 2003 [29]

2 | Models

2.1 Overview

Generally speaking, *a model is a mathematical, physical and chemical representation that can diagnose the past or present, or attempts to predict the future, state of a real system*. A weather-prediction model solves the primitive equations based on current physical and chemical knowledge. The first attempt to solve those equations was due to L. F. Richardson, however his 6h surface pressure tendency prediction was very unrealistic. The solutions of Richardson's equations contain not only slow-moving waves but also high-velocity phenomena, such as sound and gravity waves; these kinds of waves tend to amplify and produce "noise" obscuring more relevant meteorological phenomena. This problem can be solved with an appropriate approximation of the primitive equations based on the time and length scales of the relevant phenomena, as we will see later. Another problem was the lack of knowledge of initial conditions: according to V. F. K. Bjerknes [3], weather prediction is mainly an **initial-value problem**; thus, it is necessary to know with great precision both the laws governing atmospheric motions and the physical and thermodynamic state of the atmosphere at a certain initial time. Fortunately, improvements in physical knowledge, the systematic use of atmospheric soundings for the analysis of the atmosphere and the increase in computer processing power have allowed the improvement of weather prediction, which is now approaching the theoretical limit of two weeks foreseen by E. N. Lorenz [36]. Nowadays, meteorological models can be grouped in two main classes:

- **General Circulation Models (GCMs)**, like the USA GFS, European Integrated Forecasting System model (IFS) or the GLOBO model developed by the Italian Consiglio Nazionale delle Ricerche (CNR). This kind of model covers the whole atmosphere, describing synoptic systems with an approximate horizontal resolution of tens of km. They are run operationally every day to provide forecasts of meteorological fields at medium range (< three weeks) and their output can be used as initial and boundary conditions for the following class of models;
- **Limited Area Models (LAMs)**, like WRF, the Bologna Limited Area Model (BOLAM) (which is hydrostatic) or the Modello Locale in Hybrid coordinates (MOLOCH) (which

is nonhydrostatic; the last two were both developed by CNR), cover a smaller part of the atmosphere (e.g., part of a continent or one region). These models are the best choices to make an accurate prediction in a local area, since, compared to GCM, they have a finer grid spacing that can reach up to few km or even hundreds of meters. Generally, LAMs are run only for short-range, forecast for example, BOLAM model provides operational forecast within a range of 3 days with 8.3 km grid spacing. LAMs are forced by GCM, so their outputs are not independent of the large-scale fields used to force these models. The extension and the resolution of the LAM domain are a compromise between the need to properly represent small-scale features and to use a finite amount of computational power. These types of models are used to predict mesoscale or α–microscale weather systems.

2.1.1 Prognostic models

All prognostic models (that is, where time is an explicit variable) predict future state of systems, knowing initial conditions of the atmosphere. First of all, they cover the atmosphere with a 3D grid covering the whole globe (GCM) or a limited area (LAM) with a suitable horizontal and vertical spacing. The following equations, in the form taken from the book *An Introduction to Dynamic Meteorology* [30], have to be solved:

$$\frac{D\,\mathbf{U}}{D\,t} = -2\boldsymbol{\Omega} \times \mathbf{U} - \frac{1}{\rho}\nabla\, p + \mathbf{g} + \mathbf{F}_r \qquad \text{Momentum Equations} \qquad (2.1)$$

$$\frac{1}{\rho}\frac{D\,\rho}{D\,t} + \nabla \cdot \mathbf{U} = 0 \qquad \text{Continuity Equation} \qquad (2.2)$$

$$c_v \frac{D\,T}{D\,t} + L\frac{D\,q}{D\,t} + p\frac{D\,\alpha}{D\,t} = \dot{Q} \qquad \text{Energy Conservation Equation} \qquad (2.3)$$

$$\frac{D\,q}{D\,t} = \dot{P}_q \qquad \text{Humidity Conservation Equation} \qquad (2.4)$$

$$p\alpha = R_d\, T_v \qquad \text{State equation} \qquad (2.5)$$

where $\boldsymbol{\Omega}$ is the angular velocity of Earth, ρ is the density, p is the environment pressure, $\mathbf{g}$ is the gravity term, $\mathbf{F}_r$ are the frictional forces, c_v is the specific heat of dry air at constant volume, T is the environment temperature, L is the latent heat, q is the water vapor mixing ratio, α is the specific volume, $\dot{Q}$ is the diabatic heating rate, $\dot{P}_q$ is the sum of all the source and sink rate terms of q in the atmospheric column, R_d is the gas constant for dry air and T_v the virtual temperature. Some of previous equations can be simplified according to the typical space and time

scale one wants to investigate, indicated in Table 2.1, where the last row refers for Large Eddy Simulations (LES). Scale analysis leads to hydrostatic (equation 2.6) and geostrophic approximation (equations 2.7 and 2.8) in synoptic scale. The hydrostatic approximation is generally used in GCM and LAM with grid spacing greater than 7-8 km.

Models	Horizontal Scale	Vertical Scale	Range Time
Climate models	100 km	400 m	100 years
GCM	20 km	200 m	10 days
LAM	4 km	100 m	2 days
Cloud model	500 m	100 m	1 day
LES	50 m	50 m	5 hours

Table 2.1 – Space and time scales

$$\frac{\partial p}{\partial z} = -\rho g \qquad \text{Hydrostatic approximation} \qquad (2.6)$$

$$v_g = \frac{1}{f\rho}\frac{\partial p}{\partial x} \qquad \text{Zonal component of geostrophic wind} \qquad (2.7)$$

$$u_g = -\frac{1}{f\rho}\frac{\partial p}{\partial y} \qquad \text{Meridional component of geostrophic wind} \qquad (2.8)$$

2.2 Parameterizations

Since horizontal resolution is limited, some phenomena cannot be resolved by models because their typical space scale is smaller than grid spacing or their behaviors are too complex to be physically represented by a simplified process; this kind of phenomenon is said to be subgrid scale and needs to be statistically analyzed. The procedure of expressing the effects of subgrid processes is called *parameterization*.

2.2.1 Radiation

As it is well known, the energy of the Sun is the main source for the atmospheric motions. An indication of this at the largest scales is the differential heating from the poles to equator that drives the mean global circulation. The local energy budget depends on many factors: the solar zenith angle, the albedo of the surface, the temperature of the emitting body and its emissivity, the local cloud type fraction, etc. An accurate representation of radiative processes and their time and space variations are essential for weather and climate research.

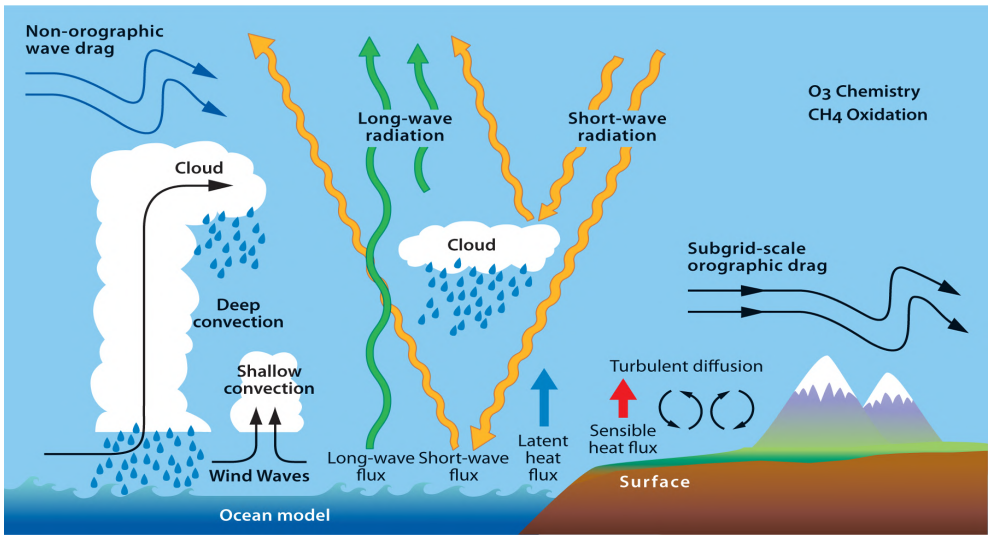

Figure 2.1 – Overview of sub-grid proceses, from ECMWF website [17].

Radiation is divided into short and long-wave components: short-wave directly comes from the Sun and it can be absorbed by surfaces or atmospheric gases or scattered back, while long-wave radiation is emitted by surfaces and the Earth's atmosphere. If the incoming radiation is absorbed or reflected from an object, it will depend on the radiative properties of the object itself (type of soil, type and concentration of a certain gas, etc.) and the frequency of the radiation. In the same way, the amount of emitted long-wave radiation will depend on the radiative properties of the object. Computationally, it is too expensive for a meteorological model to deal with all the lines of the spectrum of radiation; thus, the spectrum is split into different frequency bands, where each of these has different capacity of interaction with the atmospheric gasses and particles (like, water vapor, ozone and carbon dioxide). Types of radiative transfer model that have been used in this work are: the Rapid Radiative Transfer Model (RRTM) scheme (Mlawer et al., 1997) [43] for long-wave radiation and the Dudhia scheme (Dudhia, 1989) [15] for short-wave radiation.

2.2.2 Convection

In the atmosphere, the phenomenon of convection can occur when an air mass is heated by an energy source (the Sun) and its density becomes smaller than the surrounding air, so that the air parcel may ascent: in this case we refer to *free convection*. Instead, when an air mass is forced up either by a colder air mass moving in the low-levels (e.g., mid-latitude fronts) or by orographic lift, we refer to *forced convection*. In any case, convection probably represents the most important physical process to parameterize in order to forecast weather. Especially free convection occurs on small horizontal scales, of the order of km or less. Convection can also be distinguished in shallow convection or deep convection: the first, where updraft velocities are of the order of few m/s, generally forms low stratified clouds, with an horizontal extent

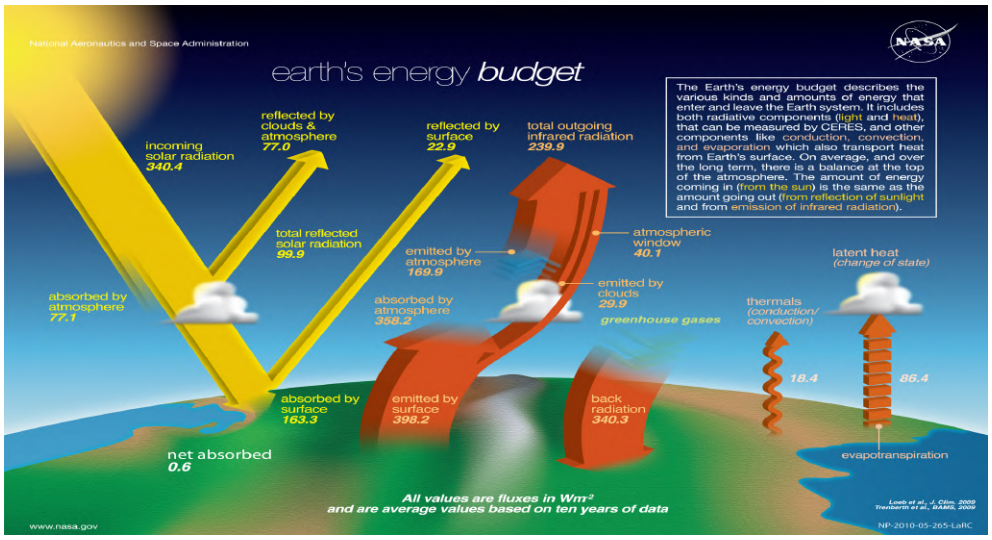

Figure 2.2 – Earth's energy budget, from NASA website [46].

much greater than the vertical; the second occurs when surface heating is very strong or in presence of deep atmospheric instability (e.g., cumulonimbus formation); in this case, impressive vertical cloud structures are formed, even passing above the tropopause. Deep convection is associated with the most intense and dangerous weather phenomena; to predict these events with a suitable advance time for civil protection purposes, the models do not need only an high horizontal resolution but a high vertical resolution as well. The Kain-Fritsch (Kain, 2004) [35] scheme has been used for cumulus parameterization; this scheme reproduces local shallow and deep convection, furthermore it allows the resolution of the vertical flux due to updraft and downdraft motions that are not solved on the grid.

2.2.3 Land-Surface models

Land Surface Models (LSMs) use quantitative methods to simulate the biogeochemical, hydrological and energy cycles at the Earth surface–atmosphere interface. A LSM must provide four quantities to the atmospheric model: surface sensible-heat flux Q_H, surface latent-heat flux Q_E, upward long-wave radiation Q_L (or skin temperature and surface emissivity) and upward (that is, reflected) short-wave radiation Q_S (or surface albedo). These fluxes provide lower boundary conditions for vertical motions. To parameterize land effects, a 5-layer thermal diffusion scheme (Dudhia, 1996) [16] has been used here.

2.2.4 Clouds

A cloud is defined as an aggregate of very small water droplets, ice crystals, or a mixture of both, with its base above the Earth surface. With the exception of certain types that have no direct effects on weather, clouds are confined to the troposphere. They are formed mainly as the result of vertical motion because of air heating, in forced ascent over high elevations, or in the

large-scale vertical motion associated with depressions and fronts. At temperature below 0 °C, cloud particles frequently consist entirely of supercooled water droplets down to about −10 °C in the case of layer clouds and to about −25 °C in the case of convective clouds. At temperature between supercooled limits and about −38.5 °C, clouds are "mixed" in water droplets and ice crystals. Below −38.5 °C, clouds are mainly compound of ice crystals. Formation and dynamics of the clouds are strictly connected with chemical processes: except from really low temperatures (that can be reached in the upper troposphere), formation of embryonal cloud droplets occurs through specific atmospheric aerosols called Cloud Condensation Nuclei (CCN). The latter are minute solid particles suspended in the atmosphere, on which water vapor condenses at typical supersaturated relative humidity values detected inside clouds. This kind of formation is called heterogeneous nucleation (as opposed to homogeneous nucleation, which occurs below −38.5 °C); in this case, water vapor does not need a solid surface to induce condensation. After formation, droplets can grow in many different ways, which in fact are not all known or completely understood, to become drops, raindrops, graupels or hail. Cloud parameterization has to consider all kinds of processes, many of which are governed by stochastic equations, that take place at microscopic scales. In order to parameterize microphysics processes, in this work we have been used the WRF Single-Moment 5-class scheme (WSM5) (Hong, Dudhia and Chen, 2004) [32], a slightly more sophisticated version of the WRF Single-Moment 3-class scheme (WSM3), that allows for mixed-phase processes and super-cooled water.

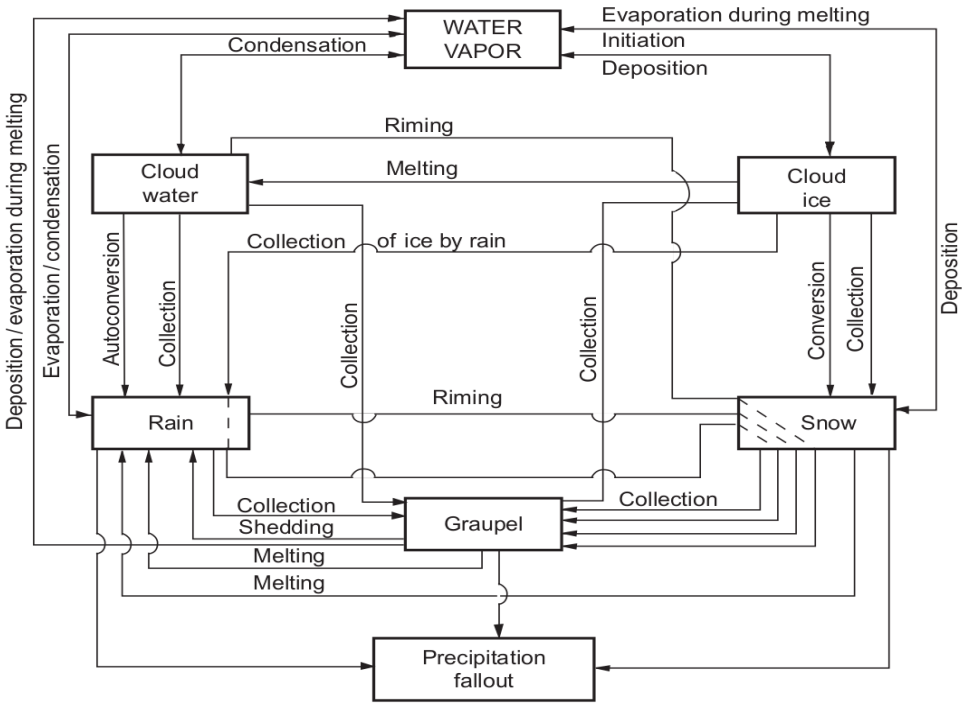

Figure 2.3: Overview of microphysic processes that take place inside clouds, from Cloud Dynamics book [58].

2.2.5 Turbulence

The Atmospheric Boundary Layer (ABL), or Planetary Boundary Layer (PBL), is that portion of the atmosphere affected by the presence and properties of the underlying surface and biosphere. The depth h of the PBL varies typically from 10 m to 10^3 m, in relation to the type of surface, hour of the day and season. Compared to the longer time scale involved in phenomena that affect the whole atmospheric depth from the surface the to tropopause, this tiny layer of atmosphere has a time scale of variations of one hour. PBL phenomena are essentially turbulent, and hard to mathematically analyze, due to the stochastic behavior of mixing processes. There is not a complete and unified theory of turbulence but different approaches to study it, as Reynolds or Kolmogorov theories with countless empirical formulas. The Yonsei University scheme (YSU) (Hong, Noh and Dudhia, 2006) [33], a non-local-K scheme with explicit entrainment layer and parabolic K profile in unstable mixed layer, has been used to parameterize the PBL, while the revised Mesoscale Meteorological Model, Version 5 (MM5) Monin-Obukhov scheme (Jiménez et al., 2012) [34] has been chosen to parameterize the surface layer.

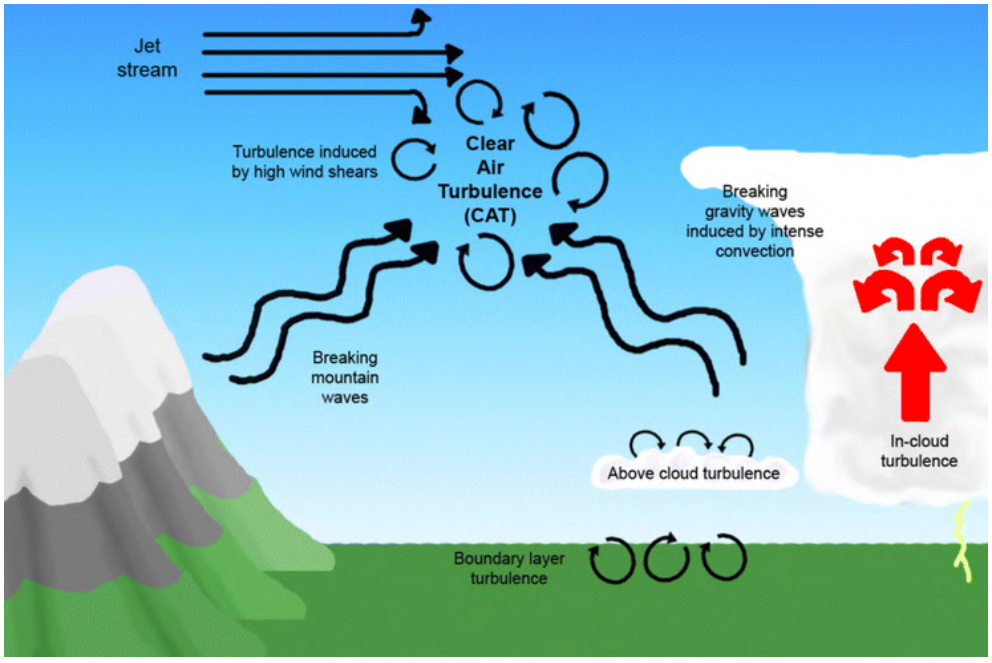

Figure 2.4 – Overview of turbulence processes that take place in the atmosphere [62]

2.3 Numerical Methods

The goal of numerical forecast is to determine the future state of the atmosphere, knowing its initial state, with appropriate numerical approximations. In addition to a good knowledge of the current state of the atmosphere, we need a closed system of equations, numerical methods to integrate them and, naturally, powerful supercomputers. A problem with the complete set

of equations is that they contain waves-like solutions (i.e., sound and gravity waves) that are not of meteorological interest and produce "noise" that obscures the relevant meteorological fields. As anticipated earlier, appropriate approximations can be used as a filter to obtain a set of equations without the presence of sound and/or gravity waves.

Even the equation of barotropic vorticity, the simplest prognostic equation, is nonlinear and has a complicated solution; other equations contain terms depending on $\mathbf{U}^2$ and cannot be solved analytically. A way used in almost all Numerical Weather Prediction (NWP) models to solve these difficulties, is to use the so called Finite Difference Methods (FDMs). FDMs are discretization methods for solving differential equations by approximating them with difference equations, in which derivatives are approximated with finite difference of desired order of accuracy. If $\Psi(x)$ is the solution of the differential equation in a certain interval, we can divided the interval in J sub-intervals of length dx, so called grid spacing; now we can approximate $\Psi(x)$ with $J+1$ values:

$$\Psi_j(x) = \Psi(j\,dx)$$

If dx is much smaller than the length scale in which $\Psi(x)$ varies, $\Psi_j(x)$ will be a good approximation for $\Psi(x)$. A greater accuracy can be achieved with a smaller dx, but this implies an increase in the number of points, or an increase in the degree of the polynomial used for the approximation (which may lead to very complicated formulas). Approximate solutions must be limited on the numerical domain, otherwise numerical methods become unstable. The Courant–Friedrichs–Lewy condition (CFL) sets strong limitations on the Courant number $\sigma = c\frac{dt}{dx}$. In the case of explicit methods, σ must be less or equal 1, thus, grid spacing and integration time have to be chosen carefully. Explicit methods solve the equation in a foreward way, knowing the current approximate value of the solution and moving it on in time and space. Implicit methods, instead, find a solution by solving the equation involving both the current and future state of the system. Numerical analysis shows that implicit methods are absolutely stable, therefore the solution does not grow with time. Incidentally, implicit methods are more complicated to deal with because they have to solve the equation in all grid point directions simultaneously and leads to the calculation of huge matrices, which is historically one of the most time-consuming computational problems. Moreover, implicit methods cannot be used if there are nonlinear terms: a solution is to use Implicit-Explicit Methods (IMEXs), where nonlinear terms are treated in an explicit way.

Another method used in some meteorological models (like the glsecmwf IFS) is the spectral method; the variations of space variables are expressed as a function of finite series of orthogonal functions. In case of sphere-like domains as the Earth, spherical harmonics are used as orthogonal functions. At low resolution (that is, for GCMs), spectral methods are more accurate than FDM (e.g., a single Fourier component can realistic represent one Rossby wave, while many points are required for FDM). On the other hand, spectral methods have

serious computational problems when there are many components of spherical harmonics because of nonlinear nature of the advection terms. This problem can be solved using the Fourier Transform (FT) that allows us to switch from spherical harmonics's wave numbers to latitude-longitude grids at each time step; the advection term can be treated on this new grid, avoiding to calculate spectral function products.

Current NWP models are based on approximate primitive equations. Vertical coordinates are generally terrain-following. Anyway, surface is not flat and pressure will change: to avoid complication due to vertical-dependent boundary conditions, the so called σ coordinate is used:

$$\sigma = \frac{p - p_T}{p_S - p_T} \tag{2.9}$$

where p is pressure, p_T is the pressure at the top of the model and p_S is the mean sea level pressure; $\sigma = 1$ at the ground and 0 at the top. Thus, σ condition is 1 everywhere on the lower surface, even if there is an obstacle. Primitive equations in σ coordinates will be:

$$\frac{D\mathbf{U}}{Dt} + f\mathbf{k} \times \mathbf{U} = -\nabla\Phi + \sigma\nabla \ln p_s \frac{\partial \Phi}{\partial \sigma} \qquad \text{Momentum Equation} \tag{2.10}$$

$$\frac{\partial p_s}{\partial t} + \nabla \cdot (p_s \mathbf{U}) + p_s \frac{\partial \dot{\sigma}}{\partial \sigma} = 0 \qquad \text{Continuity Equation} \tag{2.11}$$

$$\frac{\partial \Phi}{\partial \sigma} = -\frac{R\theta}{\sigma}\left(\frac{p}{p_0}\right)^k \qquad \text{Hydrostatic Equation} \tag{2.12}$$

$$\frac{\partial \theta}{\partial t} + \mathbf{U} \cdot \nabla\theta + \dot{\sigma}\frac{\partial \theta}{\partial \sigma} = \frac{J}{c_p}\frac{\theta}{T} \qquad \text{Thermodynamic Equation} \tag{2.13}$$

$$\frac{Dq_v}{Dt} = P_v \qquad \text{Moisture-Continuity Equation} \tag{2.14}$$

where $\mathbf{U} = (u, v)$, Φ is the geopotential, θ is the potential temperature, p_0 is 1000 hPa, q_v is the mixing ratio and P_v the source term. Primitive equations are solved on a particular type of grid on which all of the variables are not predicted at all of the points but rather are interspersed at alternate points. This kind of grid is called "staggered". Vertical staggered grid is telescopic, that is, there is higher level density near the ground and lesser near the top of the model, due to the high resolution needed in the lower atmosphere.

2.4 Data Assimilation

Data assimilation is a mathematical discipline that seeks to optimally combine theory with observations. Objective of atmospheric data assimilation is to produce a regular and physically

consistent representation of the state of the atmosphere from a heterogeneous array of in situ and remote instruments, which sample the atmosphere imperfectly and irregularly in space and time. Data assimilation extracts the signal from noisy observations, interpolates in space and time and reconstructs state variables that are not sampled by the observation network.

One of the major problems of NWP is the knowledge of initial conditions. Observations cannot be used directly but they need to be modified to be dynamically valid. In NWP, data assimilation combines observation of meteorological variables, such as temperature and atmospheric pressure, with prior forecast in order to initialize numerical forecast models.

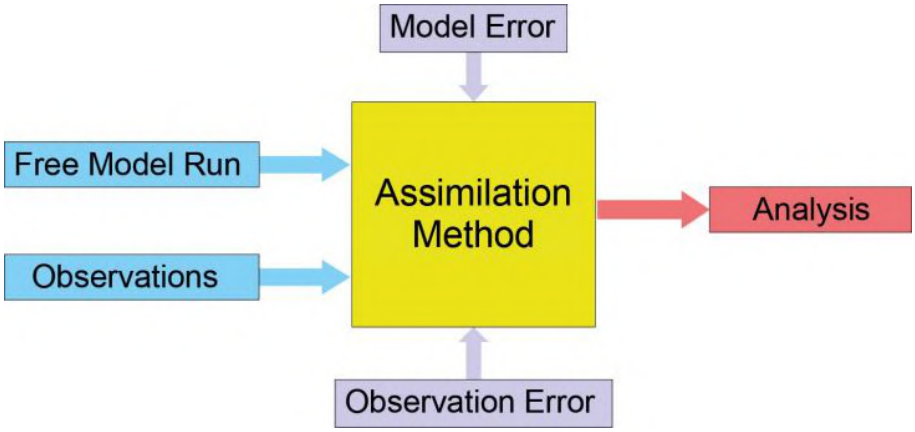

Figure 2.5 – Assimilation Scheme [9]

Optimal Interpolation methods (OIs) calculate optimal values of weights to minimize the error of the variance. The generic formula is:

$$\mathbf{x}_a = \mathbf{x}_b + \mathbf{W}\left(\mathbf{y} - \mathbf{H}\left(\mathbf{x}_b\right)\right) \tag{2.15}$$

where $\mathbf{x}_a$ is the result of analysis, $\mathbf{x}_b$ is the forecast (or background) vector, $\mathbf{y}$ is the observation vector, $\mathbf{H}$ is a non-linear operator that converts the background in observations (e.g., radiative transfer equations) and $\mathbf{W}$ is the matrix of weights, whose elements are functions of background and observation errors. OIs directly solve the problem.

An alternative approach is to iteratively minimize a cost function $J(x)$ that solves the same problem. These are called variational methods, such as 3D or 4D variational data assimilation: 3D-VAR is formally equivalent to OI methods, while 4D-VAR method uses the model to create a sequence of states that fit optimally with background and the observations on a time frame. In 4D-VAR, observations are included from following and previous time steps into the analysis. The main advantages of 4D-VAR are the consistency with the governing equations and the implicit links between variables; on the other hand, these methods are computationally very expensive and the model result may be too constrained.

2.5 Ensemble Forecasting

Ensemble Forecasting is a method used to evaluate and quantify the two usual sources of uncertainty in forecast models, that is, the errors introduced by the use of imperfect initial condition amplified by the chaotic nature of the atmosphere equations, and errors introduced because of imperfections in the model formulation, such as approximate methods and different types of parameterizations. In practice, several forecasts of similar models are run in parallel with slightly different initial conditions; this will produce a predicted ensemble spread and the amount of it should be related to the uncertainty of the forecast (see figure 2.6). In other words, this approach is used to estimate of the probability density of the forecast. These kinds of forecasts are called Ensemble Prediction Systems (EPSs). In a good ensemble, "truth" looks like a member of the ensemble.

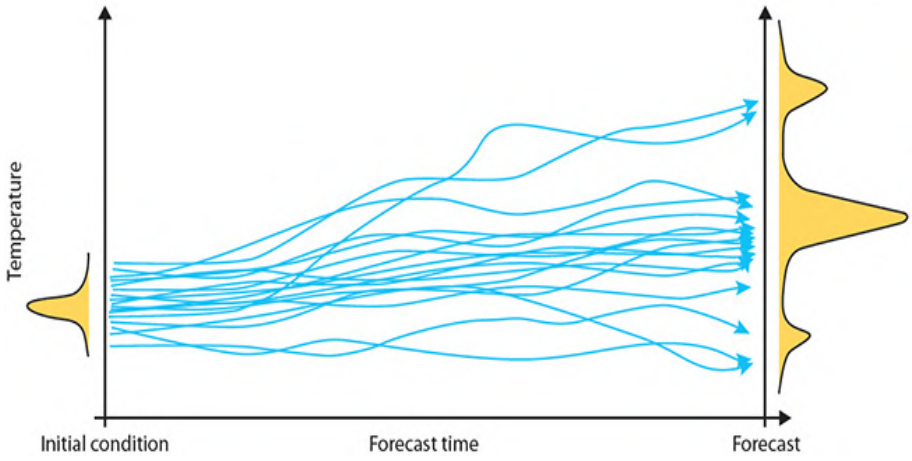

Figure 2.6: Complete description of weather prediction in terms of a Probability Density Function (PDF) [18].

In an EPS, the average value of the ensemble will give us a forecast generally better than forecasts of each member of the ensemble; in fact, some models could see a meteorological pattern, like a cut-off, but the average over all the runs could eliminate that pattern. The spread of the members will give us an estimate of the forecast accuracy: the smaller the spread, the greater the reliability.

There are different ways to visualize the ensemble forecast information. One of these, is the so called the *spaghetti plot* called in this way because isolines appear like noodles. When isopleths are close together, the reliability of the EPS is high and viceversa. In Figure 2.7, the lower-right plot is a clear example of the intrinsic chaotic behavior of the atmosphere. The longer is the forecast horizon, the larger will be the spread among the different members. Figure 2.8 shows the ensemble track prediction of Hurricane Sandy for the days afterwards October 26, 2012: the cone contains the probable path of the storm center and it spreads out in the following days.

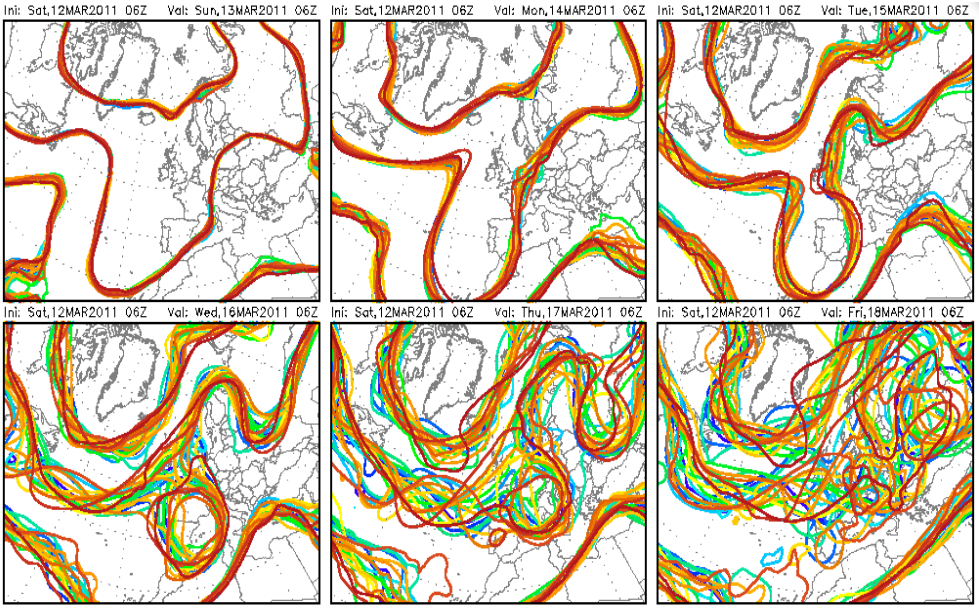

Figure 2.7 – Example of spaghetti plot relative to 500 hPa geopotential heights of GFS [7].

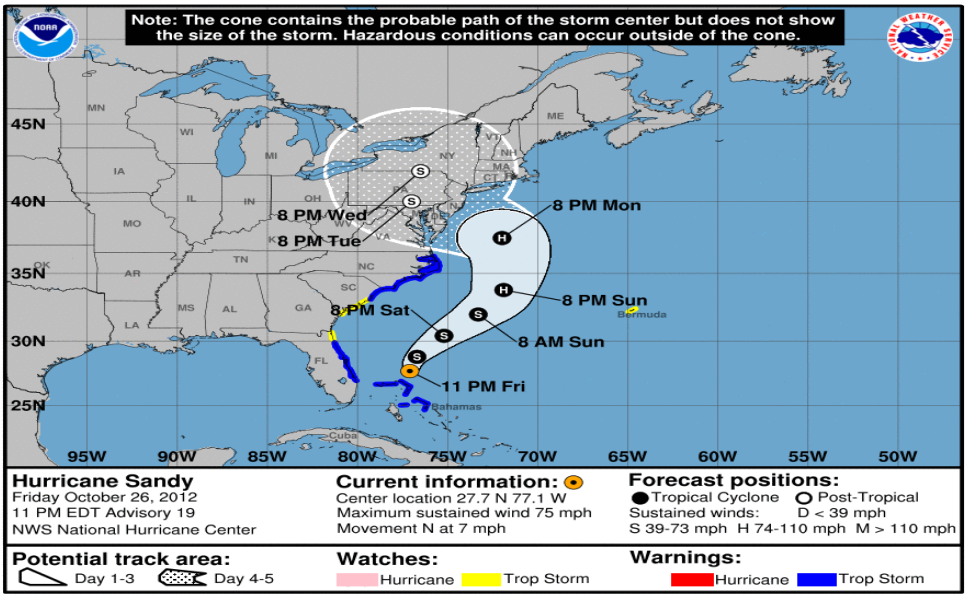

Figure 2.8 – Ensemble tropical cyclone storm track [49].

3 Analysis tools

In this chapter, tools used in this research will be introduced and discussed.

3.1 The WRF model

The WRF model is a mesoscale open-source NWP system developed since the 1990s by the National Center for Atmospheric Research (NCAR) and NOAA among other partnerships. It can be used both for local or global predictions with suitable case-dependent time-space resolution. It is developed with two dynamical core: the Advanced Research WRF (ARW) and the Nonhydrostatic Mesoscale WRF Model (NMM); the first is mainly built for atmospheric research and real/idealized simulations and the other for operational forecasting. WRF solves the governing Euler equations of motion in non-hydrostatic way (but a hydrostatic option is also included) with terrain-following vertical coordinates (recently changed to hybrid) based on a normalized atmospheric pressure. The Arakawa C-grid is used to stagger the grid points in space, so that temperature and horizontal wind fields are horizontally shifted; similarly, the vertical component of velocity is vertically staggered with respect to the other fields. The model uses the Runge-Kutta 2^{nd} and 3^{rd} order time integration schemes, and 2^{nd} to 6^{th} order advection schemes in both the horizontal and vertical. WRF model simulations for a real case require two steps:

- WRF Pre-processing System (WPS), that creates the meteorological and numerical grid and defines the initial and the lower boundary conditions on the grid (for an idealized case it is not necessary to configure it);
- ARW model, the essence of the model that solves the atmospheric equations.

In this work ARW 4.1 was used [61]. Another part, not strictly connected to ARW run but surely very important, is the post-processing step. This part allows the conversion of WRF output into graphs, meteorological maps or even 3D data visualizations. Utilities used for the analysis are described in the following sections.

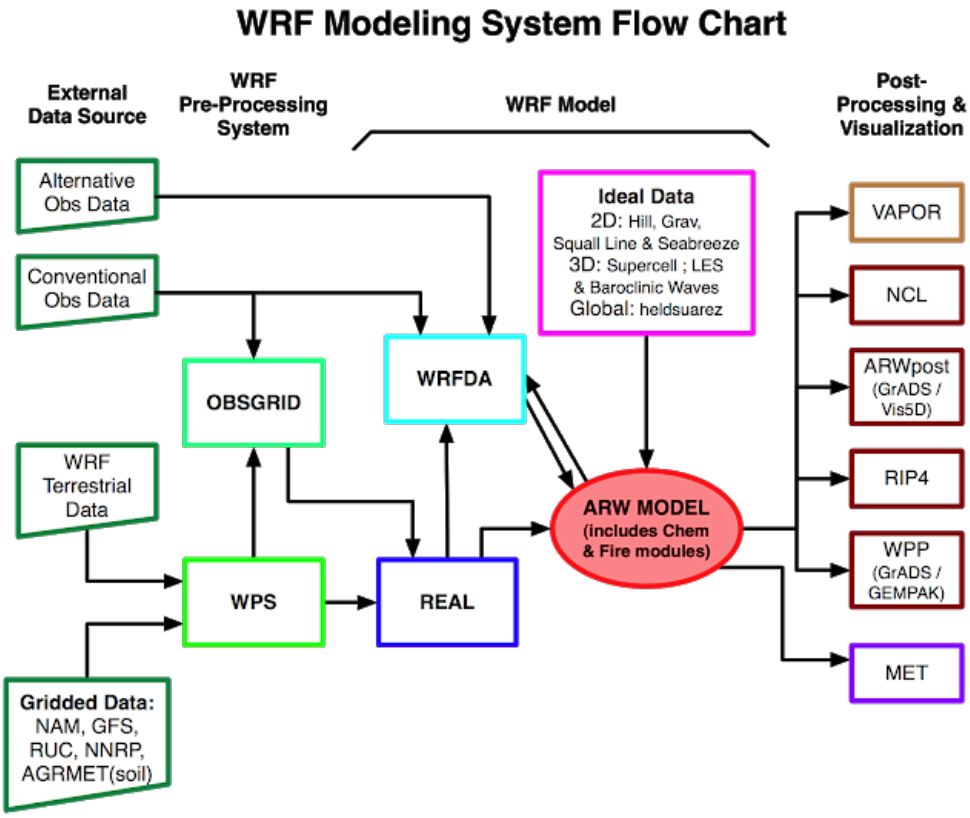

Figure 3.1 – WRF Modeling System Flow Chart, from the WRF User's Guide.

3.1.1 WPS

The purpose of the WPS is to define the domain and interpolate terrestrial data to it. Furthermore, it interpolates meteorological data from a global model (European Centre for Medium-Range Weather Forecasts (ECMWF) or GFS) to our simulation domain, preparing initial data for ARW analysis. WPS is composed of three different programs:

- `geogrid.exe` that produces the domain including static (time invariant) geographical data. Geogrid files contain topographic and map projection data. Geogrid output file are generally indicated with the name `geo_em.d01.nc`, where `d01` stands for the external domain and output is in Network Common Data Form (NetCDF) format;
- `ungrib.exe` that extracts meteorological fields from General Regularly-distributed Information in Binary form (GRIB) files, taken from ECMWF or GFS website. GRIB is a WMO standard file format storing regularly distributed grids. `ungrib.exe` uses Vtables (Variable tables, e.g. `Vtable.GFS` or `Vtable.ECMWF`) to know which fields have to be extracted. The format of the name of the ungrib output files is `FILE:YYYY-MM-DD_HH`, where YYYY-MM-DD_HH indicate year, month, day and hours respectively;
- `metgrid.exe`, that interpolates meteorological fields horizontally within the domain using data extracted from geogrid and ungrib steps. Metgrid output files have names

like `met_em.d01.YYYY-MM-DD_HH.nc`.

`namelist.wps` file is where WPS's programs read the parameters for the definition of the grids and of the initial and boundary conditions. It have a great importance because it allows to modify grid domain and time-space interpolation. The main sections of this namelist are:

- `&share`, that describes variable in common for the different steps;
- `&geogrid`, that describes dimensions and parameters of domain and sub-domains;
- `&ungrib`, concerning ungrib output files;
- `&metgrid`, concerning metgrid output files.

It is possible to create multiple nested domains inside the main domain. A *nested domain* is completely contained within its *parent domain* with a finer-resolution grid. It is a very useful way to analyze in greater detail a small portion of the domain, using data generated in the external domain as boundary and initial conditions for the nested grid. There are two types of nesting:

- One-way nesting, when information flows only to the nested grid from the larger, lower-resolution domain during the simulation;
- Two-way nesting, when both the main and nested domains have mutual feedback during simulation across sub-domain boundaries. In this case, the information moves in both directions, from the external to the internal grids and viceversa.

3.1.2 ARW Model

It is the main component of modeling system that resolves the fully compressible governing equations. WPS is the initial step to generate domain where equations will be solved; however, it is necessary that WRF is configured before WPS. To do this, one will choose `em_real` to deal with a real case. After configuring it, the following programs will be generated:

- `real.exe`, that allows the WRF initialization;
- `wrf.exe`, that is the model executable.

After compiling WRF, it is necessary to check and modify `namelist.input` file because main options in this file have to be the same as `namelist.wps`. Concerning the WRF namelist, the main sections are:

- `&time_control`, concerning run, start and end time options;
- `&domains`, concerning parameters of domains;

- `&physics`, for physics and microphysics parameterizations, like cumulus convection, precipitation, radiation and planetary boundary layer;
- `&dynamics`, for dynamical parameterizations;
- `&bdy_control`, for boundary condition options.

Afterward, it is possible compile `real.exe` to create the fields in the boundary and initial conditions in all model levels where data are interpolated. Then one runs `wrf.exe` to create the forecasts.

3.2 Input Data

To create initial and boundary conditions forcing the NWP, the ECMWF Reanalysis 5th Generation (ERA5) was used in all case-studies. ERA5 replaces the previous ERA-Interim reanalysis. The horizontal and vertical coverage of ERA5 data is global and from 1000 hPa to 1 hPa respectively; the horizontal resolution is 0.25° × 0.25°, while the hybrid sigma/pressure levels are 137. The released ERA5 data covers the period, hourly, from 1979 and continues to be extended forward in near real time. With respect to ERA-Interim, ERA5 distinguishes data on pressure (or model) levels between surface level in distinct files. ERA5 data, and tecnical information about them, was downloaded from the Climate Data Store website [19].

3.3 Post-processing tools

Post-processing tools allow the plotting of the results of the simulation in 2D or 3D so that they can be easily understood and analyzed by users. There are a number of visualization tools available to display WRF model data. Since the model data is written in NetCDF format, essentially any tool capable of displaying this data format can be used to display the WRF model data. The tools used in this work are described in the following sections.

3.3.1 ARWpost

It is a package that reads the ARW output in NetCDF format only and creates the GrADS input files. ARWpost can process also WPS geogrid and metgrid output data and output from real-weather and idealized simulations. To prepare ARWpost for conversion, it is necessary to edit `namelist.ARWpost` file.

3.3.2 GrADS

Grid Analysis and Display System (GrADS) is an interactive tool used for manipulation, and visualization of earth science data. GrADS support a number of data file format (GRIB,

NetCDF, HDF, ...). In this work, input data in NetCDF format are used in ARWpost to produce GrADS input files. GrADS uses a 5-Dimensional data environment: the four conventional dimensions (longitude, latitude, vertical level, and time) plus an optional 5th dimension for grids that is generally implemented but designed to be used for ensembles. GrADS handles grids that are regular, non-linearly spaced, gaussian, or of variable resolution. Common representations with GrADS are temperature and geopotential maps at fixed isobaric levels, wind fields and vertical cross-sections of atmosphere. It is mainly a 2D data visualization. Most of vertical and horizontal cross-sections are generated with GrADS in this study.

Listing 3.1 – Example of namelist.ARWpost

```
&datetime
 start_date = 'yyyy-mm-dd_hh:mm:ss',
 end_date = 'yyyy-mm-dd_hh:mm:ss',
 interval_seconds = 10800, ! output intervals (in seconds)
/

&io
 input_root_name = 'input_root_name'
 output_root_name = 'output_root_name'
 plot = 'list'
 fields = 'LH,HFX,QVAPOR,QCLOUD,W,QRAIN,T2,height,geopt,theta,tk,td,td2,rh,rh2,wspd,
           umet,vmet,pressure,u10m,v10m,slp,mcape,mcin,lcl,lfc,dbz,max_dbz'
 mercator_defs = .false.
/

&interp
 interp_method = 1, ! on pressure levels
 interp_levels = 1000.,975.,950.,925.,900.,850.,800.,750.,700.,650.,600.,550.,500.,450.,400.,
                 350.,300.,250.,200.,150.,100.
 extrapolate = .true.
/
```

3.3.3 NCL

NCAR Command Language (NCL) is a free interpreted language designed specifically for scientific data analysis and visualization, developed by the Computational and Information Systems Laboratory (CISL) at the NCAR. It can read and write NetCDF, Hierarchical Data Format (HDF) and binary data; it can also read HDF and GRIB files. In this work version 6.6.2 was used to modify `met_em` files to perform some sensitivity tests. Few lines of code used are shown in listing 3.2.

Listing 3.2 – Example of NCL script

```
load "$NCARG_ROOT/lib/ncarg/nclscripts/csm/gsn_code.ncl"
load "$NCARG_ROOT/lib/ncarg/nclscripts/csm/gsn_csm.ncl"

...

  a4 = addfile("met_em.d01.1996-10-04_09:00:00.nc","w")
  rh4 = a4->RH
  rh4 = rh4 > 50.
  a4->RH = rh4

  print("SUCCESSFUL STEP 4")

...
```

3.3.4 VAPOR

Visualization and Analysis Platform for Ocean, Atmosphere, and Solar Researchers (VAPOR) is a 3D fluid dynamic visualization tool, developed at NCAR in Pyhton language.VAPOR can read a `file.vdf` converted from a WRF output file using `wrfvdfcreate` command after VAPOR installation. In this work versions 2.6 and 3.2 were used, mainly to plot 3D streamlines for back-trajectory analysis.

At this point a clarification is needed before introducing the back-trajectories. VAPOR is able to deal with steady or unsteady fields: in our case, we want to focus on wind field (composed by U, V and W vectors) to plot back-trajectories. Naturally, wind field is a non-stationary field. In some circumstances (e.g., at upper atmospheric levels under stationary conditions or when a well defined low level flow exists and remains stationary for several hours) streamlines can be calculated with good approximation using stationary wind field at a given time. In fact, a comparison with the streamlines calculated without this approximation, but using the wind field with U, V and W vectors that vary at every time steps, does not show significant differences. In contrast, stationary approximation cannot be used when the wind field varies a lot in time in a specific point of space (e.g., during the cyclone formation in close proximity of the sea level pressure minimum). To better show the behavior and features of the air masses involved in the precondition and formation phases of the cyclones, we should sometimes use plots referred at a previous time with respect the time when the streamlines are calculated (in our case, a previous moment with respect the initial time when the back-trajectories are plotted), putting side by side different fields at different hours. This will be done, if necessary, to try to better describe the phenomenon in its entirety. In this works, all the streamlines are calculated using the unsteady wind field with model output of one hour.

II | Case studies

4 | Medicane Zeo

The first case study is a cyclone that developed on 13 December 2005, named *Zeo* by Deutscher Wetterdienst Wetter und Klima aus einer Hand (DWD). A vast cyclogenesis centered on the Libyan Sea occurred on 13 December; the cyclone deepened and intensified, bringing severe weather to Tunisia and Sicily. During the following day, the storm acquired subtropical and later tropical characteristics during the night. The tropical-like cyclone continued to move eastward over the eastern Mediterranean Sea, maturing for a few hours into a medicane structure between the island of Crete and Libya. Zeo made landfall on the coasts of Lebanon on the morning of 16 December with tropical-storm intensity. Two natural-color satellite images of the cyclone are shown in figure 4.1; figure 4.1a shows its mature stage while 4.2b its decay phase.

The simulation with WRF4.1 lasts from 00:00 UTC of 11 December 2005 to 00:00 UTC of 16 December 2005. The model integration domain has a horizontal grid spacing of 9 km and 40 vertical levels (more closely spaced in the boundary layer). The grid is centered at 36°N, 6°E and has 400 × 350 horizontal grid points. ERA5 reanalysis was used. The simulated trajectory in figure 4.2 is in accordance with other works (Miglietta and Rotunno, 2019 [42], Fita and Flaounas, 2018 [26]).

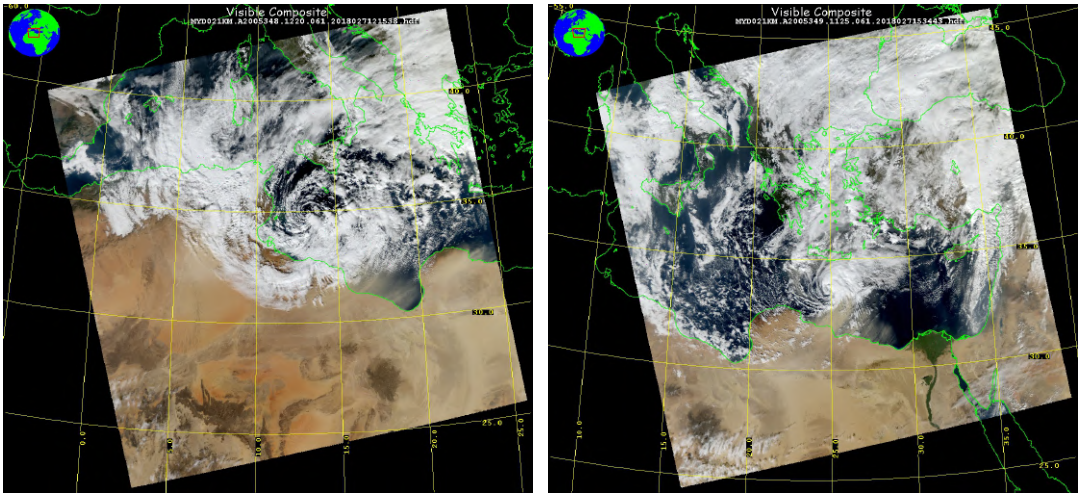

(a) 14 December 2005 - 12:20 UTC (b) 15 December 2005 - 11:25 UTC

Figure 4.1 – Medicane Zeo satellite images taken from the MODIS AQUA satellite

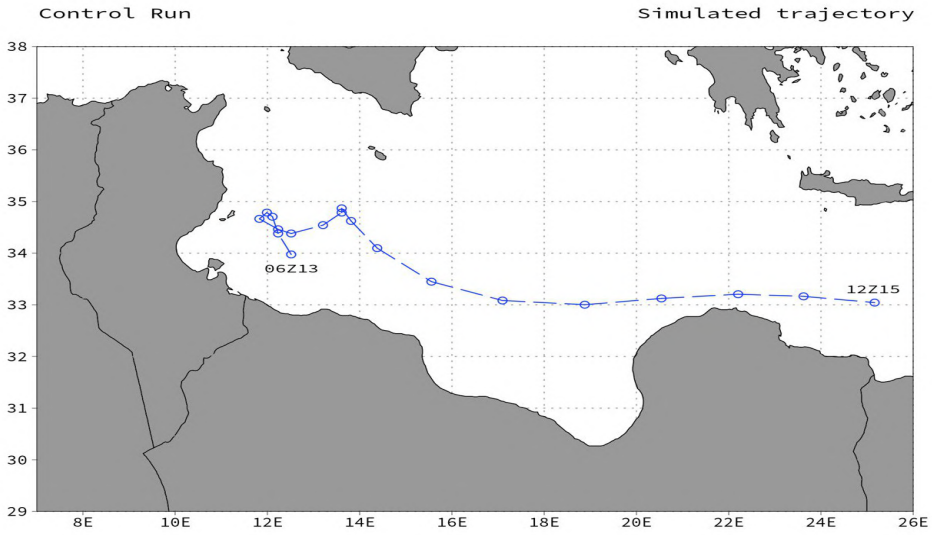

Figure 4.2 – Simulated trajectory of Medicane Zeo - points every 3 hours

4.1 Initial conditions

Since the purpose of this study is to analyze the characteristics of this category of cyclones before and during their formation and development, hereafter we describe the state of the atmosphere, starting from before the formation of the cyclone. In figure 4.3 the temperature field and the geopotential at 500 hPa are shown on the left, while the sea level pressure on the right; the figures 4.3a,b show the initial condition of the simulation. The temperature field shows an elongated trough extending from northeastern Europe that remains trapped over the western Mediterranean between two highs forming an upper-level cut-off, while an area of low pressure extends from the tropics to the Ionian region in the lowest layer of the atmosphere. After 24 hours - figures 4.3c,d - the pressure minimum, associated with a cold pool, cuts off from the large-scale circulation; at the low levels, on its east side, the low-pressure structure is still present, showing two minima over the Tyrrhenian Sea and on the north African mainland. The presence of a cold air mass in the upper troposphere is a crucial ingredient in the triggering of medicanes (Emanuel, 2005 [20]), because it increases the instability of an atmospheric column thus favoring convection.

The other important factor favorable to the development of deep convection is the presence of moist air in the lower and midtroposphere. Figure 4.4 shows the equivalent potential temperature and the wind field at 700 hPa on the left, and the water vapor mixing ratio at 700 hPa with sea level pressure contours on the right. The cold pool can be identified in the same area as in figure 4.4; a strong gradient of θ_e is present in the future cyclogenetic area. The water vapor mixing ratio on the right side of figure 4.4 identifies an area of moist air above the region where the cyclone will form.

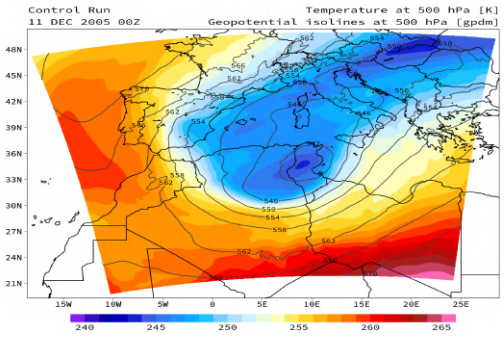

(a) 11 December 2005 - 00:00 UTC

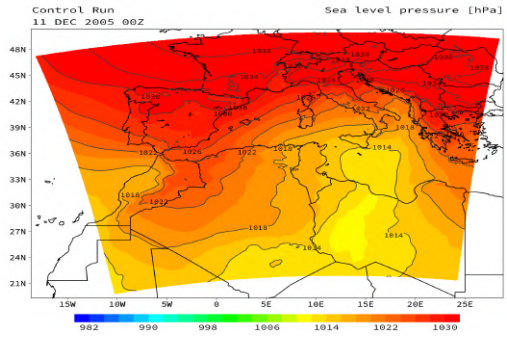

(b) 11 December 2005 - 00:00 UTC

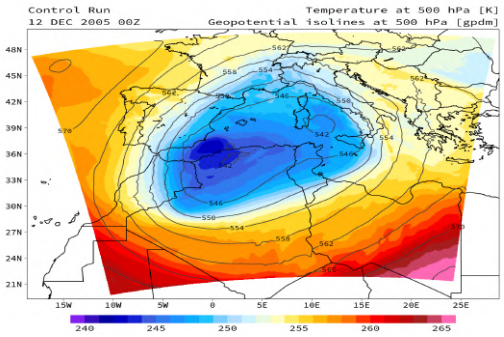

(c) 12 December 2005 - 00:00 UTC

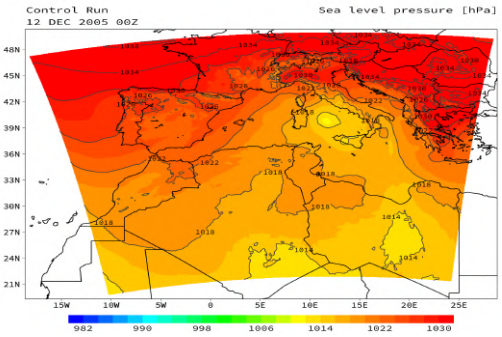

(d) 12 December 2005 - 00:00 UTC

Figure 4.3 – Control run temperature field at 500 hPa and sea level pressure surfaces

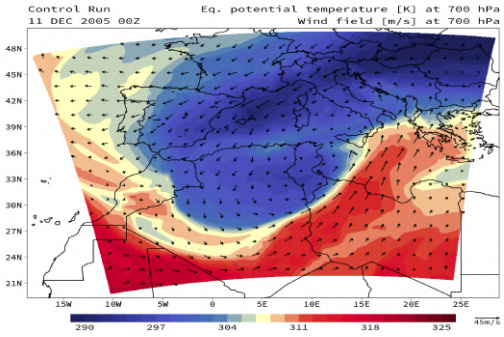

(a) 11 December 2005 - 00:00 UTC

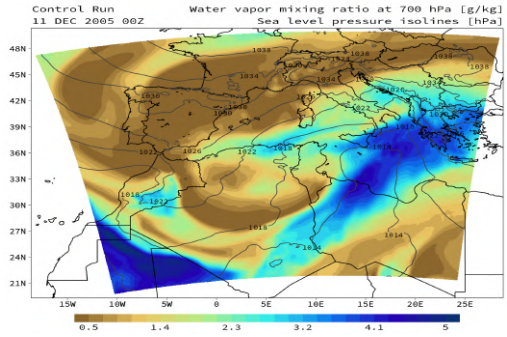

(b) 11 December 2005 - 00:00 UTC

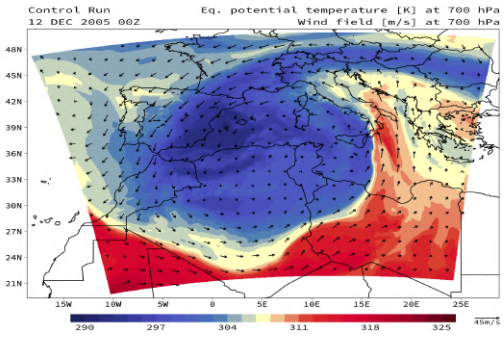

(c) 12 December 2005 - 00:00 UTC

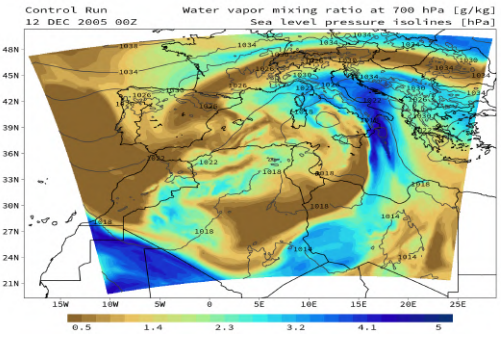

(d) 12 December 2005 - 00:00 UTC

Figure 4.4 – Control run θ_e field at 700 hPa and water vapor mixing ratio at 700 hPa

4.2 Moist air masses analysis

Following the analysis of Miglietta et al., 2019 [42] on the role of latent- and sensible-heat fluxes from sea surface as a crucial ingredient in the cyclone formation, the first survey of this case study concerns the behavior of moist air masses on meso- and synoptic-scales. We begin the discussion of the preconditioning phase of cyclogenesis using maps at fixed pressure levels and back-trajectory analysis. The first row of figure 4.5 shows water-vapor mixing ratio at 950 hPa (figure 4.5a) and latent-heat fluxes from surface (figure 4.5b), 36 hours after the beginning of the simulation; in these figures a peak of water vapor is evident over the Ionian Sea. The origin of this moist air mass can be found, at least in part, using the back-trajectory analysis for parcels arriving at 500 m (figures 4.5c,d,e,f). The origin of back-trajectories are marked with red line in figure 4.5a. There is a well-defined flow at 950 hPa coming from eastern Europe to the Ionian region, associated with an anti-cyclonic circulation over the Balkans. Back-trajectory analysis for parcels arriving at 500 m height shows air parcels descending near the sea surface approximately over the Aegean Sea and acquiring water vapor during their passage over the sea toward the Ionian Sea, where the maximum of water vapor mixing ratio can be identified (green-brown section in figures 4.5c,d,e,f). A vertical cross section located farther south shows nearly the same path with a additional contribution of moist air coming from the lower layers of the eastern Mediterranean basin. Figure 4.5b showing latent-heat flux confirms that evaporation is responsible for the increase of humidity during the passage of the air parcels over the Aegean sea.

Figure 4.6b shows the 850 hPa water vapor mixing ratio; a vast area of moist air is present off the Libyan coast. According to the back-trajectory analysis for parcels reaching the area of maximum of humidity at 850 hPa in figure 4.6c,d, the zone of maximum of humidity is fed by two different contributions: flow coming from the east of the Mediterranean basin and from the tropical region. The trajectories coming from the east, that lift up during their path (figure 4.6c), are associated with the circulation around a mesoscale pressure high over the eastern Mediterranean. In contrast, the trajectories from the south, undergoing a relatively slight lifting during their path, from 750-1000 m (figure 4.6c), can be associated with a synoptic-scale flow coming from the south. To get a better insight of this upper flow, we focus on the flow in the middle of the trajectory, 12 hours before the cyclone arrives over the Ionian regions. This is necessary because, as already reported, back-trajectories are calculated considering the unsteady behavior of the wind field; in this phase, the wind field varies a lot in time; moreover, analyzing the wind field at the same elevation of the back-trajectories final points (i.e., red lines section in figure 4.6b at 1500 m) can be misleading because trajectories change their elevation. For these reasons, we show in figure 4.6a the wind field at 900 hPa referred at 00:00 UTC of 12 December. We can see that a well defined flow exists coming from the south to our area of interest. Another section located farther south shows that the main contribution at more southern latitudes comes totally from the southern regions (figures 4.6a,e,f).

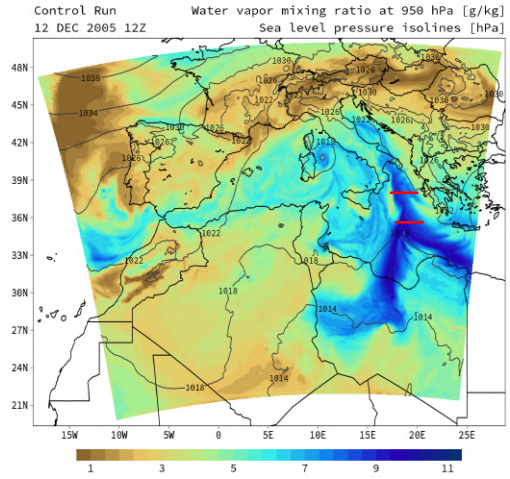

(a) 12 December 2005 - 12:00 UTC

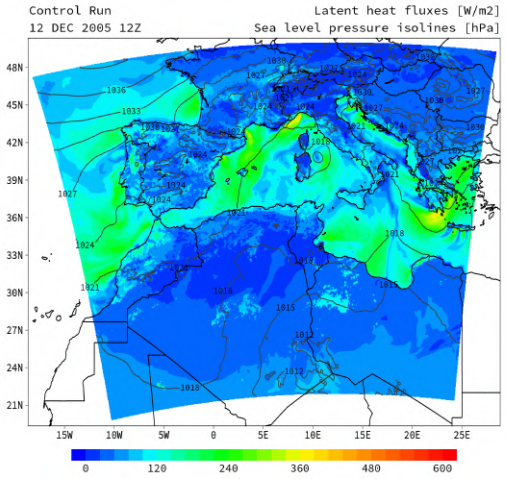

(b) 12 December 2005 - 12:00 UTC

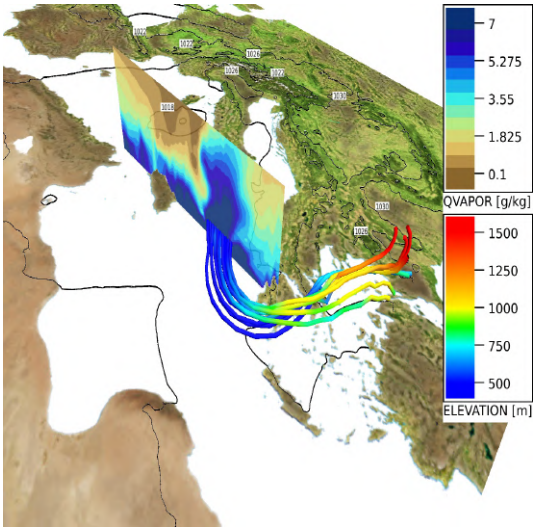

(c) Back-trajectories of 24h from 500 m

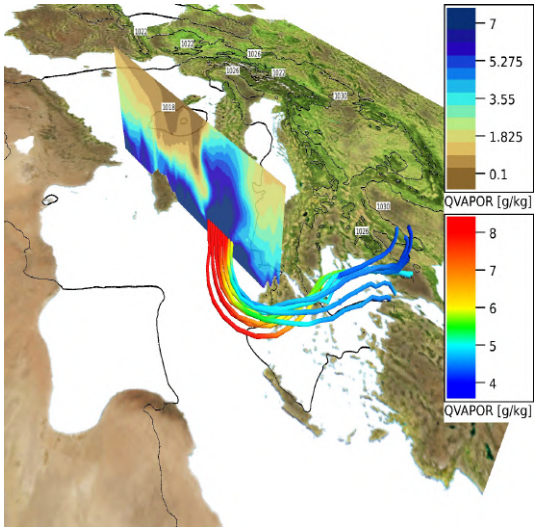

(d) Back-trajectories of 24h from 500 m

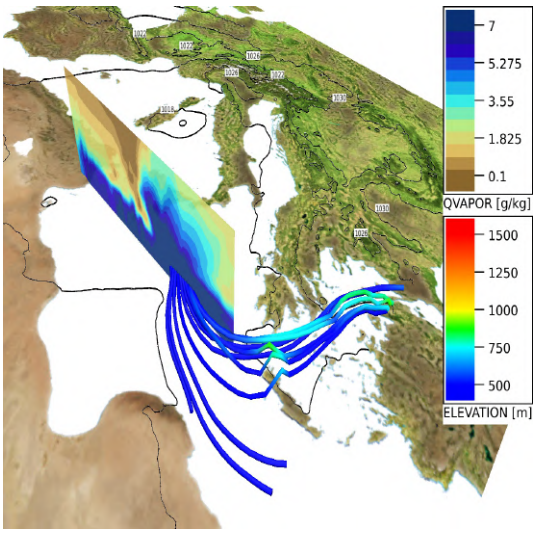

(e) Back-trajectories of 24h from 500 m

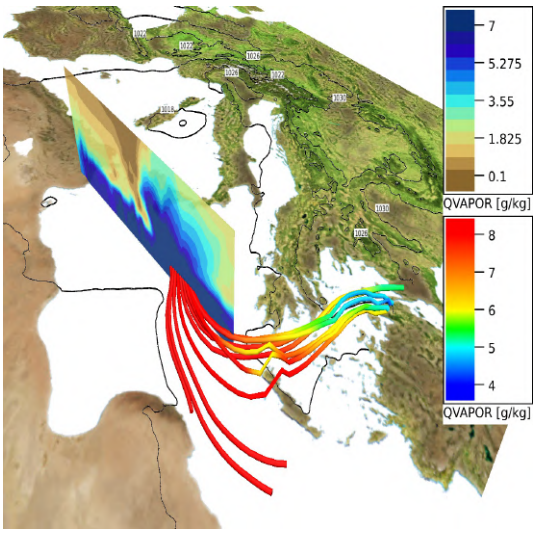

(f) Back-trajectories of 24h from 500 m

Figure 4.5 – Moist air back-trajectory analysis at 950 hPa

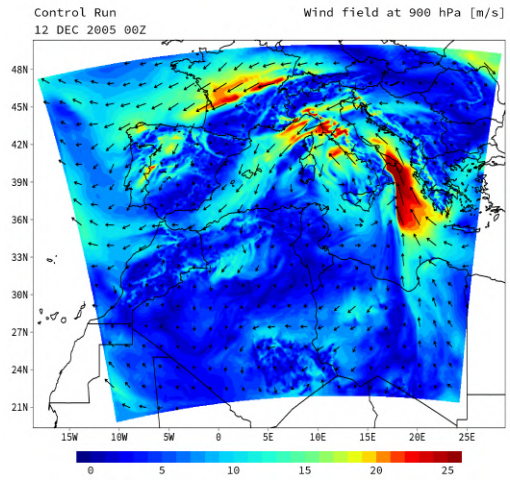

(a) 12 December 2005 - 00:00 UTC

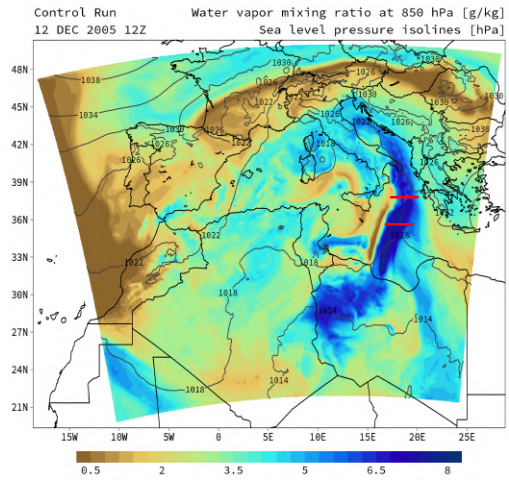

(b) 12 December 2005 - 12:00 UTC

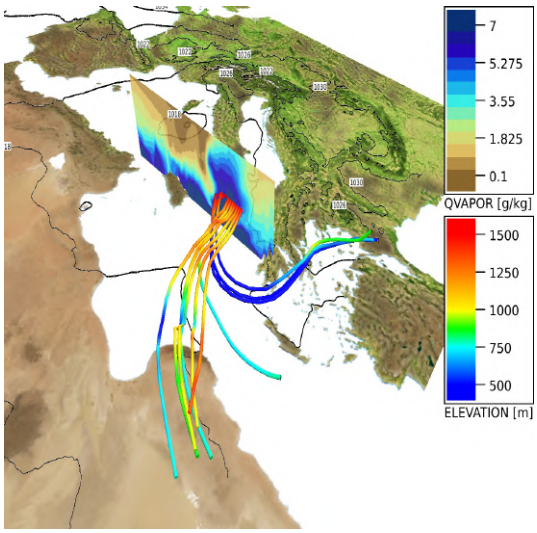

(c) Back-trajectories of 24h from 1500 m

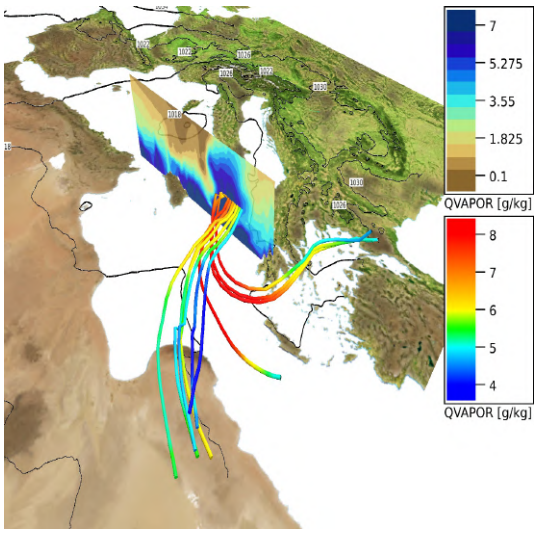

(d) Back-trajectories of 24h from 1500 m

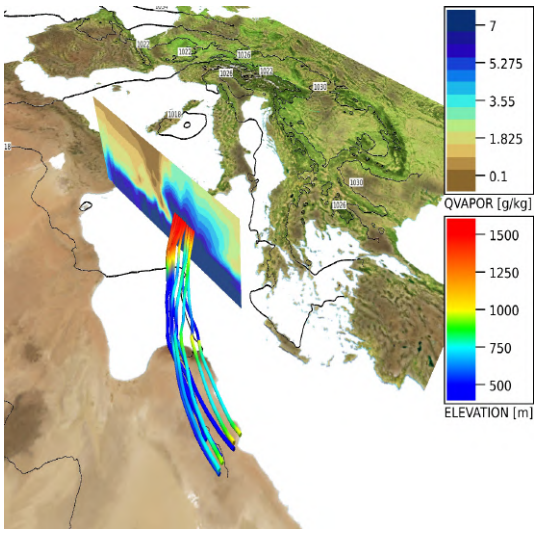

(e) Back-trajectories of 24h from 1500 m

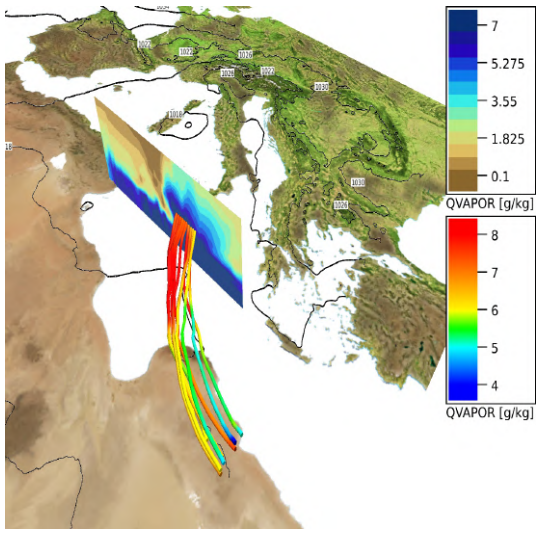

(f) Back-trajectories of 24h from 1500 m

Figure 4.6 – Moist air back-trajectory analysis at 850 hPa

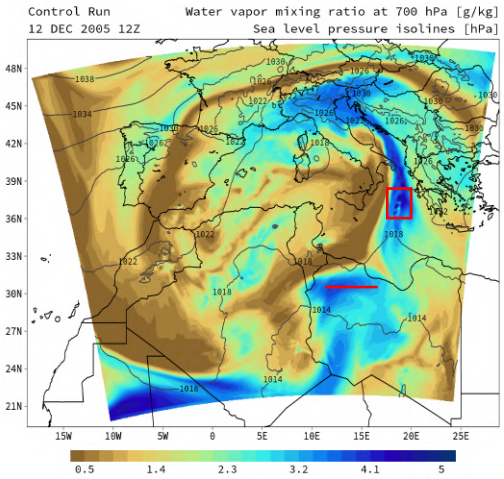

(a) 12 December 2005 - 12:00 UTC

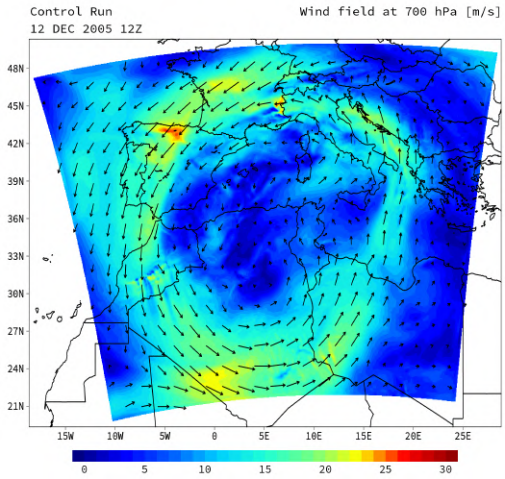

(b) 12 December 2005 - 12:00 UTC

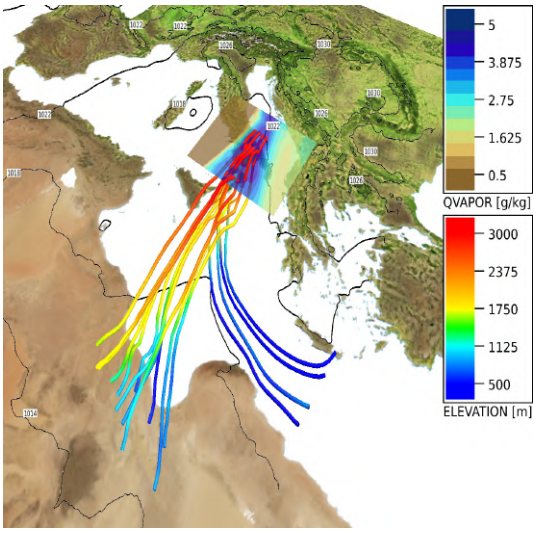

(c) Back-trajectories of 24h from 3000 m

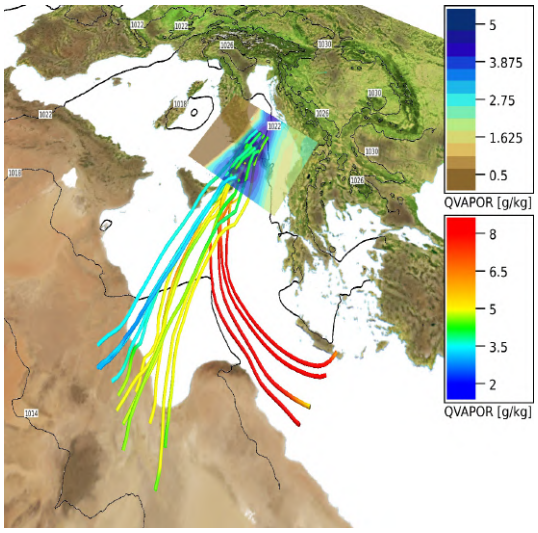

(d) Back-trajectories of 24h from 3000 m

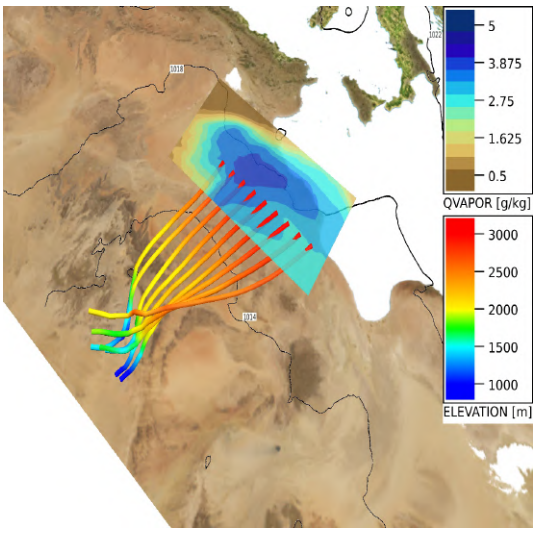

(e) Back-trajectories of 24h from 3000 m

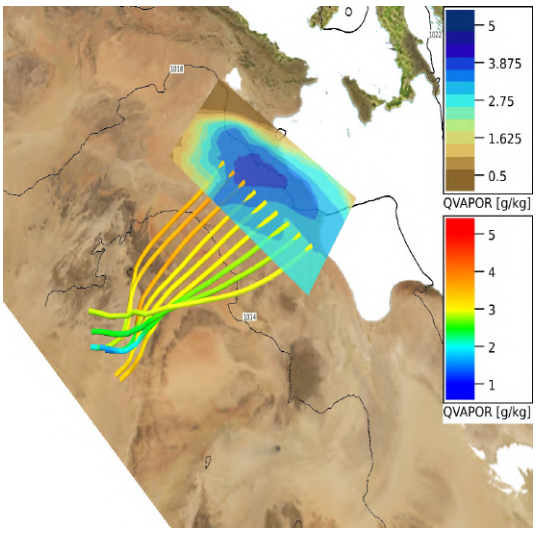

(f) Back-trajectories of 24h from 3000 m

Figure 4.7 – Moist air back-trajectory analysis at 700 hPa

Lastly, at 700 hPa, two sections for back-trajectories are shown. The former is a plane located in the area of maximum of humidity over the Ionian regions and the latter a line located a more southern latitudes. The moist air over the Ionian Sea has again two contributions (figures 4.7c,d): one from the lower levels of the eastern Mediterranean basin and another from the Tropics. The latter contribution appears to be the major to humidify the atmosphere at 700 hPa; it is associated with a meso- and synoptic- scale flows (see wind field at 700 hPa in figure 4.7b). At this height, the transport of moist air is associated with the large-scale features, bringing humidity from the Atlantic region and the tropical areas into the Mediterranean region. This is shown both in the water-vapor mixing ratio maps (figure 4.7a, where we can see a high humidity content zone between 21° and 24° N that moves northward between 10° and 15° E) and in the back-trajectories starting from southern (figures 4.7c,d). Although these southern back-trajectories reach the borders of the domain of simulation and do not show their entire path, it is very likely that these trajectories come from the equatorial region of West Africa, noting the related wind direction (figure 4.7b).

4.3 Sensitivity tests without surface fluxes

According to Miglietta et al., 2019 and with reference to figure 4.5b, heat fluxes from the sea surface create a favorable environment for the cyclone formation allowing the evaporation into the atmosphere of water vapor. To investigate this hypothesis we have undertaken a sensitivity test where latent- and sensible-heat fluxes have been turned off, throughout the whole domain, in the first 36 hours of simulation with respect to the control run, and then turned on again afterward until the end of simulation. From now on, we will refer to this test as 'No Fluxes' test. This simulation was run by putting the parameter of the namelist.input file `isfflx=0` for the first 36 hours and leaving the other parameters unchanged. After 36 hours of simulation without sensible- and latent-heat fluxes from the surface, the simulation was restarted using the WRF restart procedure with the parameter `isfflx=1`, that is the heat fluxes from the surface have been turned on again in the whole domain.

Before moving on to the analysis of the sensitivity simulation, it is necessary to verify that the isobaric and geopotential fields of the No Fluxes test do not change too much with respect to the control run at the time when the fluxes were turned back on in the No Fluxes test at 12 December 12:00 UTC. This is necessary in order to demonstrate that the pressure patterns in the area where the cyclone will form do not change significantly. Otherwise, in the case that the starting situation differs, the changed pressure fields may affect the following evolution of the cyclone, making it more difficult to disentangle the role of the evaporation in the intensification of the cyclone.

In figure 4.8 are shown, on the left, the difference in sea level pressure between the control run and the No Fluxes test over the region where the cyclone will form; the same procedure

was applied for the difference in geopotential heights on the right. Since the differences in sea level pressure, in absolute value, are limited between 0 and 3 hPa and around 1 hPa in most of the area, we can consider the pressure configuration not significantly affected by the sensitivity experiment at 12 UTC of 12 December 2005. Analogous considerations can be done looking at geopotential height difference figure 4.8b since the difference at 500 hPa is small over the area of cyclone development. Since the structure of the atmosphere is very similar in both cases, we may conclude that the different evolution of No Fluxes simulation is not connected to changes in the isobaric or geopotential field but to the content of atmospheric humidity. Note that some significant differences, of about 5 hPa, are present in the mean sea level pressure over the Tyrrhenian Sea, associated with a weaker intensification of the cyclone formed at early stages of the simulation over there. However, the cyclone does not affect the following evolution of the medicane. Similar considerations apply to changes in 500 hPa geopotential height over Morocco.

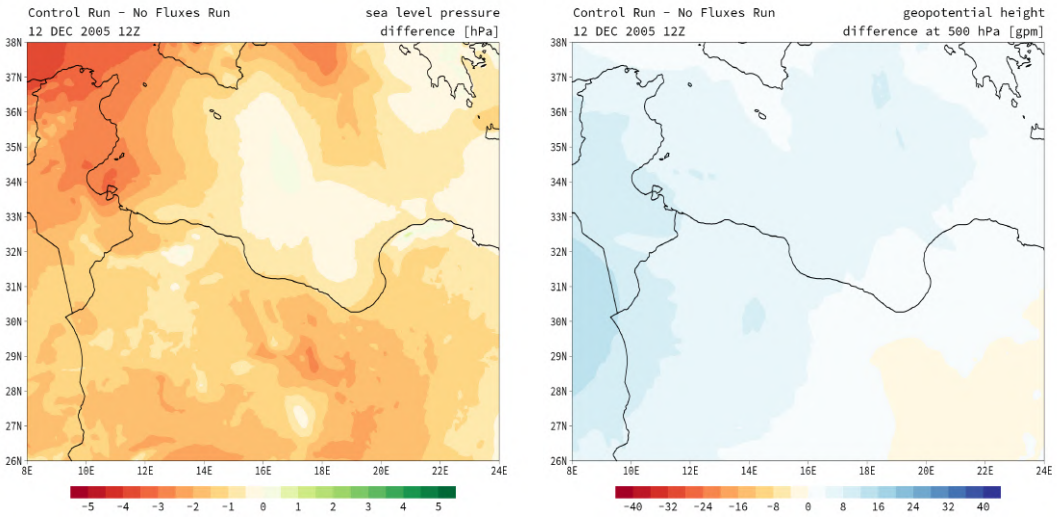

(a) (b)

Figure 4.8 – Isobaric and geopotential height differences between the control run and the No Fluxes test

In figure 4.9a,b are shown the Integrated Water Vapor (IWV) and the water vapor mixing ratio at 1000 hPa in figure 4.9c,d; figures on the left are from the control run and from the No Fluxes test on the right. The differences of integrated water vapor after 36 hours in the two runs can be mainly explained looking at the water vapor mixing ratio at 1000 hPa at the same time: it is clear that without heat fluxes from surface, the content of water vapor over the Ionian Sea dramatically decreases. After 30 additional hours, there are smaller differences between the control run and the No Fluxes test in both IWV and the water vapor mixing ratio (figures 4.9e,f,g,h). At the time the surface fluxes are turned on again (12 UTC, 12 December 2005), the atmosphere in the sensitivity test has relatively less water vapor, hence the fluxes can transfer to the lower troposphere a large amount of water vapor and at 13 December 18:00

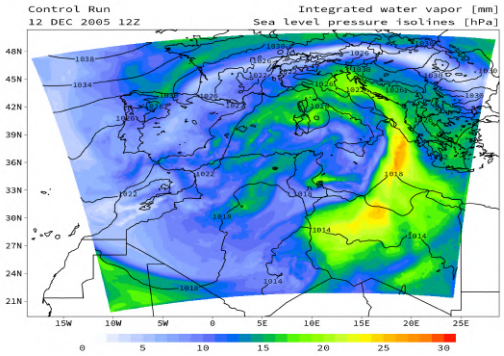

(a) 12 December 2005 - 12:00 UTC

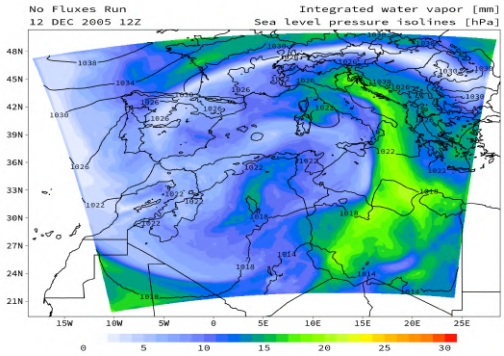

(b) 12 December 2005 - 12:00 UTC

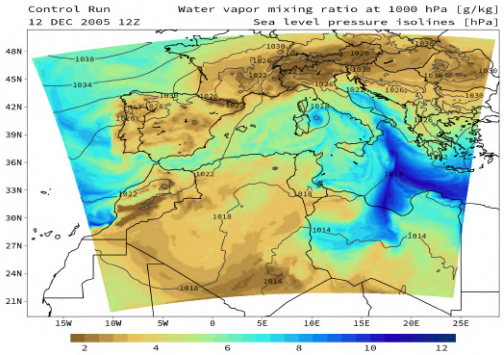

(c) 12 December 2005 - 12:00 UTC

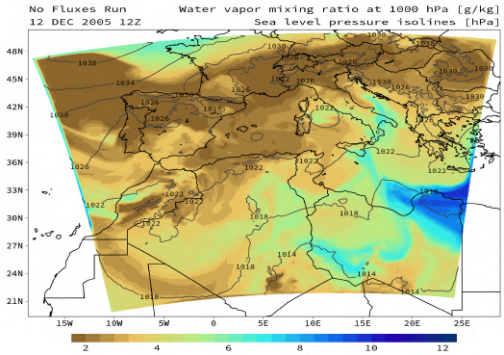

(d) 12 December 2005 - 12:00 UTC

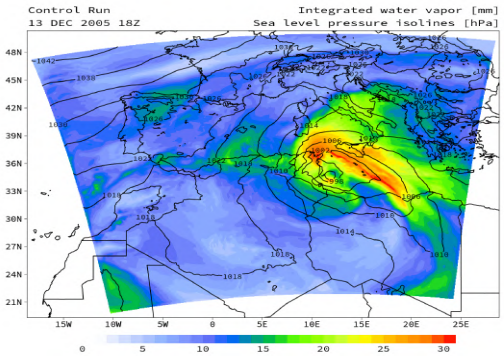

(e) 13 December 2005 - 18:00 UTC

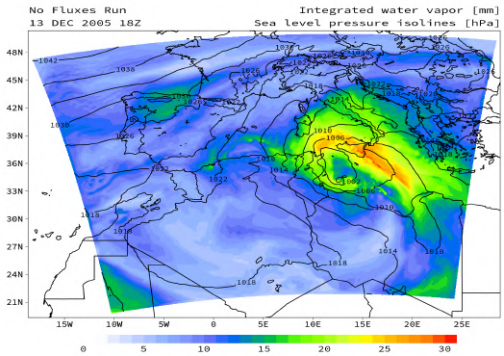

(f) 13 December 2005 - 18:00 UTC

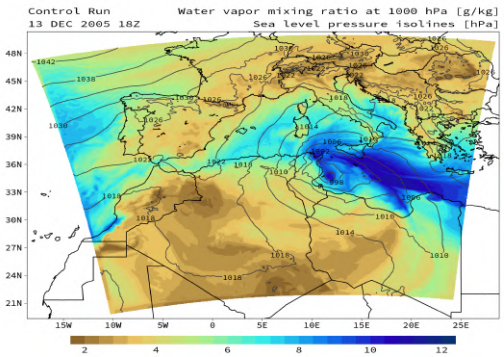

(g) 13 December 2005 - 18:00 UTC

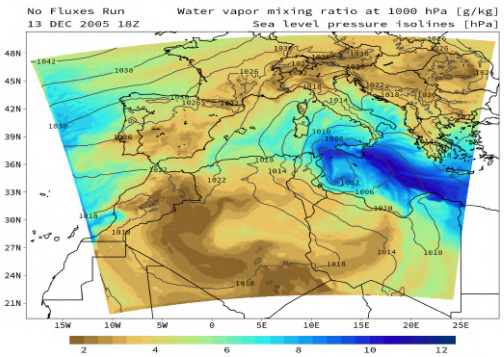

(h) 13 December 2005 - 18:00 UTC

Figure 4.9: Integrated water vapor and water vapor mixing ratio at 1000 hPa in the control run and No Fluxes test

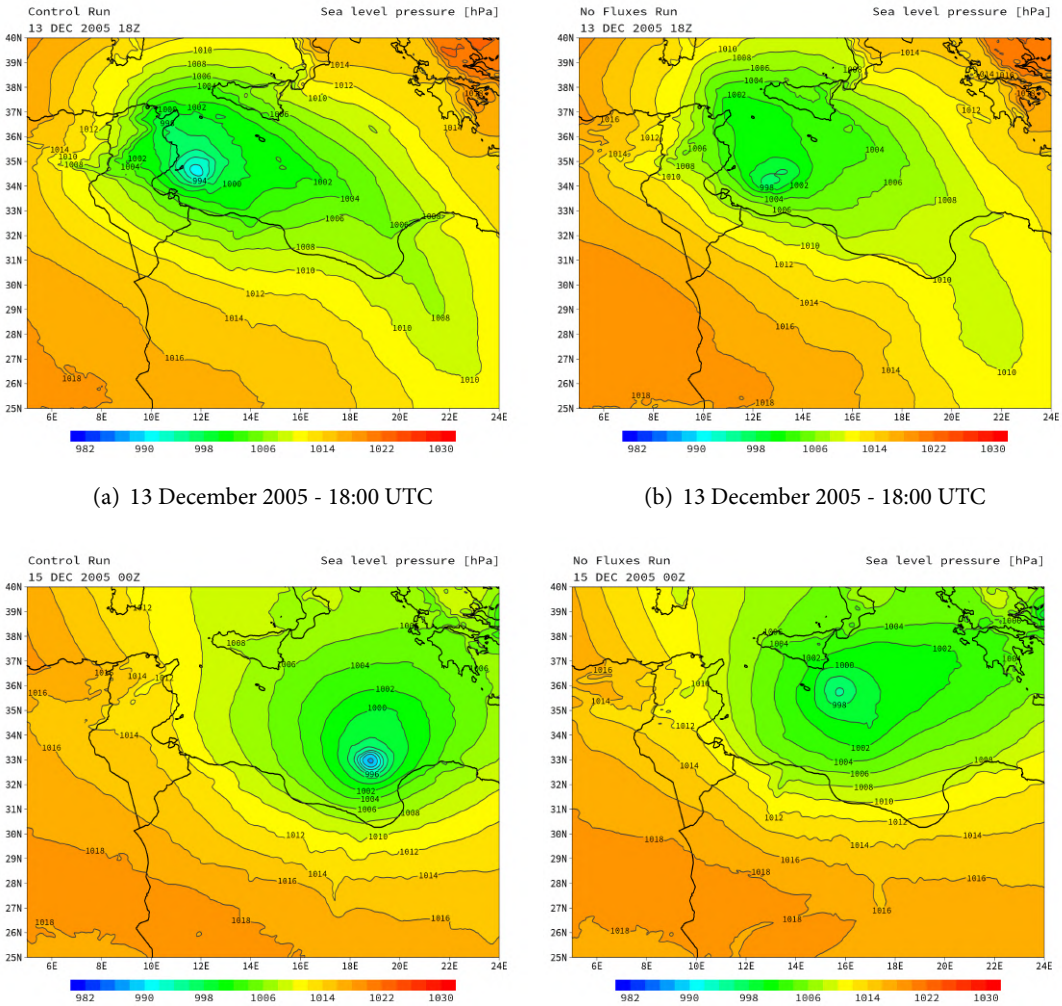

(a) 13 December 2005 - 18:00 UTC

(b) 13 December 2005 - 18:00 UTC

(c) 15 December 2005 - 00:00 UTC

(d) 15 December 2005 - 00:00 UTC

Figure 4.10 – Sea level pressure isolines in the control run and No Fluxes test

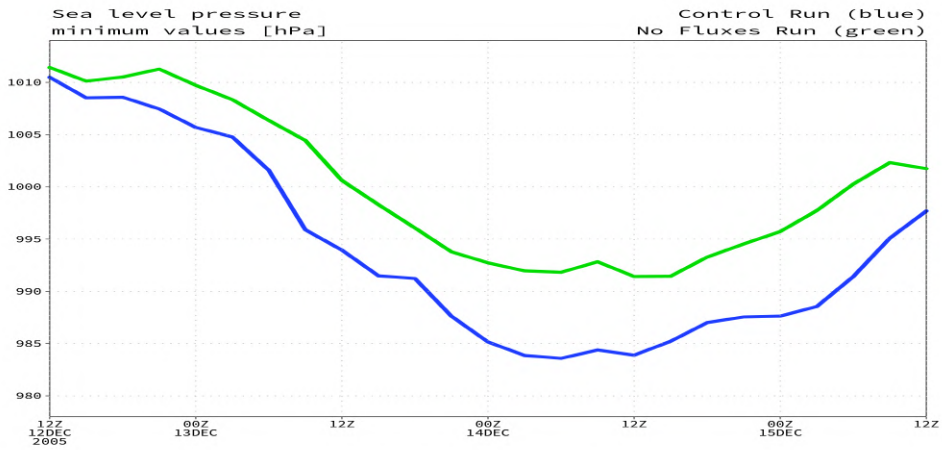

Figure 4.11 – Sea level pressure minimum values (every 3 hours) in the control run and in No Fluxes test

UTC the differences become small. However, the pressure field and the structure of the cyclone are altered with respect to the control run, as we can see in figure 4.10. In particular, the cyclone is less intense than in the control run (figure 4.11), with a maximum difference of sea level pressure of 10 hPa when the control run cyclone is most intense. Thus heat fluxes from the sea surface are essential to create favorable humidity conditions for the formation and maintenance of the cyclone.

4.4 Dry air masses analysis

The second point we investigate is the behavior and impact of dry air masses in the formation of the cyclone. Recent studies assert that for extratropical cyclones, dry-air intrusion promotes the intensification of the cyclones (Raven-Rubin, 2017 [55]). However, medicanes are not extratropical cyclones, but rather subtropical cyclones in their mature stage, since they contain both baroclinic features and a strong dependence on air-sea-interaction processes. To our knowledge, no study deals with dry-air intrusions in medicanes formation and evolution.

To identify dry-air masses involved in the cyclone formation, we use again the back-trajectory analysis. Water vapor mixing ratio at 500 hPa and back-trajectories, that start from 500 hPa, are shown in figure 4.12. The dry air that reaches the future cyclogenetic area (red line in figure 4.12a) in the preconditioning phase, is associated with a large-scale flow that comes from the medium/high-troposphere. These trajectories are likely associated with a stratospheric-air intrusion (figure 4.12b), as shown by their extremely low values of water vapor mixing ratio (figure 4.12d).

In figure 4.13 are shown back-trajectories of dry air transport referred to the initial phase of the cyclone development, starting from the horizontal red section depicted in figure 4.13a. At 13 December 2005 12:00 UTC, the contribution of dry air is again of large scale origin, coming from Northwest of the domain and curving eastward over the Africa mainland. These dry parcels come apparent from the high-troposphere/lower-stratosphere, originated at 7000 m 36 hours before (see figure 4.13b). Cross sections of relative humidity (figure 4.13c,d) allow one to identify a dry-air intrusion that extends above the center of the forming cyclone (the center of the cyclone is the minimum value of sea level pressure and is located in the center of the figures, at 34.5° N in section on figure 4.13c and at 34.6° N in figure 4.13d). This intrusion of dry air may inhibit deep convection in the forming cyclone because of the arrival of drier air and its mixing with the surrounding moist air. This hypothesis will be tested with sensitivity experiments discussed in the following section.

Figure 4.14 shows, on the left, water-vapor mixing ratio at 850 hPa and, on the right, aerosol content of Modern Era Retrospective analysis for Research and Applications Aerosol Reanalysis (MERRAero) (values on the right scale of figure 4.14b are referred to the Aerosol Optical Depth (AOD) at 550 nm; AOD is the degree to which aerosols prevent the transmission of light

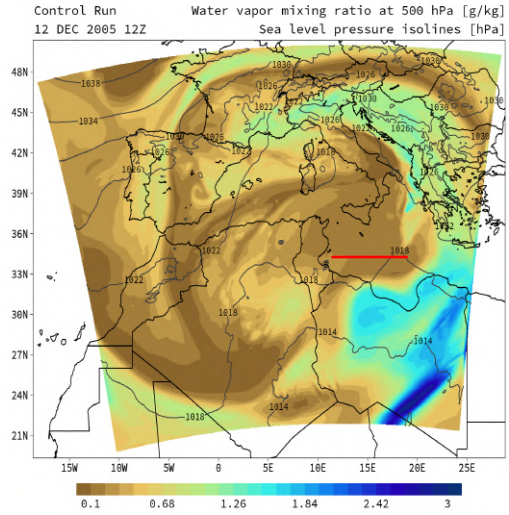

(a) 12 December 2005 - 12:00 UTC

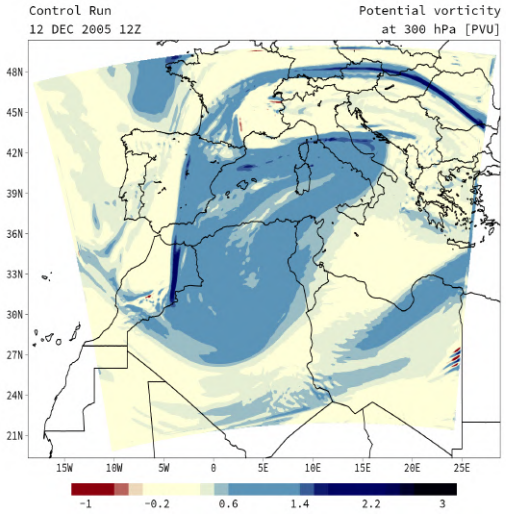

(b) 12 December 2005 - 12:00 UTC

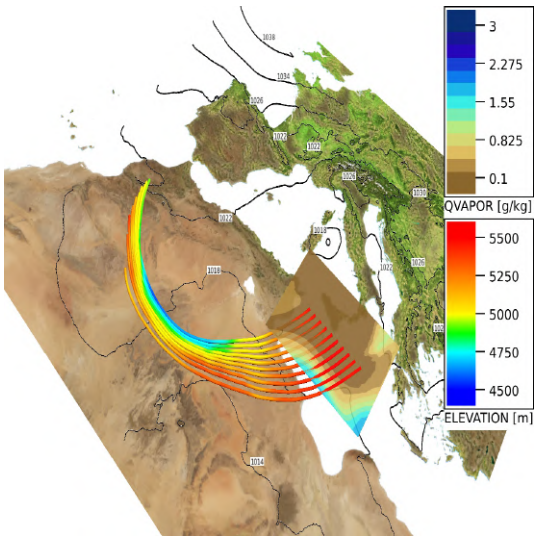

(c) Back-trajectories of 36h from 5500 m

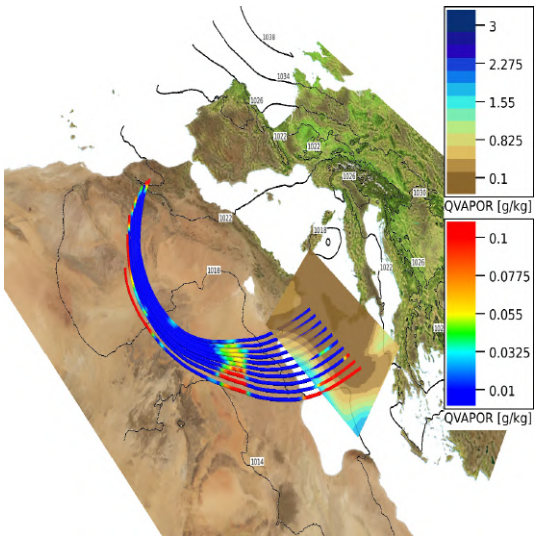

(d) Back-trajectories of 36h from 5500 m

Figure 4.12 – Dry air back-trajectory analysis at 500 hPa

by absorption or scattering of light and it is defined as the integrated extinction coefficient over a vertical column of unit cross section). MERRAero provides reanalysis products from the 5th version of the Goddard Earth Observing System Data Assimilation System (GEOS-5). GEOS-5 is radiatively coupled to the Goddard Chemistry, Aerosol, Radiation and Transport (GOCART) aerosol module and includes assimilation of aerosol optical depth from the MODIS sensor on board the Electro-Optical System (EOS) Aqua and Terra satellites. In figure 4.14a, spots of drier air are visible immediately southern of the region of maximum content of water vapor. A comparison of figures 4.14a and 4.14b shows the same comma-like dry-air structure, although the location is not exactly coincident. We suppose that is very likely that the dry comma structure that WRF is able to simulate has, at least in part, origin from the Saha-

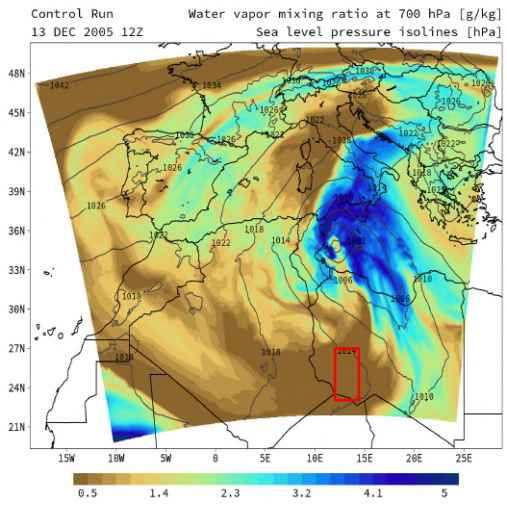

(a) 13 December 2005 - 12:00 UTC

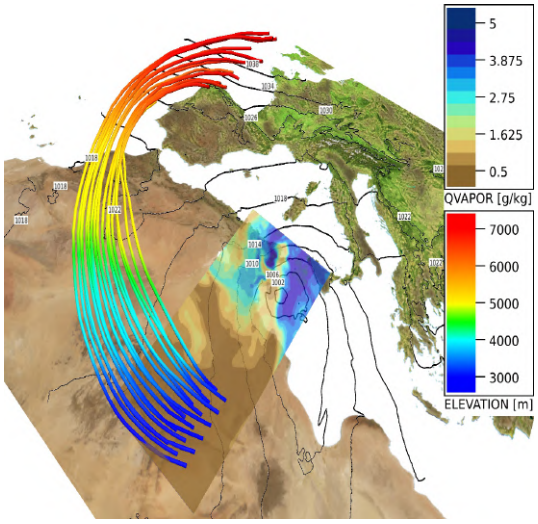

(b) Back-trajectories of 36h from 3000 m

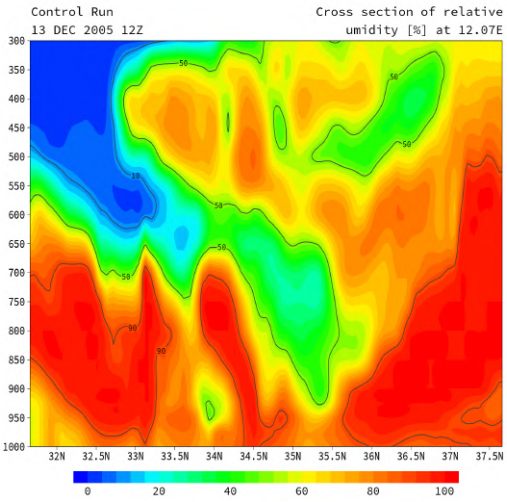

(c) 13 December 2005 - 12:00 UTC

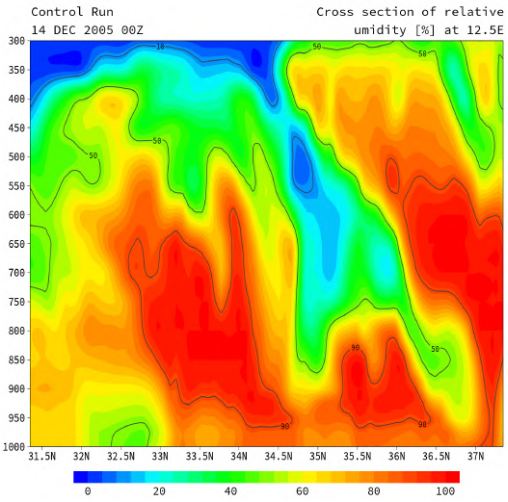

(d) 14 December 2005 - 00:00 UTC

Figure 4.13 – Dry air back-trajectory analysis at 700 hPa

ran Desert. Unfortunately, we can not have confirm of this evidence with the back-trajectory analysis. One weakness of the VAPOR software is that it hardly detects parcels that arise too close to the land and, even more so from the land itself as the case of the dust. Nevertheless, the main reason we can not legitimize the searching of parcels coming from the Saharan Desert itself is that our simulation do not take into account the presence of the aerosol or the dust of the desert. In this case, we should have used a model that at least take into account the aerosol, as WRF-Chem, that is a WRF model coupled with chemistry. WRF-Chem simulates the emission, transport, mixing, and chemical transformation of trace gases and aerosols simultaneously with the meteorology. The model is used for investigation of regional-scale air quality, field program analysis, and cloud-scale interactions between clouds and chemistry.

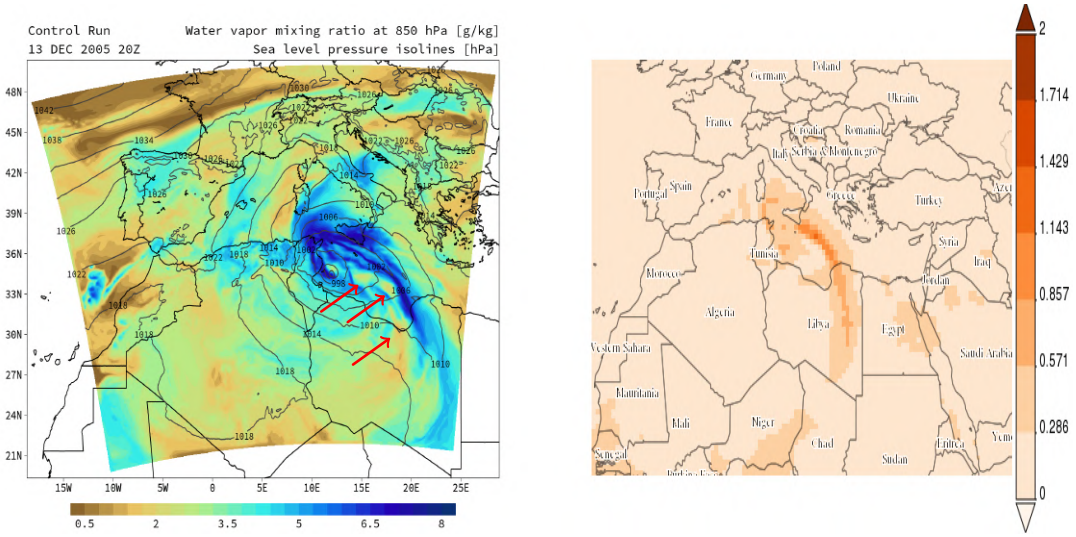

(a) 13 December 2005 - 20:00 UTC

(b) 13 December 2005 - 20:00 UTC

Figure 4.14 – Dry air at 850 hPa. Comparison with simulation and aerosol reanalysis

Rizza et al., 2017 [57] simulated an intense Saharan dust outbreak event that took place over the Mediterranean in May 2014.

4.5 Sensitivity tests with addition of water vapor

To understand the role of dry air in the initial and mature stage of the cyclone, new simulations with modified initial and boundary conditions were performed. Using an NCL script, the initial and boundary conditions provided by the metgrid WRF files, which contain the fields taken from ERA5 reanalysis, were modified in this way: in every file, values of Relative Humidity (RH) less than 50% were set to 50%. This threshold value was chosen as a compromise between making the atmosphere more humid but not so much as to bring the atmosphere locally close to saturation and cause the release of latent heat which could change the evolution of the cyclone dramatically. In this way, the experiments will explore how the change in mixing ratio, due to different water-vapor contents may affect the subsequent evolution. Three RH50 tests were performed and for every test a control run was performed, which is a run where the initial conditions were not modified: the first one, which we refer to as the '00Z11-RH50' test, starts at 00:00 UTC of 11 December 2005; the second, the '12Z11-RH50' test, starts at 12:00 UTC of 11 December 2005; the third, the '00Z12-RH50' test, starts at 00:00 UTC of 12 December 2005. Control runs are as '00Z11-CTL', '12Z11-CTL' and '00Z12-CTL', respectively.

The reason to perform the same sensitivity tests with modified initial conditions but with a time-lagged approach is explained in the following. We take the 00Z11-RH50 test as a reference point: after a few hours of this test, we see that there are some parts of the high troposphere rapidly becoming drier, well below the threshold initially imposed of RH=50% (figure

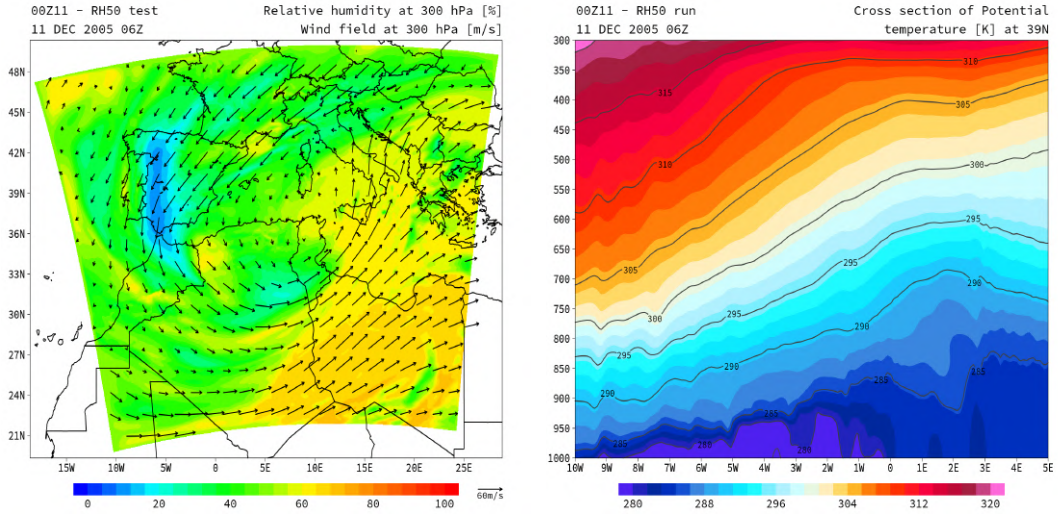

(a) (b)

Figure 4.15 – Relative humidity field at 300 hPa and θ cross section at 39° N for 00Z11-RH50 test

4.15). The same evolution is also observed at lower levels and at later times. In the troposphere over Spain there is a descent of air associated with lower stratospheric/upper tropospheric-air intrusion, visible in the vertical section of θ in figure 4.15b. If a parcel from the stratosphere descends, it will follow an isentropic surface towards lower altitudes (we suppose that only adiabatic, dry processes are at work), pressure and temperature of environment will increase, in order to keep θ constant, according to equation (4.1). Because the water vapor mixing ratio q_v remains nearly constant during that process, but the saturation water vapor mixing ratio varies due to the increase of temperature, equation (4.2) states that the value of relative humidity must decrease. This explains why values smaller than 50% are found in the RH50 tests.

$$\theta = T\left(\frac{p_0}{p}\right)^{\frac{R}{c_p}} \tag{4.1}$$

$$RH = \frac{q_v}{q_{v,SAT}(T)} \tag{4.2}$$

Thus, we expect that dry-air intrusions are responsible for a reduction of RH and partially offset the change imposed at the beginning. However, for simulations starting later, the descent of some parcels from the upper troposphere/lower stratosphere has already occurred (completely or partially) before the initial time of the run, affecting less the constraint on RH. This is relevant for our purposes, considering that the intrusions of dry air occurring earlier are those reaching the cyclone center first and affecting more directly the early stages of its development. For these reasons, we decided to analyze a set of different simulations starting at later times compared to the control run.

As we did with the No Fluxes test, we ensure that sea level pressure and 500 hPa geopoten-

tial fields in the sensitivity tests are not different with respect to the same fields at the moment when the cyclone is in the control run is in the preconditional phase (12:00 UTC of 12 December 2005). Analysis of figures of sea level pressure and geopotential field at 500 hPa in the area of interest (not shown), indicates acceptable differences (within 1 hPa in the area of cyclone development). Therefore, the analysis of RH50 tests can be accomplished assuming that the different evolution of the cyclone is not affected by a different structure of the atmosphere. Note also that the change in RH does not change the Potential Vorticity (PV) structure and values, which means that the interaction of PV streamers with the forming cyclone is not significantly modified, while only the change in RH is relevant.

4.5.1 Results of RH50 sensitivity tests

Figure 4.16 shows the IWV and sea level pressure isolines for the RH50 tests and homologous control runs at 18:00 UTC of 13 December 2005: the first column refers to control runs, the second column to RH50 tests and each rows refers to a specific test. On each control runs (figures 4.16a,c,e) the sea level pressure minimum forms in a relatively dry region: in fact, the minimum corresponds to values of IWV lower than values in the comma-like structure around it. The IWV and sea level pressure structures are very similar in each control run. We notice at this point that the control runs, performed with a time-lagged approach, do not have exactly the same evolution at each display time (e.g., at 18:00 UTC of 13 December 2005) and, as we will see better in other figures, differences of θ_e, sea level pressure and, in general, of all meteorological variables, exist among all of our control runs. These differences are due to the limit in the predictability, which can be particularly important in the case of Medicane simulations (Di Muzio et al., 2019 [14]; Davolio et al., 2009 [13]; Miglietta et al., 2015 [39]). Deterministic approaches, as the NWPs, are not able to perfectly predict nature and, even more so, a nonlinear system like the atmosphere. In addition, NWPs are extremely sensitive to different initial conditions (see Miglietta et al., 2015 [39]): in our control runs, the different initial conditions (00:00 UTC of 11 December, 12:00 UTC of 11 December and 00:00 UTC of 12 December) have the effect to change the simulated evolution of the same cyclone. Nevertheless, differences among control runs are limited, as we have seen in the IWV figure, and remain so also in the following time steps.

In contrast, the RH50 tests present remarkable differences in IWV and sea level pressure structures: in the 00Z11-RH50 test (figure 4.16b) the minimum of sea level pressure is about 992 hPa, covered by values of IWV around 18 mm; in the 12Z11-RH50 test (figure 4.16d) the comma-like structure of moist air coming southward has almost wrapped up the sea level pressure minimum at 18:00 UTC of 13 December. The fact that the cyclone has already developed an intense warm and moist core in its inner part prevents more dry air intrusion with respect to the behavior of the same structure at the same time in the 00Z11-RH50 test (figure 4.16b): in the 12Z11-RH50 test, the value of sea level pressure minimum is about 988 hPa and values

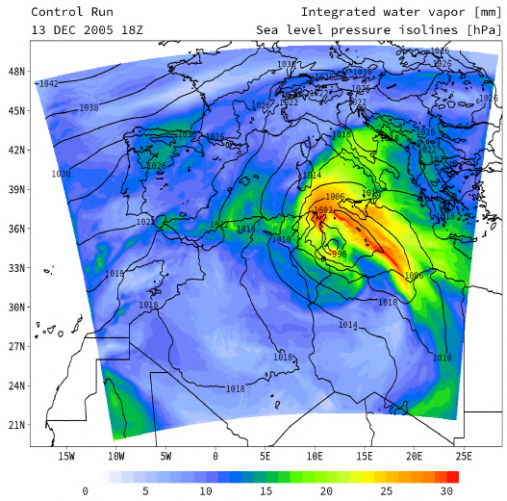

(a) 00Z11 - CTL run

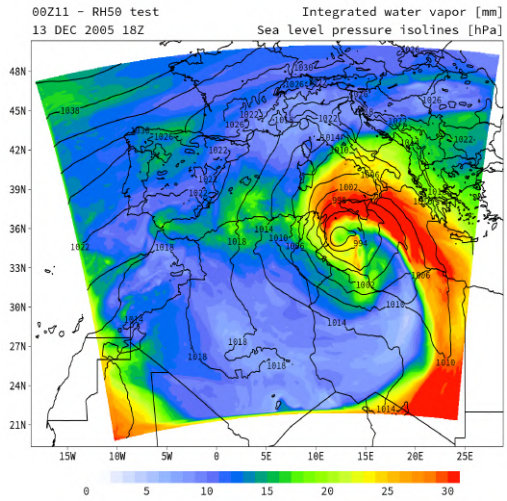

(b) 00Z11 - RH50 test

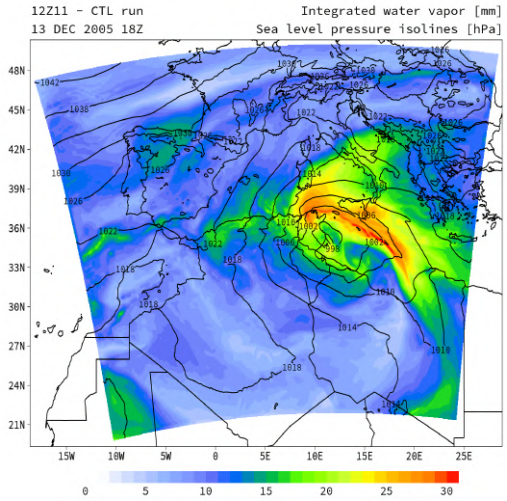

(c) 12Z11 - CTL run

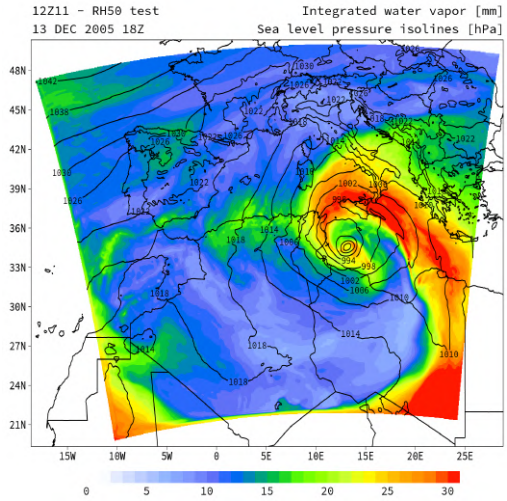

(d) 12Z11 - RH50 test

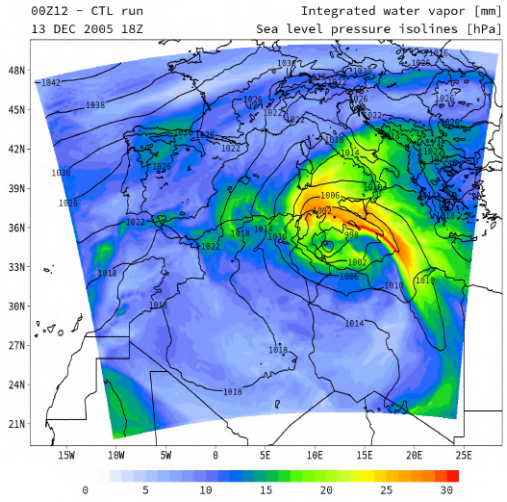

(e) 00Z12 - CTL run

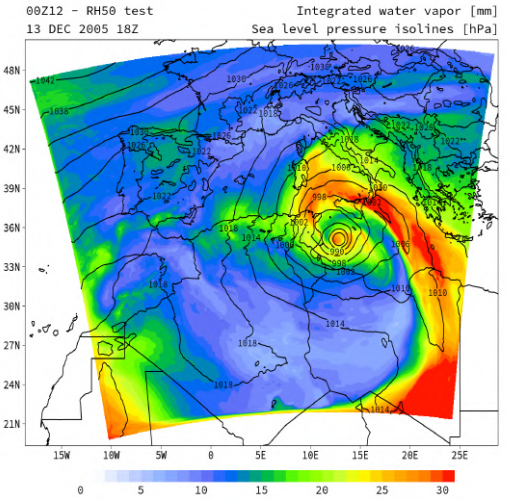

(f) 00Z12 - RH50 test

Figure 4.16 – Integrated water vapor with sea level pressure isolines in the control runs and RH50 tests

of IWV over it are around 22 mm. The third case, the 00Z12-RH50 test, depicts a more advanced comma-like structure (figure 4.16f) with respect to both 00Z11-RH50 and 12Z11-RH50 tests: sea level pressure minimum and IWV over it in the 00Z12-RH50 test are about 986 hPa and 26 mm. In summary, the RH50 tests show that the dynamics of formation of the cyclone are progressively faster with deeper values of sea level pressure minimum, at the same time, if the start of the simulation is postponed and closer to the event. These figures just discussed show, in fact, that if the atmosphere is drier, the formation of the cyclone is accelerated and more intense.

With regard to the different sea level pressure structures in the RH50 tests, figure 4.17 compares them in detail. It is evident how the intensity (and slightly also the dimension) increases from the 00Z11-RH50 test to 00Z12-RH50 test. However, to gain more confidence on the increase of the intensity in the RH50 cyclones, we can see the sea level pressure time evolution, shown in figure 4.18, and the wind speed maximum values time evolution at 10 m, shown in figure 4.19; both time evolutions are calculated in the same domain of figure 4.17 (legend is on the top-right of the figures). Minimum values of sea level pressure in the RH50 tests are always lower than the counterpart control runs. Figure 4.17 clearly shows that the later RH50 test starts, the more the cyclone can intensify. This fact is confirmed by the analysis of the wind speed maximum values time evolution at 10 m (figure 4.19): values in the RH50 tests are for most of the time higher than the control runs, especially after 06:00 UTC of 15 December, that is when the control run cyclones are in their dissipation phase: this evidence (that can be seen also in the sea level pressure time evolution after 06:00 UTC of 15 December) confirms that a more humid atmosphere induces a more favorable environment to the cyclone sustenance, delaying the cyclone dissipation.

Figure 4.20 shows 700 hPa θ_e fields at 12:00 UTC of 14 December 2005 for control runs, in the first column, and for RH50 tests, in the second column; each rows refers to a specific test. We again see in the control runs (figures 4.20a,c,e) that forming cyclones have nearly the same structure in all of them, with very close values of θ_e at the center of the cyclonic circulation; in all these runs, dry air can envelop, or even reach, the center of the circulation (12Z11-CTL cyclone in figure 4.20c); the mixing of the moist air with the dry air weakens the development of convection near the center, and intensifies the downdraft, which is known to be detrimental to the development of tropical cyclones. The RH50 tests show, instead, a more advanced stage in the cyclone development with respect to the counterpart control runs. On the other hand, observing in sequence figures 4.20b, d and f, cyclones present a faster formation at the same time and a better defined warm-core structure compared to the control runs starting at the same time. 12Z11-RH50 and 00Z12-RH50 cyclones (figures 4.20d and 4.20f respectively) present a cyclone center without dry air intrusion over it and relatively small amount of dry air around the center. Since the absence of deep convection in the mature stage has been stated in some observational studies (Miglietta et al., 2013 [41] Dafis et al., 2018 [12] Marra et al., 2019

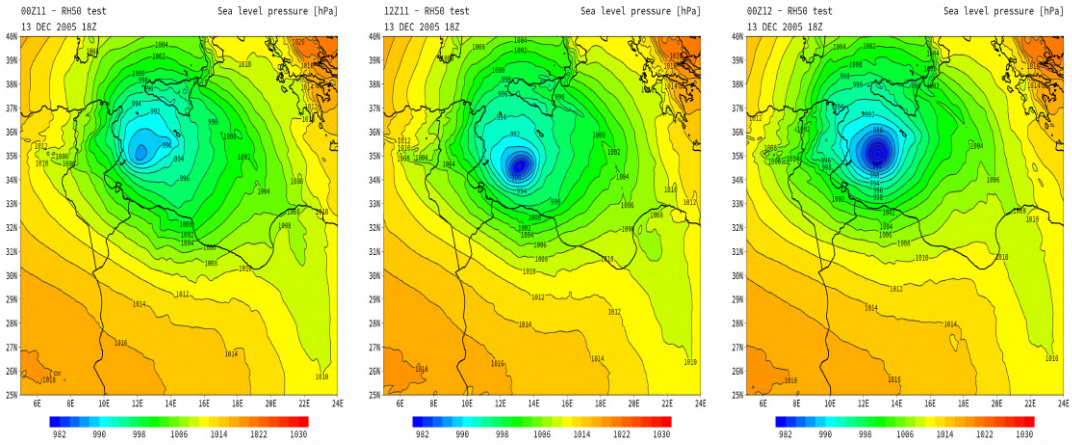

(a) 00Z11 - RH50 test (b) 12Z11 - RH50 test (c) 00Z12 - RH50 test

Figure 4.17 – Sea level pressure surfaces in the RH50 tests. Surfaces are plotted every 2 hPa.

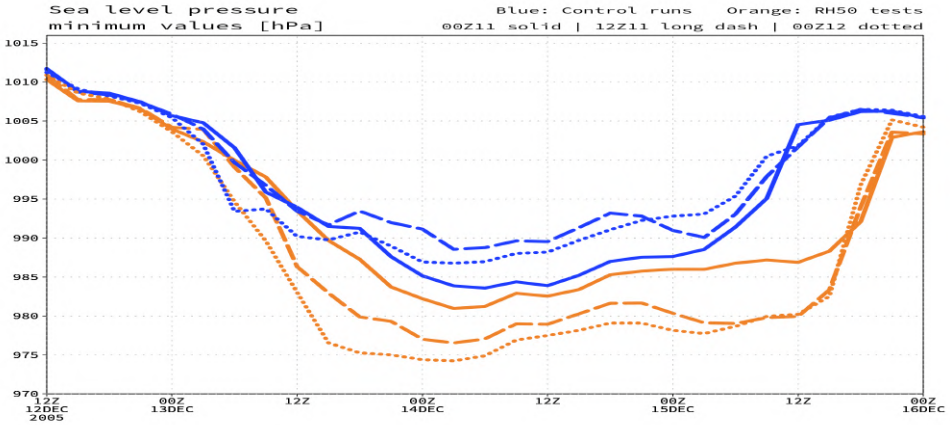

Figure 4.18 – Sea level pressure minimum values (every 3 hours) in the control runs and in RH50 tests

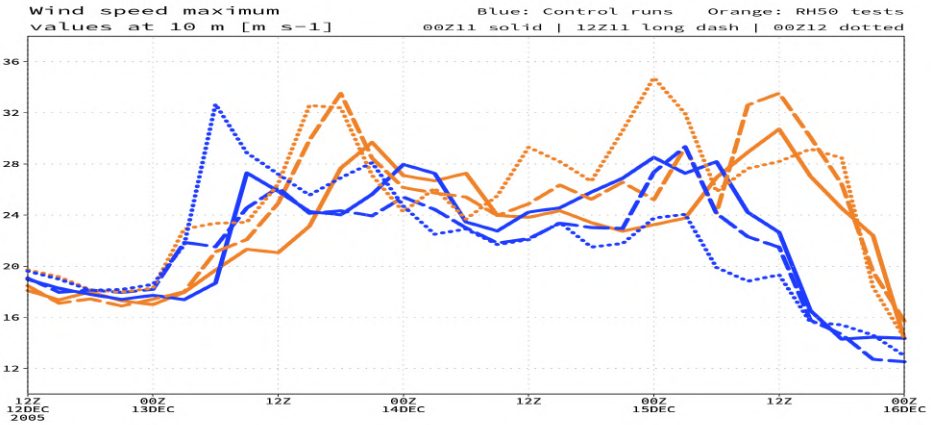

Figure 4.19: Wind speed maximum values (every 3 hours) at 10 m in the control runs and in RH50 tests

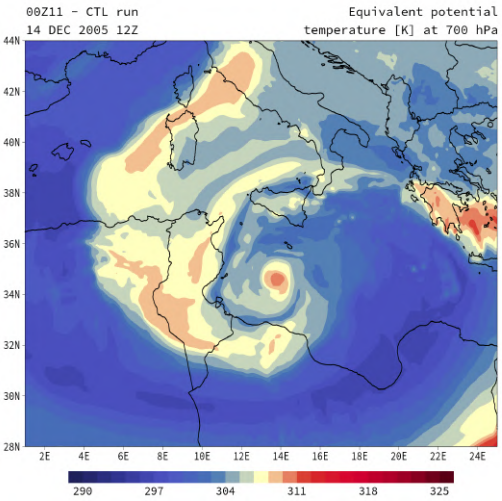

(a) 00Z11 - CTL run

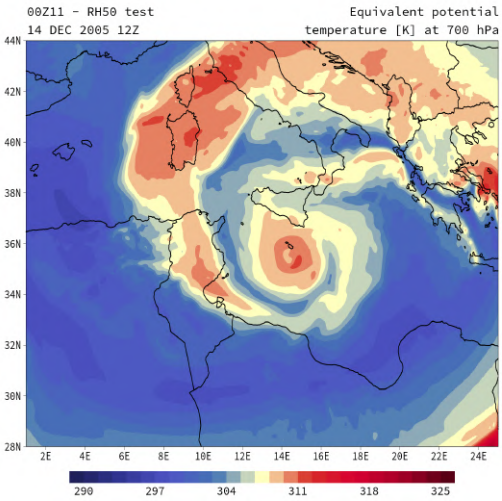

(b) 00Z11 - RH50 test

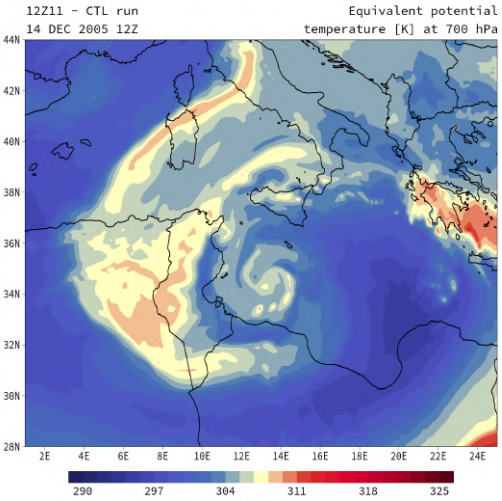

(c) 12Z11 - CTL run

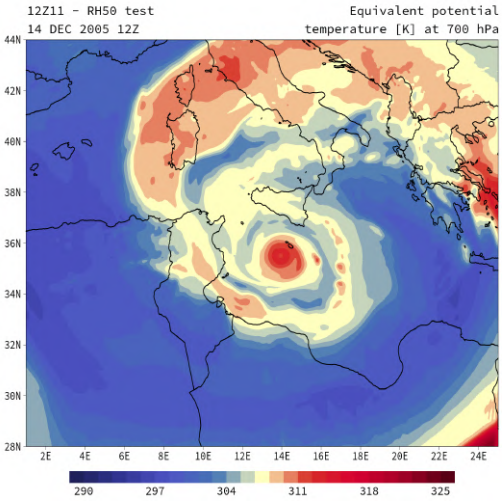

(d) 12Z11 - RH50 test

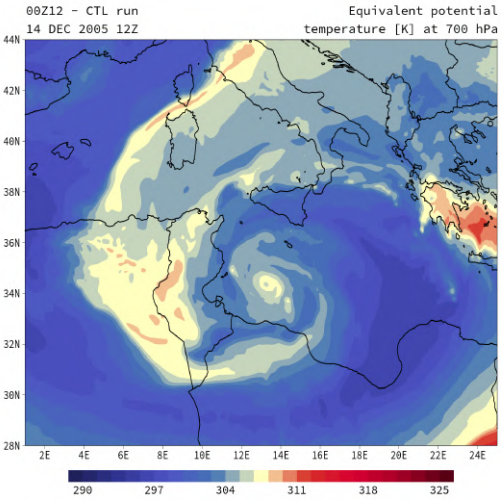

(e) 00Z12 - CTL run

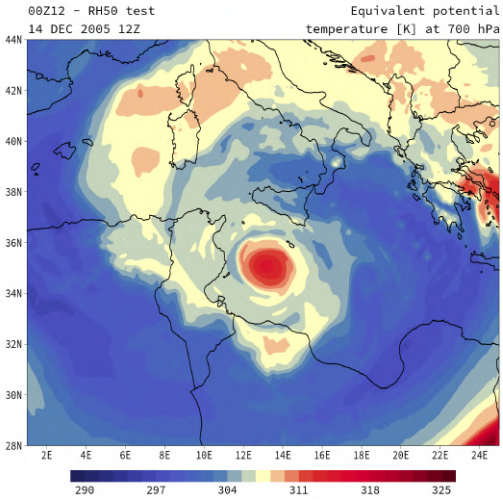

(f) 00Z12 - RH50 test

Figure 4.20 – θ_e fields at 700 hPa of control runs and RH50 tests

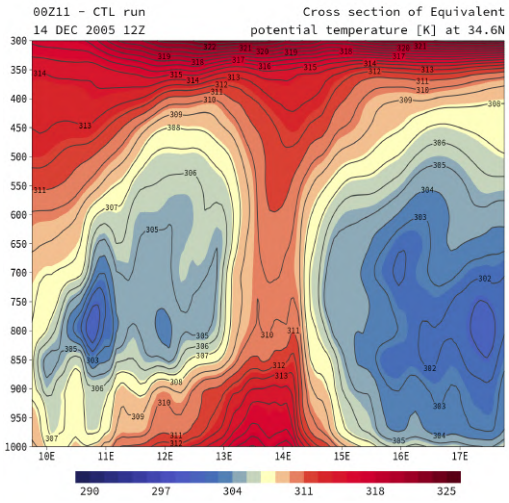

(a) 00Z11 - CTL run (center at 13.75° E)

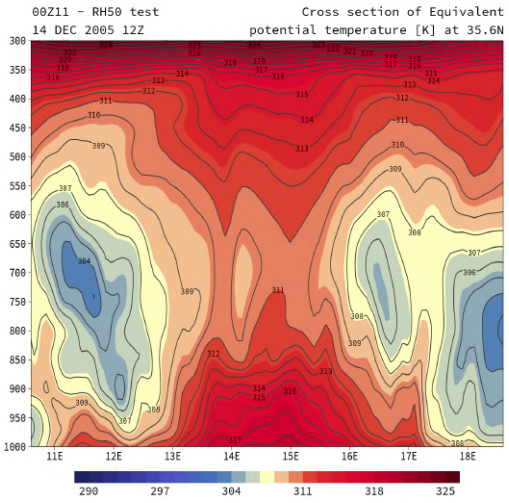

(b) 00Z11 - RH50 test (center at 14.6° E)

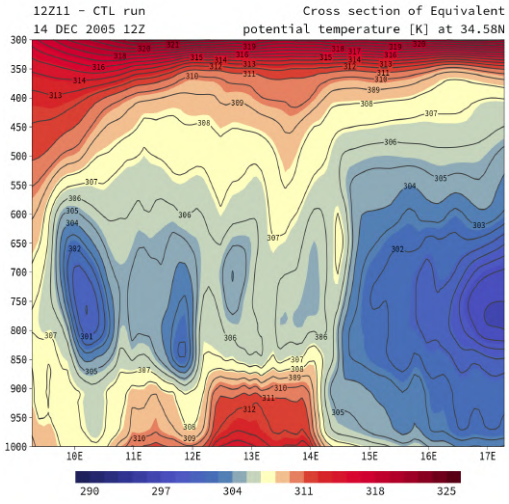

(c) 12Z11 - CTL run (center at 13.28° E)

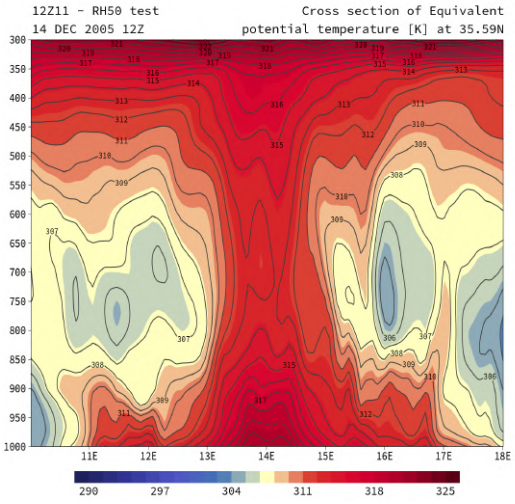

(d) 12Z11 - RH50 test (center at 14° E)

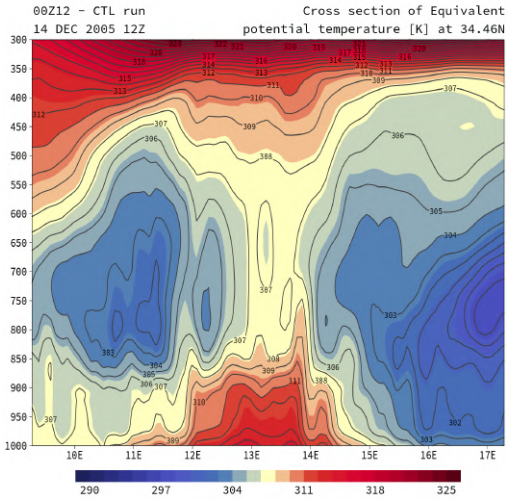

(e) 00Z12 - CTL run (center at 13.28° E)

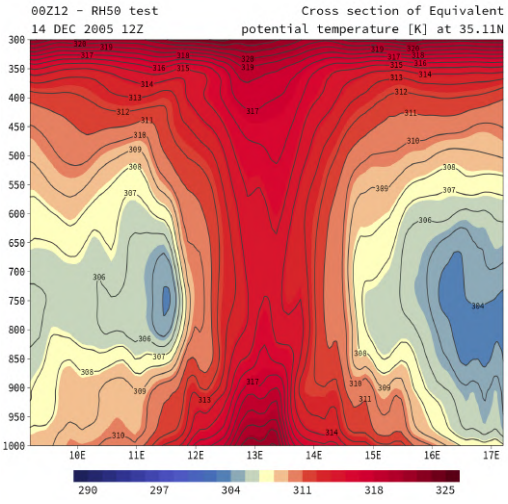

(f) 00Z12 - RH50 test (center at 13.2° E)

Figure 4.21 – θ_e cross sections of control runs and RH50 tests

[37]), we postulate that the dry air intrusion can contribute to create a less favorable environment for cyclone development. Also, the presence of more humid air around a well-defined warm core may promote the increase of the horizontal size of the cyclone and thus the duration of the cyclone. The latter considerations can be better appreciated in figure 4.21, which follows the same representation scheme as figure 4.20 (the center of the cyclones is identified by the minimum value of sea level pressure and the longitudinal coordinate is specified in the related caption). The RH50 cyclones (figures 4.21b,d,f) show an advanced formation stage with warm-core more defined from the 00Z11-RH50 test to 00Z12-RH50: θ_e values at 700 hPa are about 311 K, 313 K and 315 K for the 00Z11-RH50, 12Z11-RH50 and 00Z12-RH50 cyclone respectively. The values of the colder and drier air at the border are very different in each experiment, between the control run and the RH50 test, suggesting that the mixing of warm air near the center with the drier air at the borders is less effective in the RH50 tests. Figures 4.21b,d,f show, again, that an increase of humidity content in the whole atmosphere in the preconditioning phase of cyclone formation allows a faster development, a more define vertical structure and a slightly wider horizontal extension.

5 | Medicane Cornelia

A nontropical low over the western Mediterranean developed, moved eastward and gradually became a warm-core system that assumed tropical characteristics. On 7 October its center was between the Balearic Islands and Sardinia with 114 km/h wind gusts and was classified as Mediterranean tropical storm *Cornelia*. The storm made landfall in the evening in central Sardinia. It quickly reached category 1 on the SSHS the same day in the Tyrrhenian sea. After loosing most of its strength, it made a landfall near the Messina strait, then, reached the Ionian sea with tropical depression intensity. After that it gained new strength, reaching tropical storm intensity just west of Crete. It dissipated over the western Mediterranean on 11 October. Cornelia caused strong winds, damage and floods over the Balearic Islands, Sardinia and southern Italy, and devastated the Aeolian Islands with 145 km/h winds on 9 October. In the early stages, the storm showed distinct signs of tropical-cyclone-like behavior. The eye-like feature can be seen in figure 5.1b.

The simulation with WRF4.1 lasts from 00:00 UTC of 4 October 1996 to 00:00 UTC of 10 October 1996. The model integration domain has a horizontal grid spacing of 9 km and 40 vertical levels, more closely spaced in the boundary layer. The grid is centered at 38°N, 6°E and has 400 × 300 horizontal grid points. ERA5 reanalysis were used. In the early stages, the simulated trajectory in figure 5.2 is in accordance with another work (Miglietta and Rotunno, 2019 [42]).

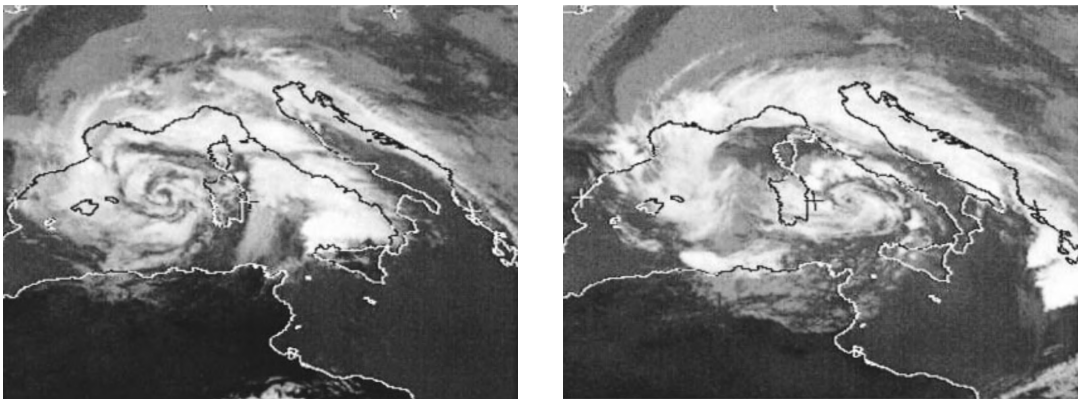

(a) 7 October 1996 - 11:30 UTC

(b) 8 October 1996 - 15:00 UTC

Figure 5.1 – Medicane Cornelia images in the infrared bandwidth, from the METEOSAT-5 satellite

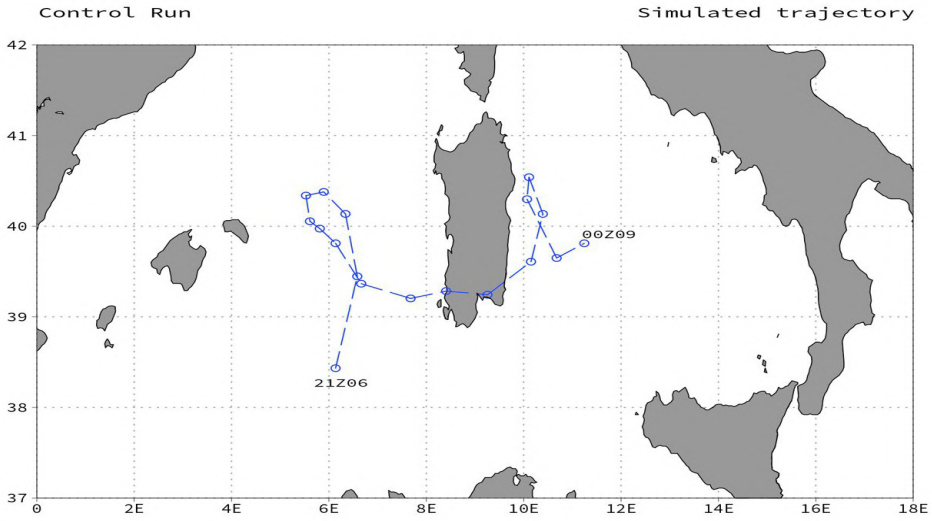

Figure 5.2 – Simulated trajectory of Medicane Cornelia - points every 3 hours

5.1 Initial conditions

As we did with Medicane Zeo, we will start by describing the state of the atmosphere before the formation of the cyclone. In figure 5.3 the temperature field and the geopotential at 500 hPa are shown on the left, while the sea level pressure on the right. The temperature field shows a deep trough over northern France (figure 5.3a) moving southward and forming an upper-level cut-off over the Balearic Islands (figure 5.3c). The environment was characterized by a strong westerly jet to the south of the storm (Reale and Atlas, 2001 [56], figure 20), which played a key role in its development by barotropic instability. In the lowest troposphere, a thermal depression in northwestern Africa mainland was forming (figure 5.3b), growing northward and intensifying over the western Mediterranean basin (figure 5.3d), in conjunction with the cut-off low formation at the upper levels.

To analyze moist and wet air masses before the cyclone formation, figure 5.4 shows the equivalent potential temperature and the wind field both at 700 hPa on the left, and the water vapor mixing ratio at 700 hPa with sea level pressure contours on the right. Strong intrusions of cold and dry air from northern Europe in the medium troposphere is clearly visible in figures 5.4a,c. Figures 5.4b,d show large values in the water vapor field over the Balearic Islands, associated with the arrival of a front from northern Europe, while, from the south-west region of Africa mainland, a tongue of moist air partially reaches the Balearic region.

In all (a) and (b) subfigures, the remnant of a previous baroclinic mesocyclone vortex over southeastern Italy in its dissipating stage is distinctly visible; additional analysis suggests that the presence of this residual cyclone does not significantly affect the environment of the cyclone Cornelia.

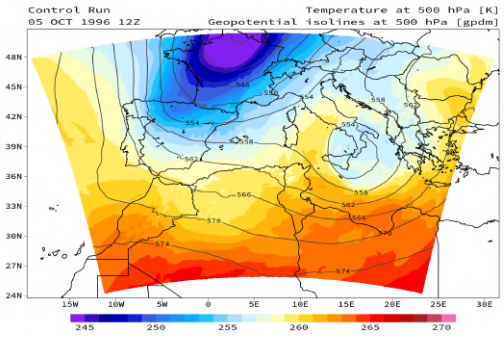

(a) 5 October 1996 - 12:00 UTC

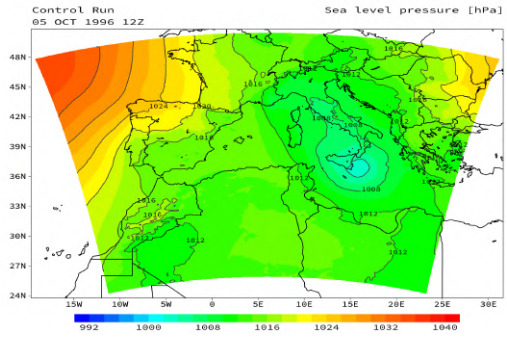

(b) 5 October 1996 - 12:00 UTC

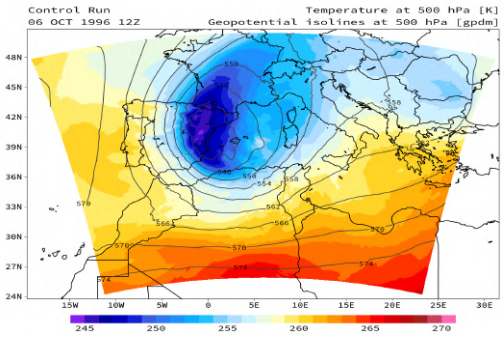

(c) 6 October 1996 - 12:00 UTC

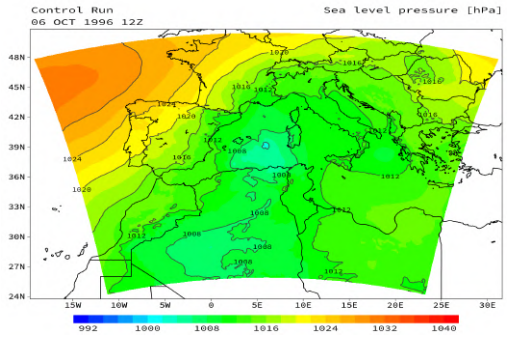

(d) 6 October 1996 - 12:00 UTC

Figure 5.3 – Control run temperature field at 500 hPa and sea level pressure surfaces

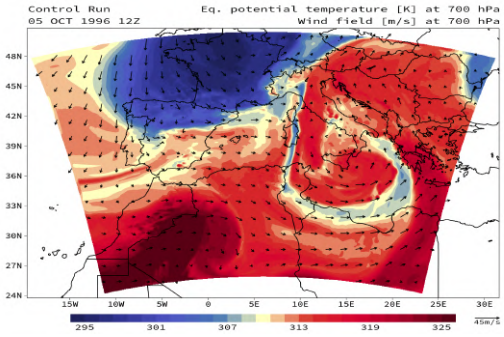

(a) 5 October 1996 - 12:00 UTC

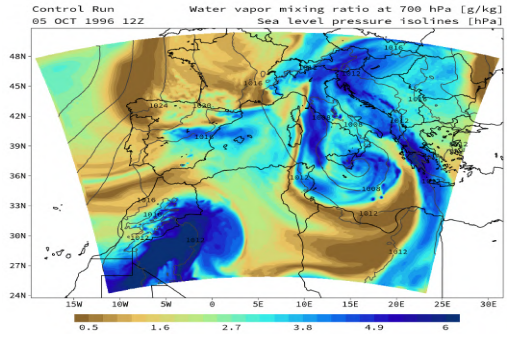

(b) 5 October 1996 - 12:00 UTC

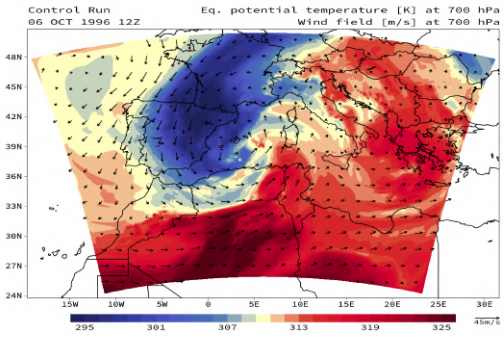

(c) 6 October 1996 - 12:00 UTC

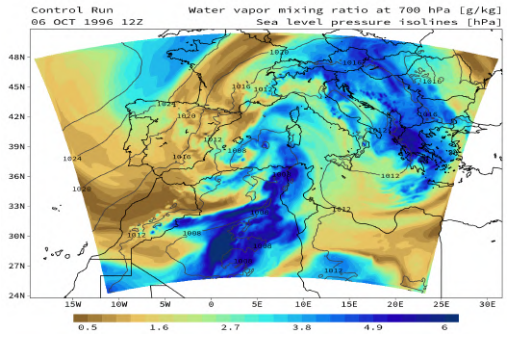

(d) 6 October 1996 - 12:00 UTC

Figure 5.4 – Control run θ_e field at 700 hPa and water vapor mixing ratio at 700 hPa

5.2 Moist air masses analysis

We analyzed moist air flows in the preconditioning phase of the cyclone to see, as we did for Medicane Zeo, whether the humidity transport or the evaporation favors a suitable environment for cyclone formation. Figure 5.5 shows, in the first row, water vapor mixing ratio at 950 hPa (figure 5.5a) and latent heat fluxes from surface (figure 5.5b), 30 hours after the simulation starts. Figure 5.5a shows large amount of water in the lower troposphere off the southern Sicilian coast because of the presence of the mesocyclone vortex with a narrow flow of moist air coming from the Tropical regions. In contrast, the water vapor mixing ratio field over the Balearic region is quite uniform and the air less moist. Latent heat fluxes of the remnant cyclone over southern Italy are visible off the coast of Tunisia, while weaker fluxes arise

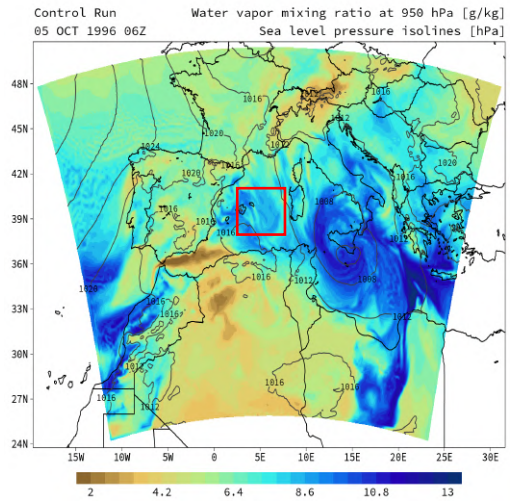

(a) 5 October 1996 - 06:00 UTC

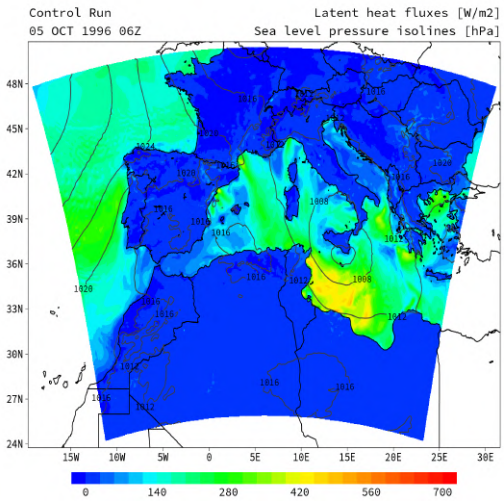

(b) 5 October 1996 - 06:00 UTC

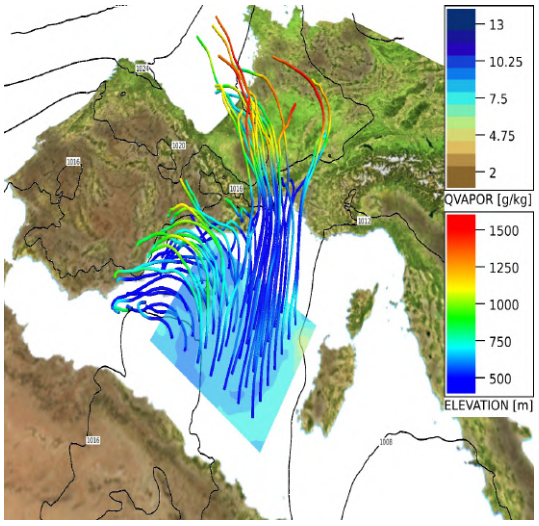

(c) Back-trajectories of 30h from 500 m

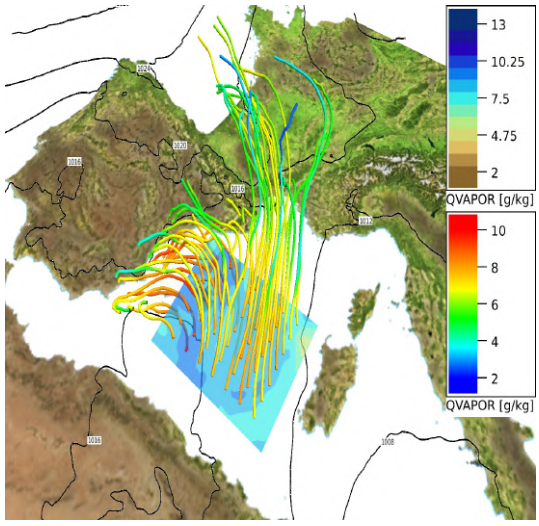

(d) Back-trajectories of 30h from 500 m

Figure 5.5 – Moist air back-trajectory analysis at 950 hPa

over the Balearic region due to tramontane wind through the Gulf of Lion and cierzo wind across the Spanish coast (figure 5.5b). To better detect the origin of the latter water vapor field, we use again back-trajectory analysis. The second row of figure 5.5 shows back-trajectories from 500 m over the Balearic region; elevation and water vapor mixing ratio field are superimposed on back-trajectories in figure 5.5c and 5.5d, respectively. Back-trajectories show a predominant flow directions associated with tramontane, coming from the north European mainland through the western Mediterranean basin. Back-trajectories come from low altitudes (1000-1500m in figure 5.5c) and are associated with low values of water vapor mixing ratio; when the air flows over the Mediterranean Sea, it gains water vapor due to evaporation (figure 5.5), as also confirmed by the intensification of the latent-heat fluxes, (see narrow-green

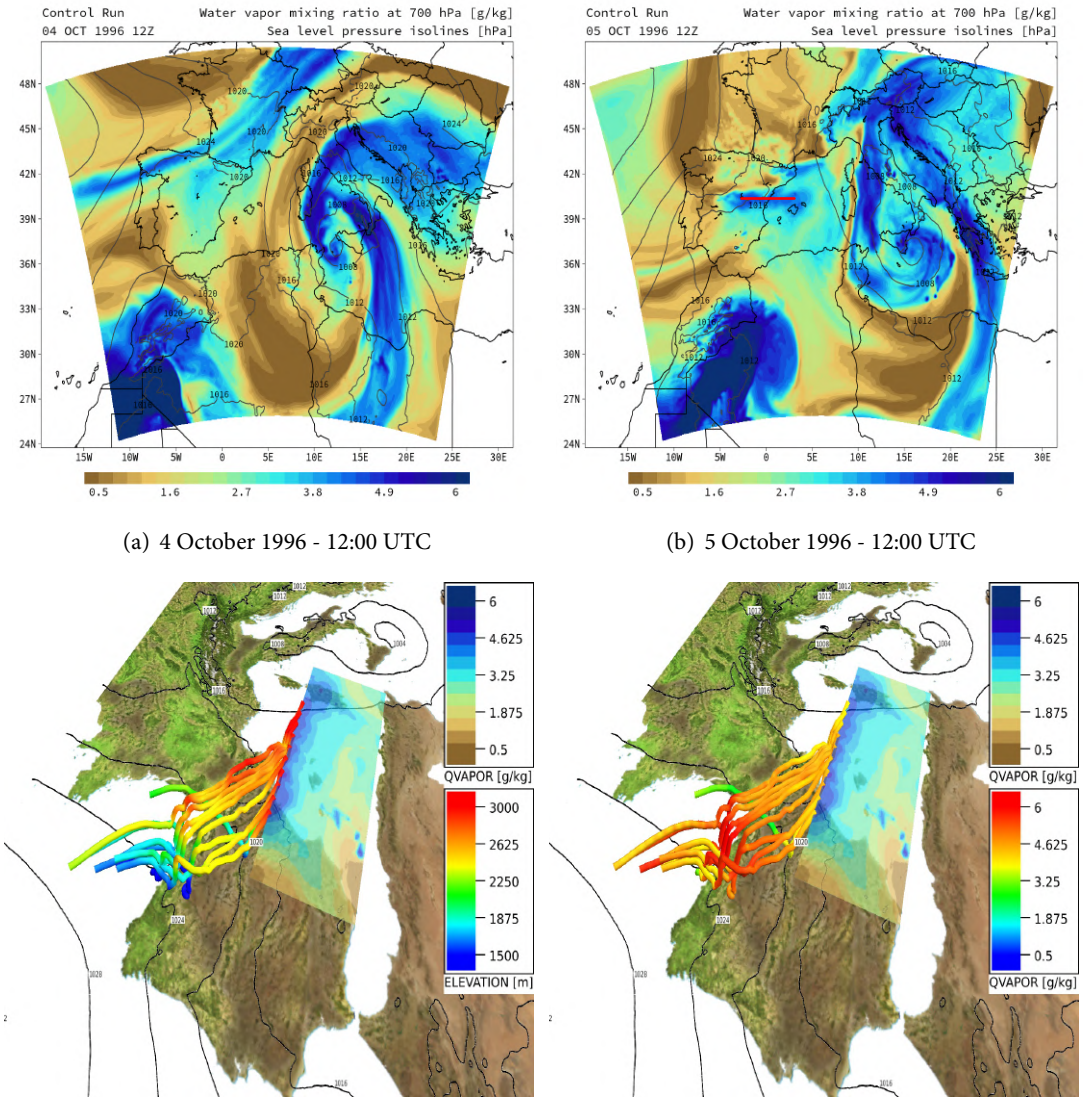

(a) 4 October 1996 - 12:00 UTC

(b) 5 October 1996 - 12:00 UTC

(c) Back-trajectories 36h from 3000 m

(d) Back-trajectories 36h from 3000 m

Figure 5.6 – Moist air back-trajectory analysis at 700 hPa

zone over the Balearic region in figure 5.5b). Beside this main flow direction, a significant number of back-trajectories with high value of water vapor mixing ratio show that humidity is increased within the Balearic region due to evaporation (see shorter back-trajectories south of Spain).

Now we move to the midtroposphere: figure 5.6 shows, in the first row, the water-vapor mixing ratio at 700 hPa at 12:00 UTC of 4 October (figure 5.6a) and at 12:00 UTC of 5 October (figure 5.6b); figure 5.6b refers to 36 hours after the simulation starts. Figure 5.6a indicates a well defined frontal structure coming from the North Atlantic toward the Mediterranean basin. Due to the frontal mechanisms, this structure humidifies the whole atmospheric column. After 24 hours (figure 5.6b), the frontal structure loses its coherence, due to the passage

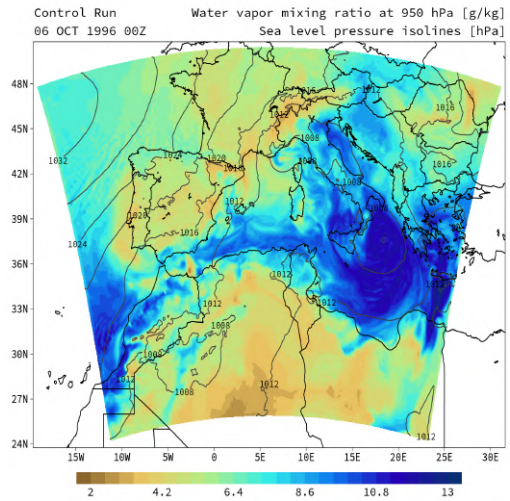

(a) 6 October 1996 - 00:00 UTC

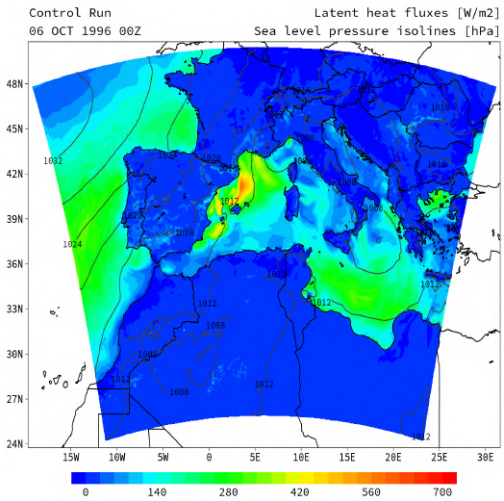

(b) 6 October 1996 - 00:00 UTC

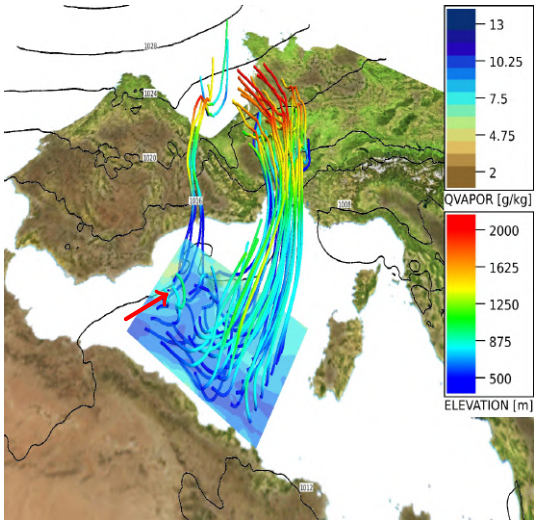

(c) Back-trajectories or 24h from 500 m

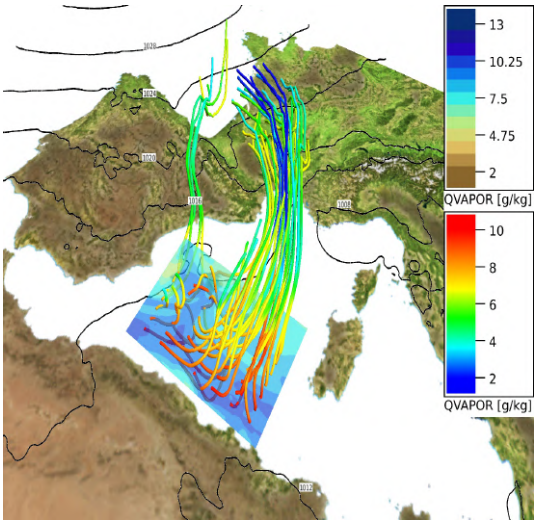

(d) Back-trajectories of 24h from 500 m

Figure 5.7 – Moist air back-trajectory analysis at 950 hPa

over the Europa mainland. However, a clear spot of moist air in the midtroposphere is still clear visible over the Balearic region (figure 5.6b). We can use the back-trajectory to detect this long-range contribution. The second row of figure 5.6 shows back-trajectories from 3000 m over the Balearic region; elevation and water vapor mixing ratio fields are superimposed on back-trajectories in figure 5.6c and 5.6d, respectively. As we can see, this air forms the remaining of the frontal system. In figure 5.6c, air is suddenly lifted up from 1500 m to near 3000 m due to the cold front mechanisms. Air parcels are, 36 hours before their arrival over Balearic region, almost all with relatively high values of water vapor mixing ratio (see figure 5.6d), Thus, the cold front pushes air parcels up and toward the Mediterranean basin, destabilizing the atmospheric column. This fact, in addition with moist air over the Balearic region (figure 5.6b), forms a strong gradient of humidity.

At 48 hours after the start of the simulation, the latent-heat fluxes from the sea surface over the Balearic region intensify. Figure 5.7 shows in the first row, the water-vapor mixing ratio at 950 hPa (figure 5.7a) and latent heat fluxes from surface (figure 5.7b). Observing both paths of the tramontane wind blowing trough the Gulf of the Lion and cierzo wind from Spain, we can see that the wind breaks in as dry air and acquires moisture during its passage over the sea due to latent-heat flux from sea surface (figure 5.7b). As a consequence, a dry region is initially observed over the Gulf of Lion and a moist region forms off the coast of Algeria (figure 5.7a). This mechanism is confirmed with the back-trajectory analysis. The second row of figure 5.7 shows back-trajectories from 950 m over the Balearic region; elevation and water vapor mixing ratio field are superimposed on back-trajectories in figure 5.7c and 5.7d, respectively. We can see that water vapor mixing ratio field over Balearic region has its main origin from the outbreak of northerly winds. But, in addition, there are a small number of really short streamlines (i.e., relating to air parcels that have been there for a maximum of 24 hours in this case) that are already formed within the Balearic region (indicated with the red arrow), as we have already noted in figure 5.5b but, this time, not so much identifiable due to predominant role of the outbreak of northerly winds. It interesting to note that some air parcels, once they reach the coasts of Algeria, deviate suddenly their paths from their original north-south direction to the east-west. This fact, that can explain the accumulation of water vapor off the coasts of Algeria, is most likely due to the flow blocking by the Atlas Mountains.

To conclude the moist air masses analysis, we want to inspect the contribution of a moist air masses coming from the Tropics. Figure 5.8 shows in the first row, the water-vapor mixing ratio at 700 hPa (figure 5.8a) and the wind field at the same time and at the same isobaric level (figure 5.8b). As we have noted discussing about conditions of the atmosphere before the development of the medicane Cornelia in section 5.1, a tongue of moist air coming from the Tropics seems to be heading towards the Balearic area. Figure 5.8a shows, indeed, a wide area of moist air over the Africa mainland approaching the Balearic region while the cyclone is forming. Wind field at 700 hPa (figure 5.8b) and back-trajectories (figure 5.8c) confirm this large-scale transport

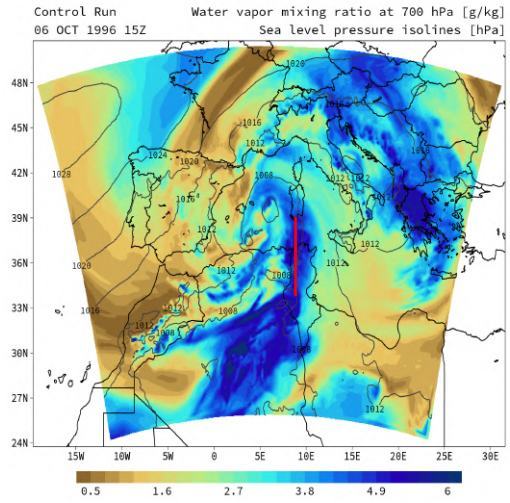

(a) 6 October 1996 - 15:00 UTC

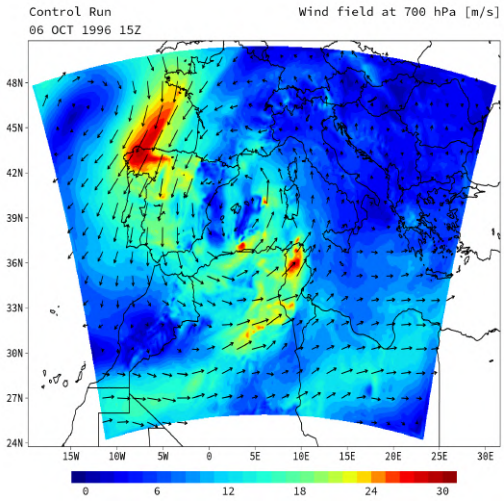

(b) 6 October 1996 - 15:00 UTC

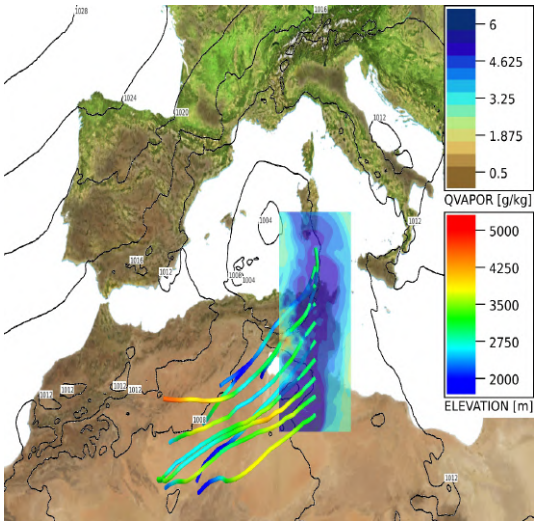

(c) Back-trajectories of 12h from 3000 m

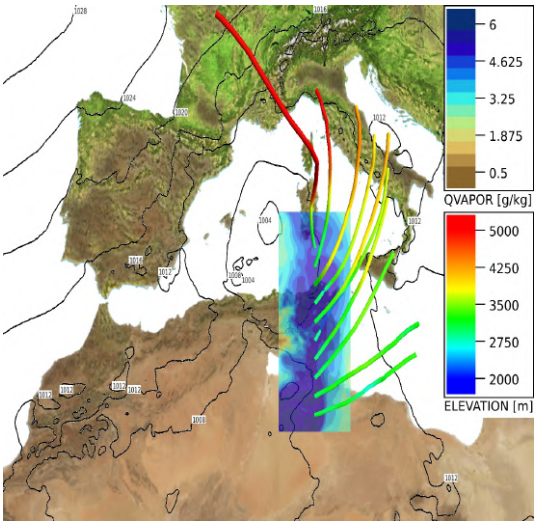

(d) Forward-trajectories of 12h from 3000 m

Figure 5.8 – Moist air back-trajectory analysis at 700 hPa

from the Tropics toward the Mediterranean basin. Despite this, forward-trajectory analysis (figure 5.8d) shows that almost every streamlines diverge eastward, not contributing to water vapor content over the cyclogenic area. Additional analysis of water vapor mixing ratio at 700 hPa (not shown) confirm the marginal role of this southern long-range moist transport into the medicane dynamics.

5.3 Sensitivity tests without surface fluxes

The previous back-trajectory analysis suggests that two main source of water vapor humidify the lower layers of the troposphere, which are the local evaporation (noted especially in figure 5.5c in the preconditioning phase) and dry-air intrusion in western Mediterranean

basin that triggers heat fluxes from the sea surface (figures 5.5c and 5.7d in the preconditioning and initial phases of the cyclone formation, respectively). To examine the importance of these two contributions, two sensitivity tests were done.

5.3.1 First sensitivity test

The first sensitivity test investigates the role of the heat fluxes and the local evaporation on the western Mediterranean basin in the preconditioning phase, which is from the start of the simulation (00:00 UTC of 4 October 1996) until the beginning of the intensification of the heat fluxes over the sea (06:00 UTC of 5 October 1996). From this point of view, we will refer to this test as 'I No Fluxes' test. Sensible- and latent-heat fluxes were turned off, throughout the whole domain, in the first 30 hours of simulation with respect to the control run, and then turned on again until the end.

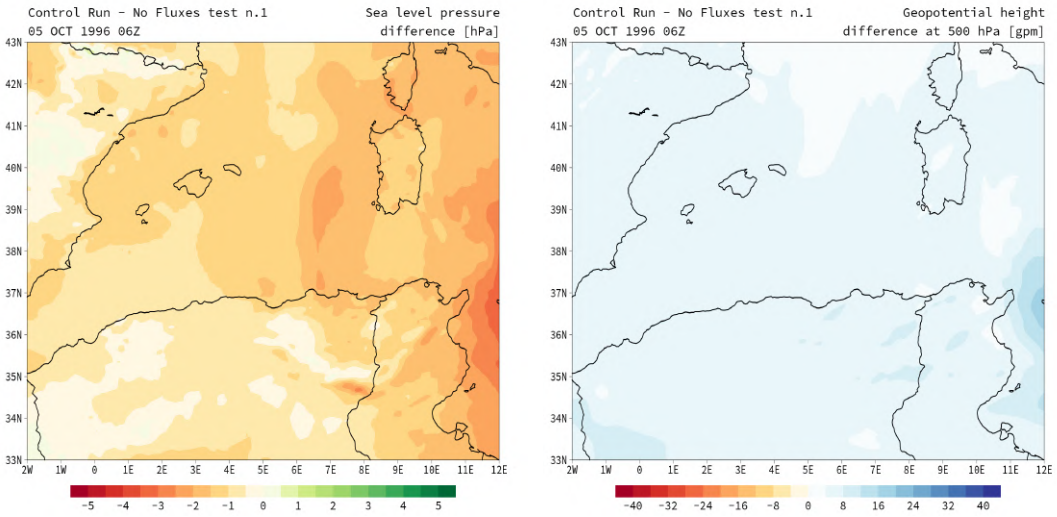

(a) (b)

Figure 5.9: Isobaric and geopotential height differences between the control run and the I No Fluxes test

As we did with Medicane Zeo, we briefly verify that the isobaric and geopotential fields of the I No Fluxes test do not significantly change with respect to the control run at the time when the fluxes were turned back on in the I No Fluxes test. Figure 5.9 shows, on the left, the sea level pressure differences between the control run and the I No Fluxes test over the region where the cyclone will form; same procedure was applied for the geopotential height difference at 500 hPa, on the right. Differences of the sea level pressure are limited between 1 and 3 hPa, in absolute value, over the Balearic region (figure 5.9a) and greater differences can be detected off the Tunisian coast, due to the presence of a cyclone that, however, does not affect the environment of the Cornelia medicane. Analogous considerations can be done with reference to figure 5.9b, where differences are less than 10 gpm. We conclude that the sea level

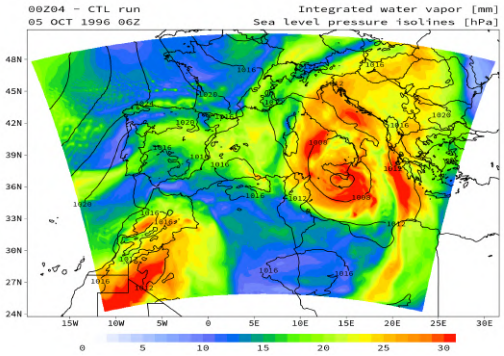

(a) 5 October - 06:00 UTC

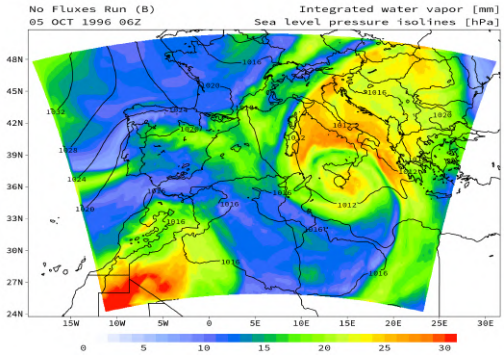

(b) 5 October - 06:00 UTC

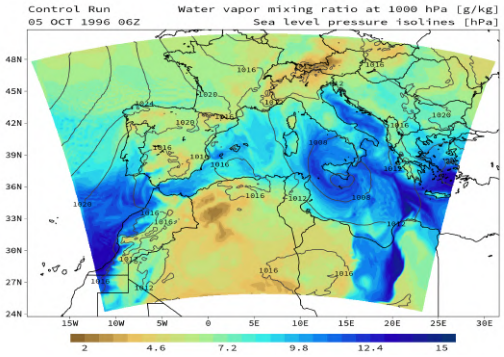

(c) 5 October - 06:00 UTC

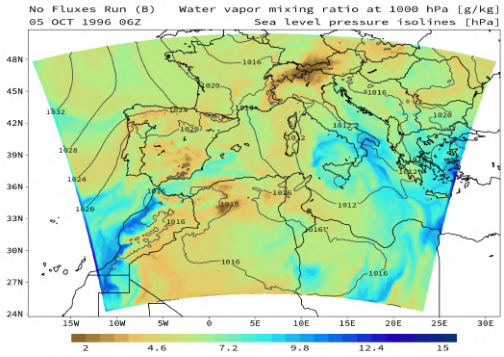

(d) 5 October - 06:00 UTC

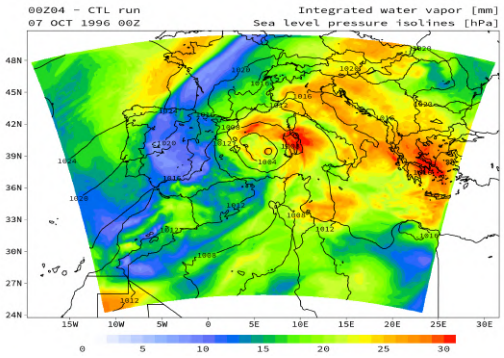

(e) 7 October - 00:00 UTC

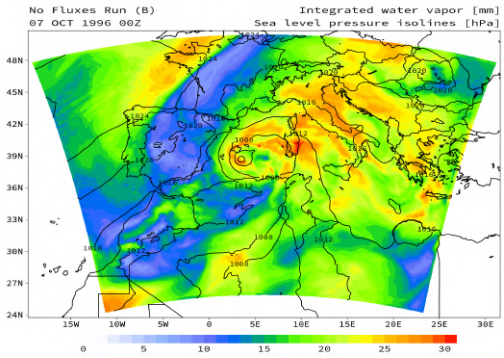

(f) 7 October - 00:00 UTC

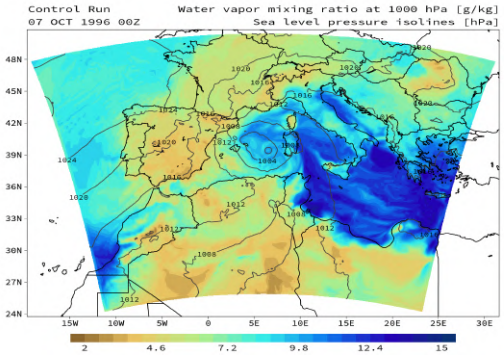

(g) 7 October - 00:00 UTC

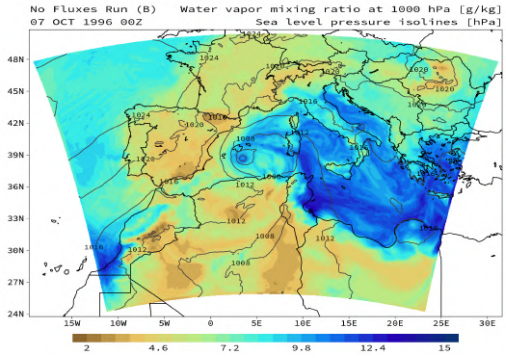

(h) 7 October - 00:00 UTC

Figure 5.10: Integrated water vapor and water vapor mixing ratio at 1000 hPa in the control run and I No Fluxes test

pressure and the geopotential fields were not significantly affected by the sensitivity experiment and possible differences in the evolution of the cyclone can be related to the content of atmospheric humidity.

In figures 5.10a,b are shown the IWV and the water vapor mixing ratio at 1000 hPa in figures 5.10c,d; figures on the left are referred to control run and to I No Fluxes test on the right. Figures 5.10b and d are referred to the times when the fluxes were turned on in the sensitivity experiments. Maximum values of IWV are over Sicily because there is the previous cyclone; focusing over the Balearic region, a reduction in the IWV content can be noted due to the turning off of the heat fluxes (figures 5.10a,b). More marked differences can be noted in water-vapor mixing ratio in the lowest troposphere (figures 5.10c,d): turning off the heat fluxes has a dramatic effect over the Ionian region, where the first cyclone is still active, and in a smaller way also in the Balearic region, where the humidity is uniformly reduced. After 42 hours, the cyclone is in its forming stage in the control run and also in the sensitivity I

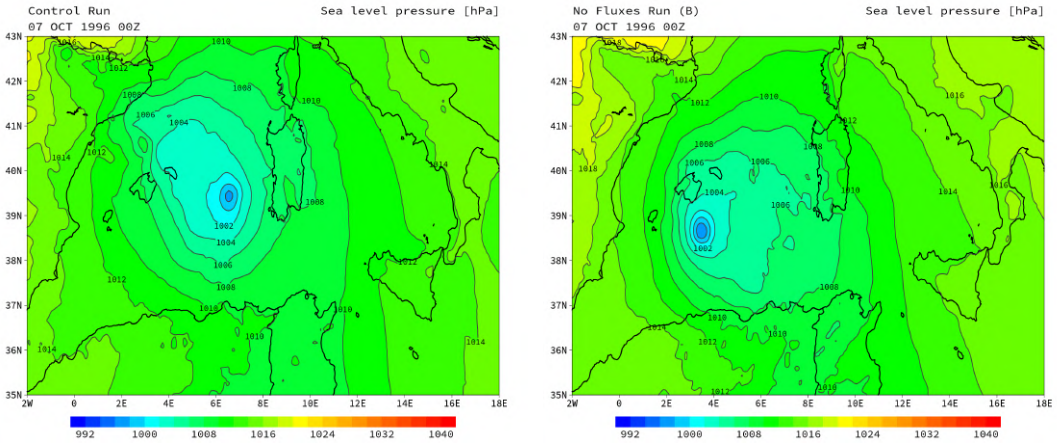

(a) 7 October 1996 - 00:00 UTC

(b) 7 October 1996 - 00:00 UTC

Figure 5.11 – Sea level pressure isolines in the control run and I No Fluxes test

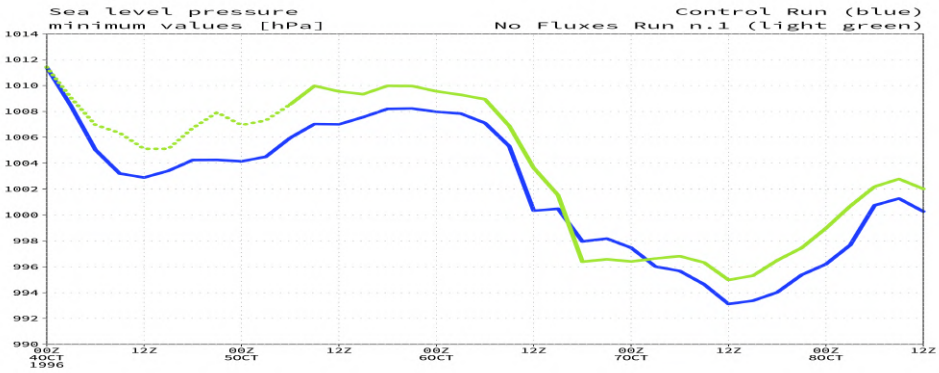

Figure 5.12: Sea level pressure minimum value (every 3 hours) in the control run and in I No Fluxes test. Dotted part refers to simulation without surface heat fluxes.

No Fluxes test: when the heat fluxes are turned on, the atmosphere in the sensitivity test has relatively less water vapor, hence the fluxes can compensate the humidity gap with greater release of water vapor. Figures 5.10e,f and 5.10g,h respectively show minor differences in values, compared to those at 06:00 UTC of 5 October 1996. Figures 5.11a,b show control run and sensitivity test cyclones at 00:00 UTC of 7 October 1996; nevertheless the absence of heat fluxes in the preconditional phase, the cyclone in the sensitivity test is able to form almost at the same time of the control run cyclone, even if with different trajectory. Figure 5.12 shows the overall sea level pressure minimum trend of the control run and the sensitivity test. Values of sea level pressure are calculated in the same domain of figures 5.11. The absence of surface heat fluxes in the preconditional phase generates a cyclone slightly less intense in the initial phase (approximately at 12:00 UTC of 6 October 1996); but the sensitivity cyclone continues to intensify with nearly the same rate of the control run cyclone or even more intensely. However, the sensitivity cyclone remains less intense of the control run (figure 5.11, at 12:00 of 7 October 1996 and beyond). With this first test it may be concluded that the release of water vapor in the lower troposphere, associated with evaporation and heat fluxes from the sea surface in the early stages of the cyclone lifetime, plays a minor role in cyclone formation and further intensification.

5.3.2 Second sensitivity test

The second sensitivity test examines the contribution of the heat fluxes at the time of cyclone formation. This test has been applied to complement the previous test, to better understand the role of heat fluxes in the Medicane Cornelia case-study. Sensible and latent heat fluxes have been maintained from the start of the simulation until 18:00 UTC of 5 October 1996, which is when the heat fluxes begin to intensify over the sea. Then, sensible- and latent-heat fluxes were turned off, throughout the whole domain, for 24 hours, which is until 18:00 of 6 October 1996; finally, heat fluxes were turned back on until the end of the simulation. From this point on, we will refer to this test as 'II No Fluxes' test.

In contrast with what we did in the previous test, we will not examine the differences in the sea level pressure field and 500 hPa geopotential field between the control run and sensitivity test at the final time of the period when heat fluxes are switched off, as we did in figure 5.9. In fact, the absence of heat fluxes in the initial stage of cyclone formation (between 18 UTC 5 October and 18 UTC 6 October) dramatically changes the sea level pressure field and 500 hPa geopotential field. Anyway, with this test we want to analyze the effect of the surface heat fluxes in the immediately preceding and concurrent hours of the cyclone formation and not the effects of different environmental conditions in the cyclone development.

In figures 5.13a,b are shown the IWV, and the water vapor mixing ratio at 1000 hPa in figures 5.13c,d; figures on the left are referred to control run, and to II No Fluxes test on the right. Figures 5.13b and d are referred to the times when the fluxes were turned on in the

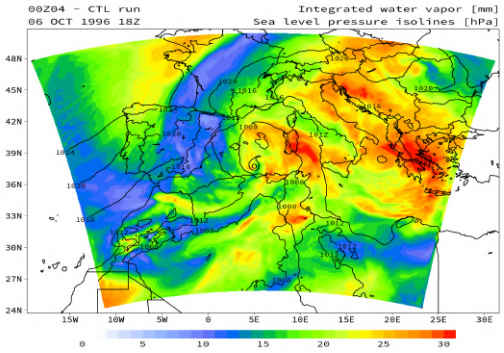

(a) 6 October 1996 - 18:00 UTC

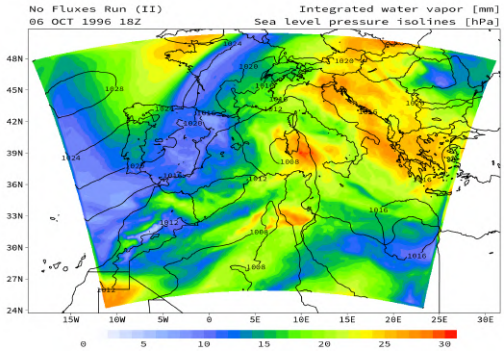

(b) 6 October 1996 - 18:00 UTC

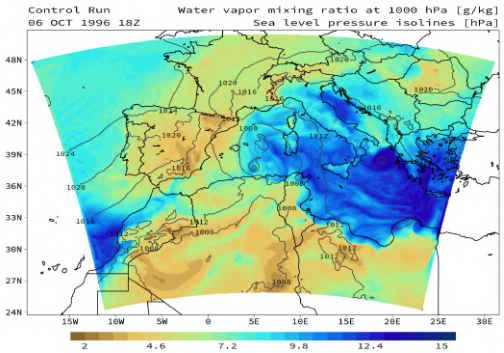

(c) 6 October 1996 - 18:00 UTC

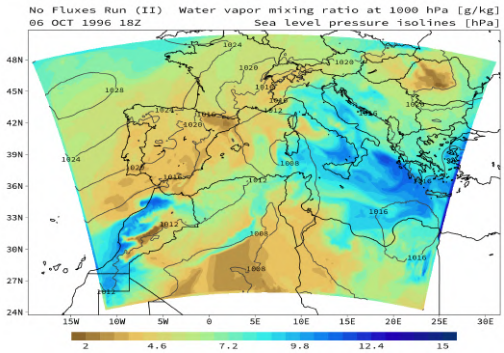

(d) 6 October 1996 - 18:00 UTC

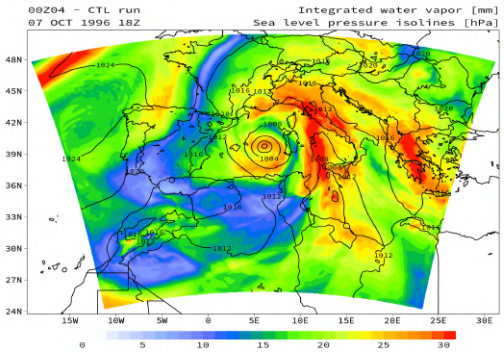

(e) 7 October 1996 - 18:00 UTC

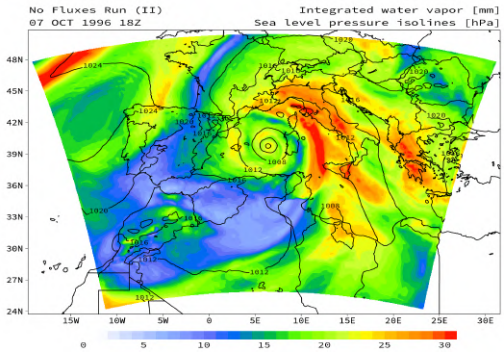

(f) 7 October 1996 - 18:00 UTC

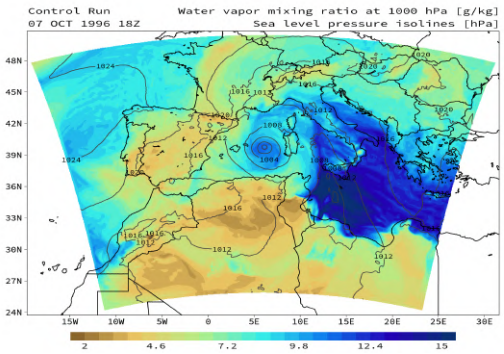

(g) 7 October 1996 - 18:00 UTC

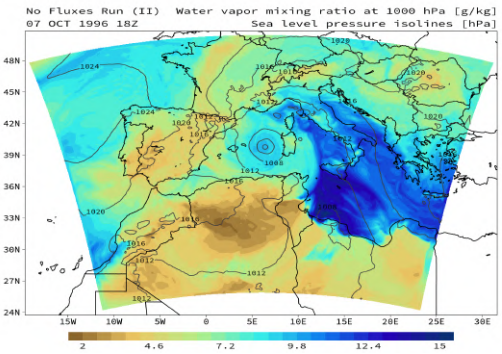

(h) 7 October 1996 - 18:00 UTC

Figure 5.13: Integrated water vapor and water vapor mixing ratio at 1000 hPa in the control run and II No Fluxes test

sensitivity experiments. When the heat fluxes are turned back on, the IWV nearly maintains the same structure but with significant differences in maximum values, especially over Greece and over Sardinia (figures 5.13a,b). Major differences can be noted in the water vapor mixing ratio fields at 1000 hPa (Figures 5.13c,d): in the control run the cyclone starts to form off the Algeria coast, while in the sensitivity test it does not intensify, both in water vapor and sea level pressure terms. After 24 hours, at 18:00 UTC of 7 October 1996, differences in IWV and water vapor mixing ratio at 1000 hPa reduce (figures 5.13e,f and 5.13g,h, respectively). Both structure are qualitatively similar and the cyclone in the sensitivity test reduces the humidity gap with respect to the control run cyclone. The structure of sea level pressure is almost identical (figure 5.14), with differences apparently only in the values: hence, the sea level pressure minimum at 18:00 UTC of 7 October is higher than the control run minimum.

Figure 5.15 shows the sea level pressure minimum time evolution of the control run and the sensitivity test, and the latent heat maximum time evolution only for the control run. Values of sea level pressure and latent heat fluxes are calculated in the same domain as figures 5.13. In the period when the heat fluxes were turned off (dotted green line of figure 5.15), there is not minimum's intensification. At the time when the heat fluxes have been turned on back (solid green line), the sea level pressure minimum of the sensitivity test is much higher than the control run; nevertheless, the sensitivity test cyclone suddenly intensifies at the same rate as the control run cyclone did earlier. After this intensification (until 03:00 UTC of 7 October), the pressure minimum in the sensitivity test remains nearly constant, following a similar evolution as the control run. One should note that the cyclone in the sensitivity test is able to recover only partially the intensity of the cyclone in the control run, which indicates that the duration of the period when the cyclone interacts with the outflow of tramontane and cierzo is relevant for the total intensification of the cyclone. In fact, the latent-heat fluxes time evolution (long-dash blue line) indicates that the intensification of the control run cyclone begins when fluxes intensify. It may be concluded that, in contrast to the Medicane Zeo case, where the heat fluxes play a significant role in the preconditional phase, in the Medicane Cornelia case the heat fluxes induced by the outbreak of wind (figure 5.7b) interacts with the cyclone itself for its development and further intensification. This is a clear indication of the importance of the WISHE mechanism in the development and maintenance of this cyclone (Miglietta and Rotunno, 2019 [42]).

5.4 Dry air masses analysis

Now we move to the analysis of the behavior and impact of upper level dry air masses in the formation of the cyclone, using again the back-trajectory analysis. Figure 5.16, referred to the initial phase of the cyclone, shows water vapor mixing ratio at 500 hPa, on the left side, and back-trajectories, that start from 500 hPa, on the right side; elevation field is superimposed

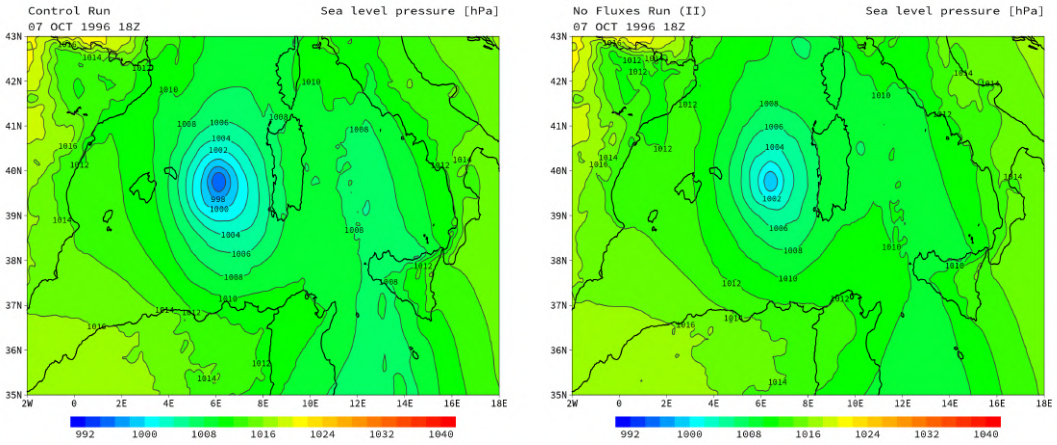

(a) 17 October 1996 - 18:00 UTC (b) 7 October 1996 - 18:00 UTC

Figure 5.14 – Sea level pressure isolines in the control run and II No Fluxes test

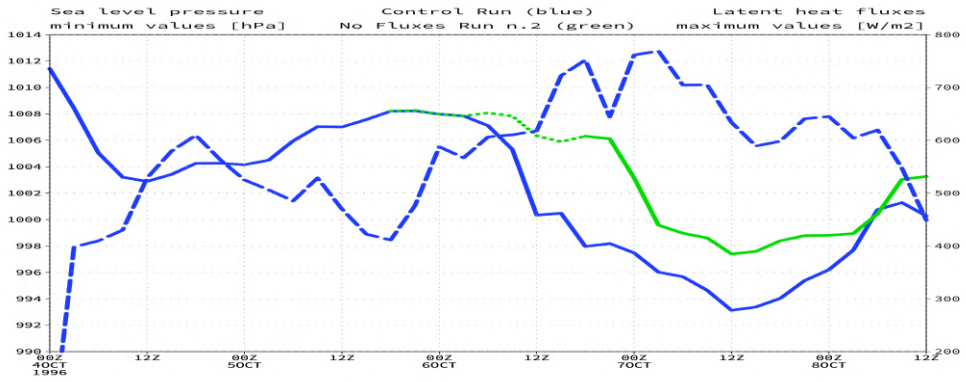

Figure 5.15: Sea level pressure minimum value (every 3 hours) in the control run (solid blue line) and in II No Fluxes test (dotted+solid green line) and latent heat fluxes maximum values in the control run only (long dash line). Dotted green part refers to the sensitivity test when the heat fluxes have been turned off.

on back-trajectories in figure 5.16b. At higher troposphere levels, two dry contributions appear (figure 5.16a): one, the northernmost, comes from North and almost moves above to the sea level pressure minimum; second, the southernmost, comes from West/Northwest from the Atlantic. According to elevation on the back-trajectory image (figure 5.16b), trajectories from the north are likely connected to the dry-air intrusion, coming from 6000-6500 m; in contrast, the southernmost comes mainly from the west, but does not affect directly the cyclone development. To better identify the dry-air intrusion of the PV streamer moving northward, figures 5.16c,d show RH in two cross sections, each centered at the latitude of the respective sea level pressure minimum. The upper-level dry intrusion appears limited and confined to the boundaries of the circulation. Back-trajectory analysis does not show dry air coming from lower tropospheric levels towards the future cyclogenic area.

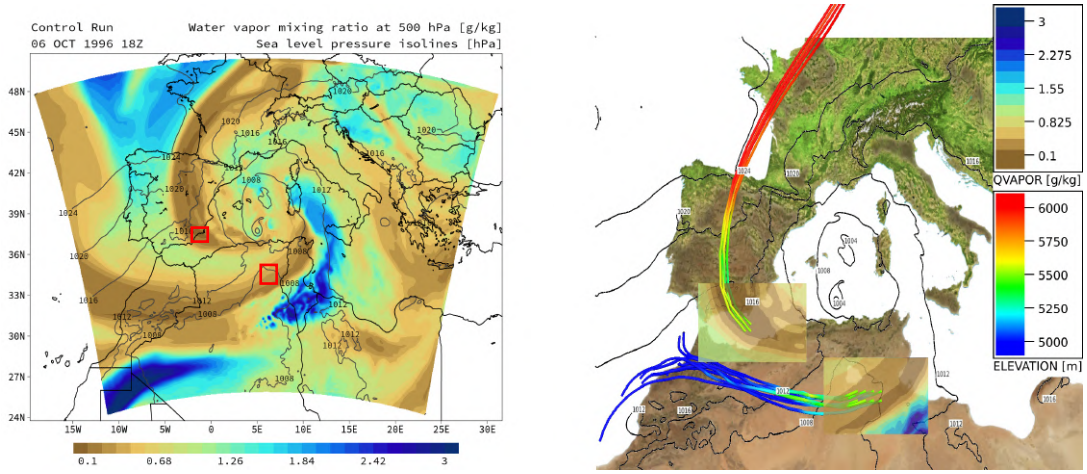

(a) 6 October 1996 - 18:00 UTC

(b) Back-trajectories of 48h from 3000 m

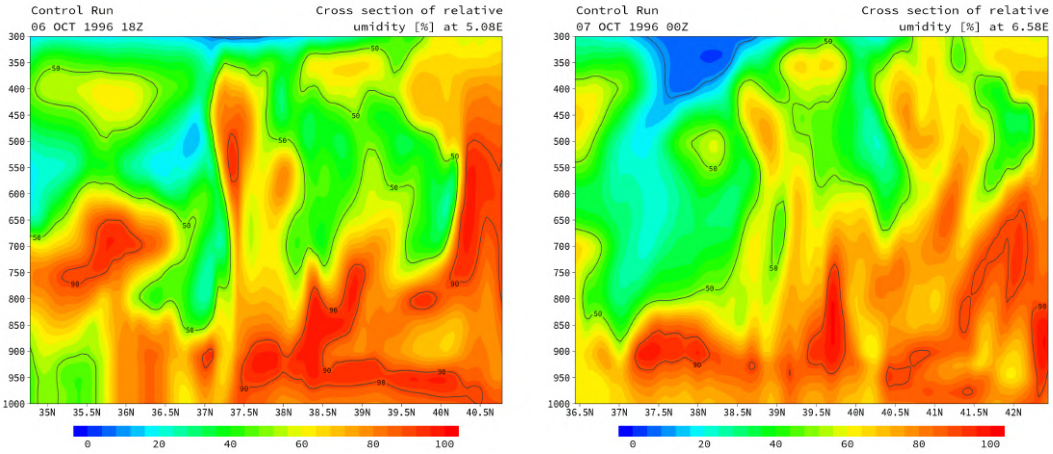

(c) 6 October 1996 - 18:00 UTC (center at 37.78° N)

(d) 7 October 1996 - 00:00 UTC (center at 39.44° N)

Figure 5.16 – Dry air back-trajectory analysis at 500 hPa

5.5 Sensitivity tests with addition of water vapor

Following the same procedure used in the Medicane Zeo case, we illustrate the results of new simulations where the initial conditions were modified so that the minimum values of RH are 50%. Four RH50 tests were performed and for every test a control run was done, which is a run where the initial conditions were not modified: the first, to which we will refer as '00Z04-RH50' test, starts at 00:00 UTC of 4 October 1996; the second, to which we will refer as '12Z04-RH50' test, starts at 12:00 UTC of 4 October 1996; the third, the '00Z105-RH50' test, starts at 00:00 UTC of 5 October 1996; the fourth, the '12Z05-RH50' test, starts at 12:00 UTC of 5 October 1996. Control runs will be named as 00Z04-CTL, '12Z04-CTL', '00Z05-CTL' and '12Z05-CTL', respectively.

5.5.1 Results of RH50 sensitivity tests

In contrast to the way we proceeded in Medicane Zeo RH50 sensitivity tests, in this case the results of this analysis will be exposed in two parts. One concerns the runs of 4 October (i.e., 00Z04-CTL, 00Z04-RH50, 12Z04-CTL and 12Z04-RH50) and the other the runs of 5 October (i.e., 00Z05-CTL, 00Z05-RH50, 12Z05-CTL and 12Z05-RH50). In the two control runs starting on 4 October, the comparison with the sensitivity tests comes out to be meaningless. One reason is due to the rather different regions of development: figure 5.17 shows, in the first row, total surface heat fluxes with sea level pressure isolines and wind field at 1000 hPa for 00Z04-CTL and 00Z04-RH50 and, in the second row, cyclone simulated trajectories for both runs; in the third and fourth row there are the same plots but referred to runs 12Z04-CTL and 12Z04-RH50. In 00Z04 cases, figures 5.17a,b, the control run cyclone develops between Sardinia and the Balearic Islands, consistently with satellite images (see figure 5.1a), while the RH50 cyclone forms northernmost. Despite the 12Z04-RH50 cyclone forms closer to the total surface heat fluxes peak region, it does not intensify in term of sea level pressure minimum (see the sea level pressure minimum time evolution on figure 5.18). The reason of this lack may be found observing the 00Z04-RH50 cyclone trajectory (figure 5.17d): in fact, the cyclone remains for a shorter period in the region where the fluxes are more intense, compared to what happened in the 00Z04-CTL cyclone, 5.17c. In addition, the limited predictability of this cyclone (see the differences in the control runs starting at different times in figure 5.17) and/or the complex morphology of the western Mediterranean region (confined among different islands, thus with a high probability of landfall, as it is for this case) can significantly affect the behavior of cyclones as they are significantly different already in the initial stages. Another important reason that explains the lack of intensification in the 00Z04-RH50 test is that this simulation starts much earlier with respect to the time when the cyclone developed, and, for the reasons provided in section 4.5, the constraint on RH is not effective in reducing the humidity content near the cyclone center. Analogous considerations can be adduced for the 12Z04 case (see figures 5.17b,f). Comparing the simulated trajectories of the 12Z04 cases (figures 5.17g,h), the 12Z04-RH50 tests seems to be affected by the same issues of the 00Z04-RH50, i.e., different development region that cause different formation and start of the simulation too early with respect to cyclone formation; the sea level pressure time evolution in figure 5.18 does not show a significant intensification for the 12Z04-RH50 cyclone. Thus, such differences make the comparison meaningless. Hereafter, we will focus only on the latter two couple of runs.

Figure 5.20 shows, in the first row, the total surface heat fluxes with sea level pressure isolines and wind field at 1000 hPa for 00Z05-CTL and 00Z05-RH50 and, in the second row, cyclone simulated trajectories for both runs; in the third and fourth row there are the same plots but referred to runs 12Z05-CTL and 12Z05-RH50. The trajectories (figures 5.20c,d) are more similar between them with respect to the trajectories of the earlier runs (figure 5.20). In

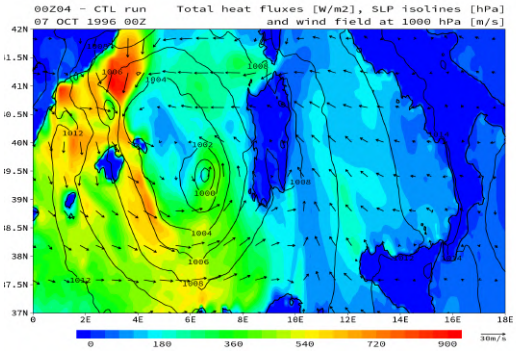

(a) 00Z04 - CTL run

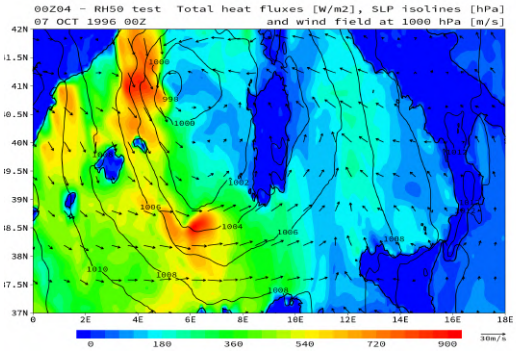

(b) 00Z04 - RH50 test

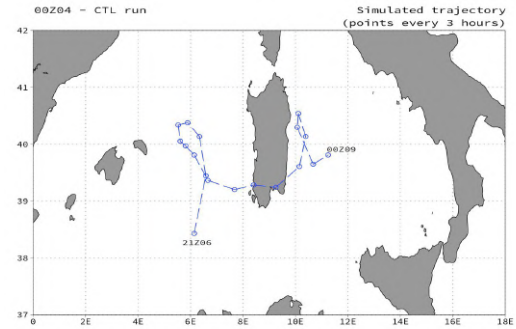

(c) 00Z04 - CTL run

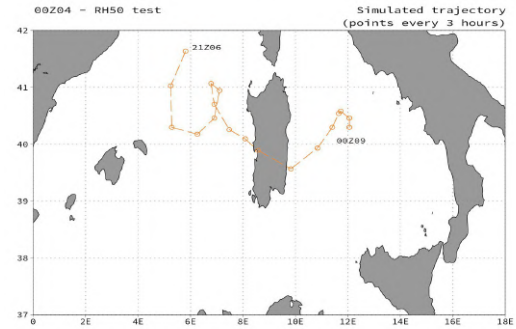

(d) 00Z04 - RH50 test

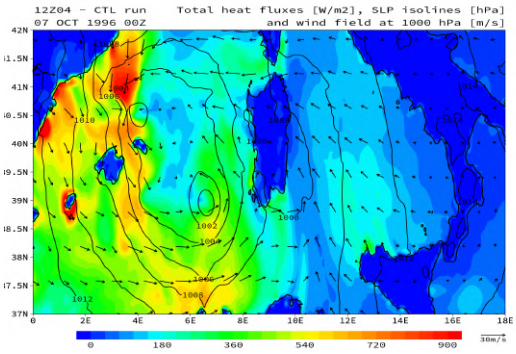

(e) 12Z04 - CTL run

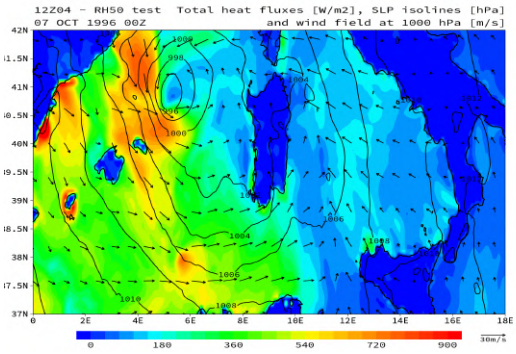

(f) 12Z04 - RH50 test

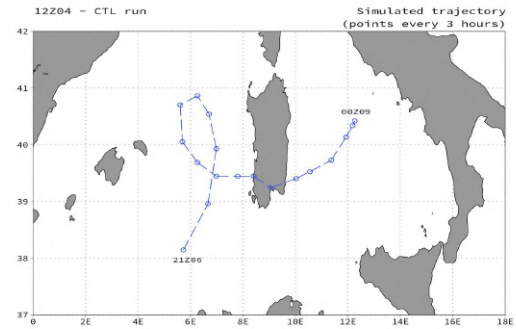

(g) 12Z04 - CTL run

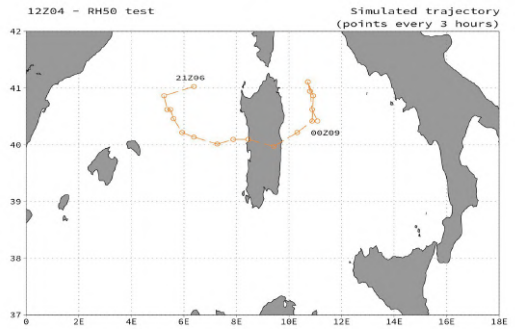

(h) 12Z04 - RH50 test

Figure 5.17: Total suface heat fluxes with sea level pressure isolines and wind field at 1000 hPa in the control runs and RH50 tests of 4 October and cyclone simulated trajectories.

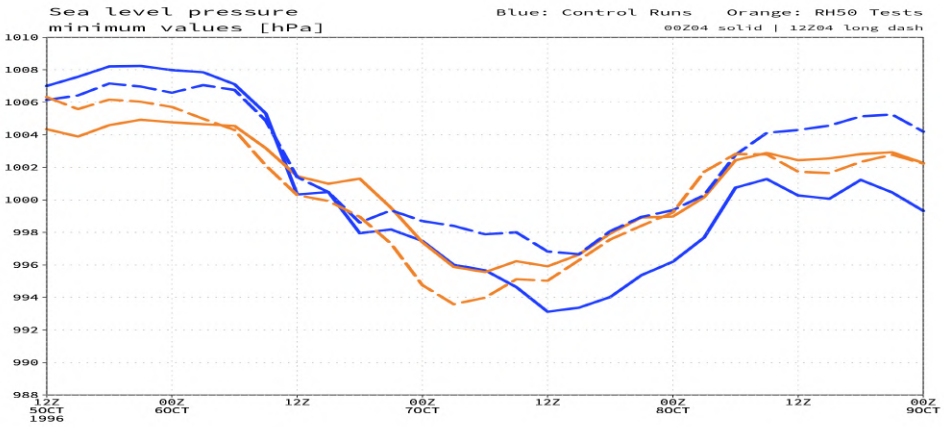

Figure 5.18 – Sea level pressure minimum values (every 3 hours) in the control runs and in RH50 tests

00Z05 runs, control run and RH50 sensitivity cyclones nearly form in the same area, between 40° - 41° N and 6° E, as it can be viewed with the aid of the sea level pressure isolines in figures 5.20a,b. In 12Z05 runs, the cyclones develop northeast of Menorca island. Thus, similar regions of development with nearly equal sea level pressure minimum in the initial stage (see figure 5.19 from 12:00 UTC of 5 October until 00:00 UTC of 6 October) make it possible a comparison. Figure 5.17 depicts, for the 00Z05-CTL run, a wide Low structure with relatively high sea level pressure value of 1002 hPa at the center. Instead, for the 00Z05-RH50 test, the sea level pressure structure appears more developed with higher wind velocity around the minimum of about 998 hPa. Observing dot-dot-dashed lines in figure 5.19, we note that the intensification of the 00Z05-RH50 cyclone, with respect to the counterpart 00Z05-CTL cyclone, spans all over the life time of the sensitivity cyclone; the sea level pressure time evolution of the 00Z05-RH50 cyclone is really similar to the 00Z05-CTL counterpart but shifted to lower pressure values. For runs that start at 12:00 UTC of 5 October, the intensification of the RH50 tests is more evident. Figures 5.19g,h show trajectories surprisingly similar. Inspection of figures 5.19e,f shows,

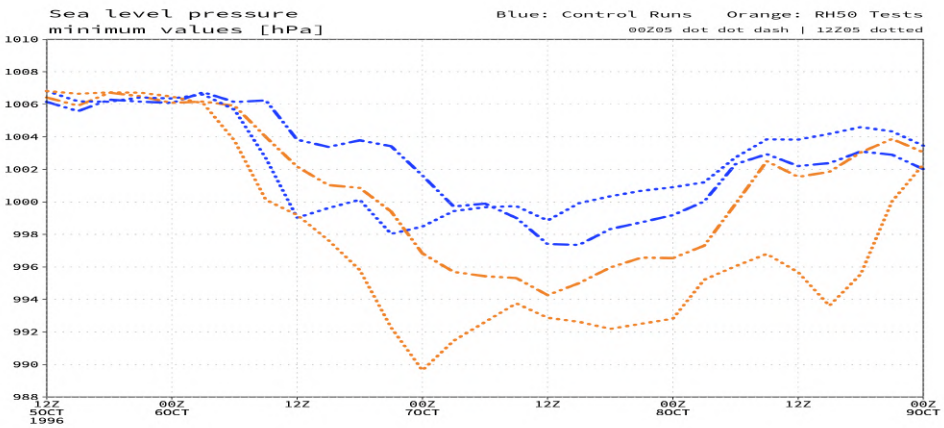

Figure 5.19 – Sea level pressure minimum values (every 3 hours) in the control runs and in RH50 tests

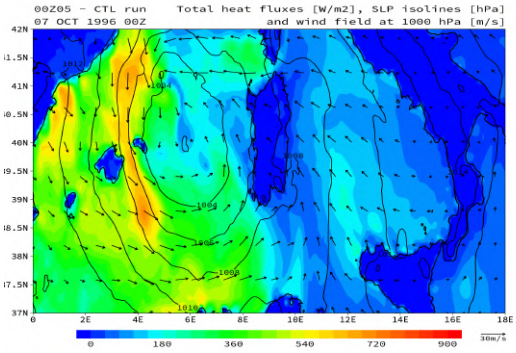

(a) 00Z05 - CTL run

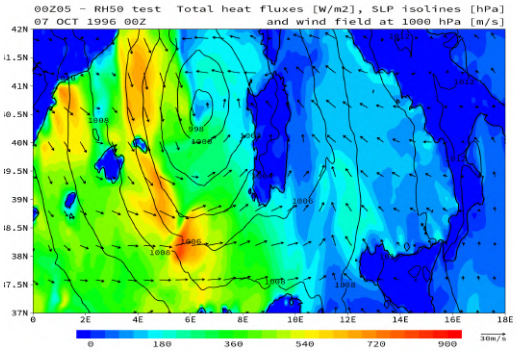

(b) 00Z05 - RH50 test

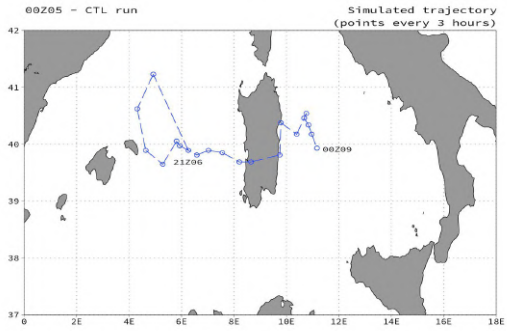

(c) 00Z05 - CTL run

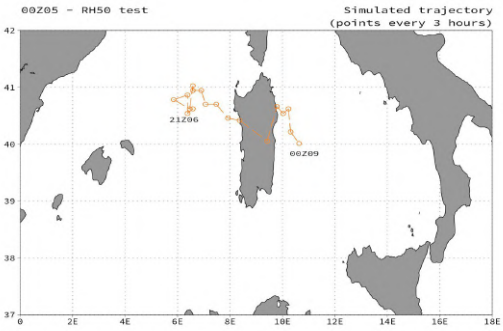

(d) 00Z05 - RH50 test

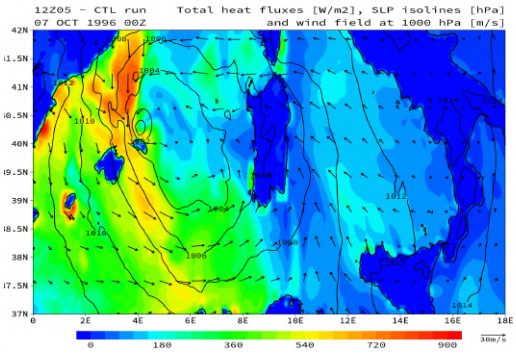

(e) 12Z05 - CTL run

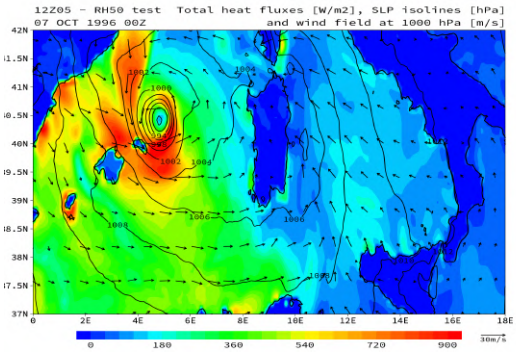

(f) 12Z05 - RH50 test

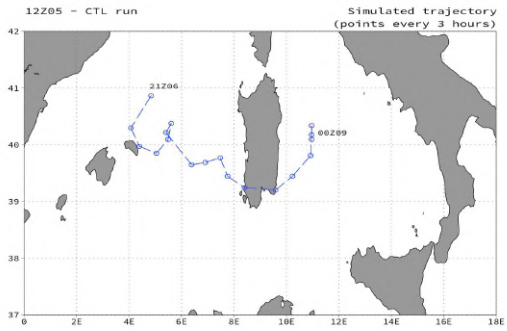

(g) 12Z05 - CTL run

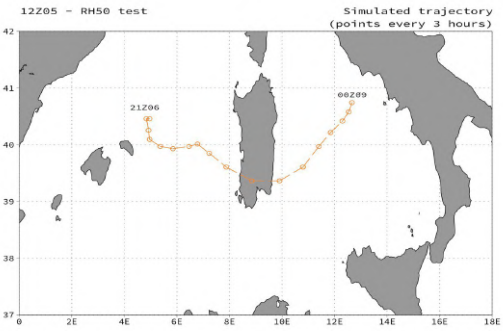

(h) 12Z05 - RH50 test

Figure 5.20: Total suface heat fluxes with sea level pressure isolines and wind field at 1000 hPa in the control runs and RH50 tests of 5 October and cyclone simulated trajectories.

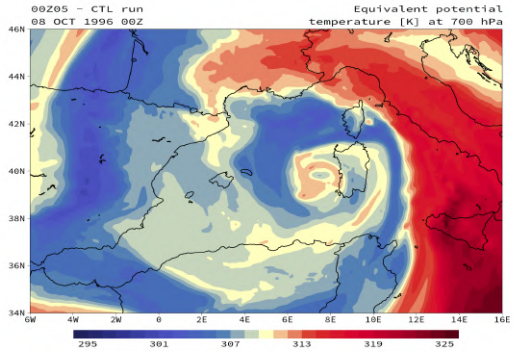

(a) 00Z05 - CTL run

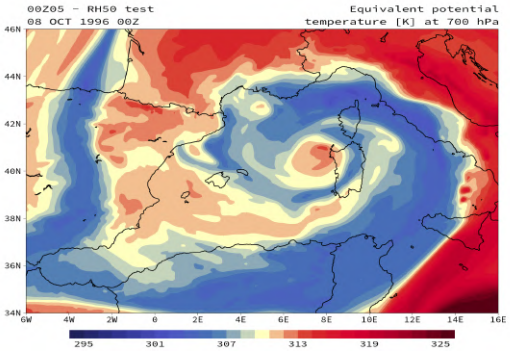

(b) 00Z05 - RH50 test

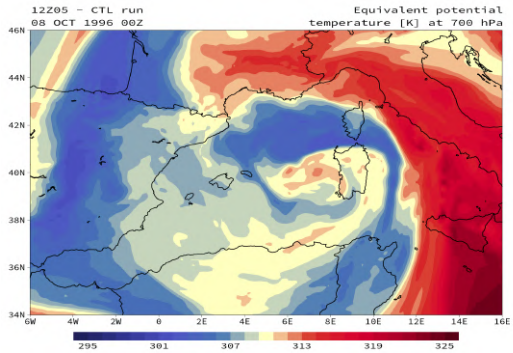

(c) 12Z05 - CTL run

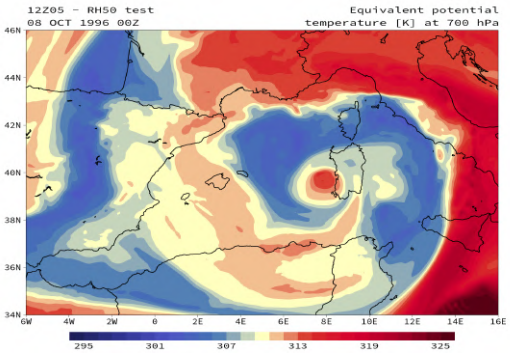

(d) 12Z05 - RH50 test

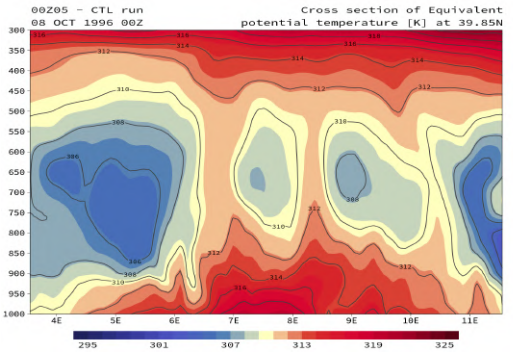

(e) 00Z05 - CTL run (center at 7.55° E)

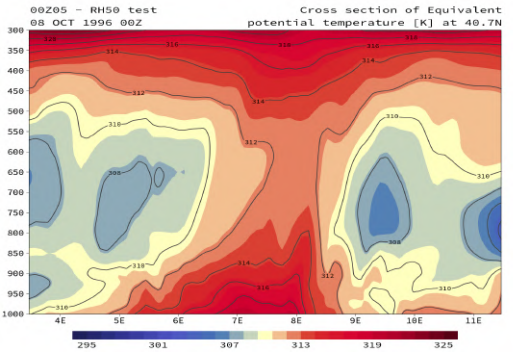

(f) 00Z05 - RH50 test (center at 7.47° E)

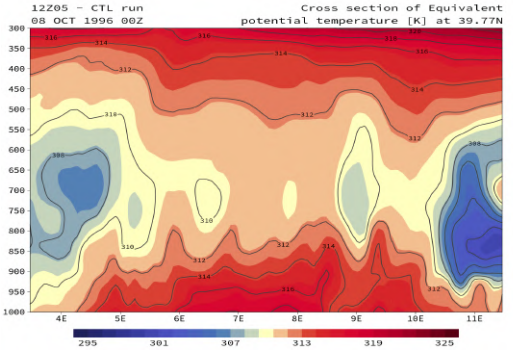

(g) 12Z05 - CTL run (center at 7.47° E)

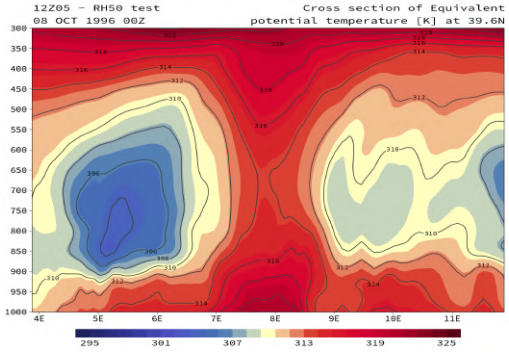

(h) 12Z05 - RH50 test (center at 7.88° E)

Figure 5.21 – θ_e fields at 700 hPa and cross sections of control runs and RH50 tests

instead, deep differences in the sea level pressure structures, wind field and heat surface fluxes behavior. The sea level pressure minimum of the 12Z05-RH50 test at 00:00 of 7 October reaches 990 hPa with high values of wind field around the minimum (nearly greater than 30 m/s), while, in the 12Z05-CTL cyclone, the sea level pressure minimum is about 1000 hPa with values of wind field around the minimum that not exceed 20 m/s.

To get a better insight about the detrimental role of dry air intrusion in the center of the cyclone we inspect the vertical structure inside and at the borders of the cyclones center. Figure 5.21 shows, in the first two rows, 700 hPa θ_e fields at 00:00 UTC of 8 October 1996 for 00Z05-CTL and 12Z05-CTL runs in the first column, and for 00Z05-RH50 and 12Z05-RH50 runs tests in the second column; each rows refers to a specific test. Between each control runs and the counterpart RH50 test, the delay in the development is apparent. While all control runs show really similar θ_e structure, with cold and dry air even near the center of the cyclonic circulation (case 00Z05-CTL and 12Z05-CTL in figures 5.21a and c respectively), RH50 tests present more advanced formation phase, with a more isolated warm core, especially in the last test (figure 5.21d). To better appreciate this behavior, figure 5.21 shows also θ_e vertical cross sections of the cyclones, that follows the same representation scheme of the figure 5.20 (the center of the cyclones is identified by the minimum value of sea level pressure and its longitude is specified in the relative caption). The RH50 cyclones (figure 5.21,f,h) show progressively an advanced columnar structure with more defined warm-core, really similar to TCs. Instead, control run cyclones (figure 5.21e,g) reveal nearly the same less defined θ_e vertical structure with evident cold and dry air spots, indication of dry intrusions still active, as discussed in Miglietta and Rotunno, 2019 [42].

We want to notice that, with respect the Medicane Zeo case, the interpretation of these sensitivity tests is more complicated, partly due to the great sensitivity to the initial conditions, but mainly due to the landfall that occurs earlier in the RH50 test, making less easy the comparison of the two runs.

III Final considerations and conceptual model

6 | Conclusions

The thesis focused on the transport and interactions of moist and dry air masses within the Mediterranean basin that led to the development of two Medicanes. The study adopted a modeling approach, using the WRF-ARW model, version 4.1, initialized with ERA5 of ECMWF. While most studies on Medicane development use high-resolution numerical simulations to explicitly resolve convection at system scale and represent the detailed evolution of the cyclones, the aim of the present numerical simulations was somewhat different. To analyze the synoptic- and meso-scale conditions on the day immediately before the cyclone formations and in the early stage of its lifetime, we chose two single domains (one for each simulation) with a relatively coarse grid spacing (9km), but sufficient to resolve these features, and domains large enough to include the long-range transport of moist/dry air toward the cyclone center.

After the control runs, the analysis of the outputs was conducted using GrADS and VAPOR, two main graphical tools used to represent the meteorological fields in 2D and 3D, respectively. First of all, several horizontal and vertical sections of the atmosphere were performed with GrADS to get an overview of the state of the atmosphere before the formation of the cyclones. Once identified the main source of moist air and the strongest upper-level streamers of dry intrusions near the center of the cyclones, we moved on to the back-trajectory analysis. The large number of options of the VAPOR software allowed us to clearly identify the origin of moist and dry air masses in the preconditional and initial phases of development of both cyclones.

Two types of sensitivity tests were then performed to investigate the influence of such air masses in the cyclones formation. The former concerned the role of sea surface heat fluxes to increase the water vapor content in the low-levels of the atmosphere in the regions where the cyclones would have formed, and the latter examined the role of the upper-level dry intrusion in the initial phases. In the following, a brief summary of the procedure and the results of the tests will be illustrated.

Concerning the 'No Fluxes tests', once identified the critical moments of the control runs when sea surface heat fluxes increased their intensity, the latent and sensible heat fluxes were turned off, throughout the domain, in the period of maximum intensity and turned on again after several hours. For the Medicane Zeo case study, it was found that without the intense sea surface fluxes in the southern Mediterranean in the preconditional phase, the cyclone in the

sensitivity test cannot reach the same intensity of the control run cyclone, with a maximum difference of sea level pressure of 10 hPa when the control run cyclone is most intense. We conclude, in this case, that heat fluxes from the sea surface are essential to create a favorable humid environment to the formation of the cyclone. For the Medicane Cornelia, two different tests were carried out to explore the role of the surface heat fluxes. In the first test, the latent and sensible heat fluxes were turned off at the start of the simulation until the beginning of the intensification of the heat fluxes near the Balearic Islands. Results showed that the effect of heat fluxes in the preconditional phase plays a minor role in the cyclone formation and further intensification. Thus, a second sensitivity test was considered to analyze the role of the heat fluxes in the initial phase of the Medicane Cornelia development. This latter test showed that the heat fluxes in the initial phase of the cyclone, induced by the outbreak of northerly regional winds, interacted with the cyclone itself and determined its intensification. This last case confirms the importance of the WISHE mechanisms in the development and maintenance of the cyclone.

Regarding the detrimental role of the upper-level dry intrusions in the initial and mature stage of the cyclone life-time, new simulations (called here 'RH50 tests') with modified initial and boundary conditions were undertaken. To reduce the impact of the dry intrusions, we modified the original initial and boundary conditions with the constraint that the values of RH smaller than 50% had to be set to 50%. This threshold value was chosen as a compromise between making the atmosphere more humid but not as much as to induce local saturation and cause the release of latent heat, which could change the evolution of the cyclone dramatically. Moreover, we verified that the change in RH does not change the PV structure and values, which means that the interaction of the PV streamers with the forming cyclone is not significantly modified, while only the change in humidity is relevant. Due to the limitations of the present approach (explained in detail in section 4.5), we decided to use a time-lagged approach to analyze a set of different simulations. With respect to the previous sensitivity test, where we found different conclusions likely due to different types of formations of the two cyclones, these further tests point to the same conclusion. Analyzing different types of meteorological variables, as the sea level pressure and its time evolution, sections of equivalent potential temperature and IWV plots, we concluded that an increase of humidity content in the whole atmosphere in the preconditioning phase of cyclones formation allows for a faster development, a more defined vertical structure and a slightly wider horizontal extension. Because of the importance of this novel result for Mediterranean tropical-like cyclones, it's worth to say a few words on the subject.

To get an over view of the cyclone life-cycles, we can see their Hart's diagrams, computed as proposed by Picornell et al., 2014 [51] for mesoscale cyclones as Medicanes. We have chosen to show here only the RH50 sensitivity cases (and related control runs) that better explain the results of these tests. In the first row of figure 6.1 the Hart diagrams of the 00Z12-CTL run

are shown and, in the second row, the Hart's diagrams of the 00Z12-RH50 test; B, $-V_T^L$ and $-V_T^U$ values are averaged over a circle with a radius of 100 km. These diagrams, that refer to tests relative to the Medicane Zeo case, clearly reveal that a more humid atmosphere generates cyclones that are more intense and more similar to TCs. In fact, in figures 6.1a,b we note that the control run cyclone reaches the structure of a symmetric, but moderate, warm core cyclone during the period of its maximum intensity, but it nearly looses these features during the last moments of its life-cycle. Instead, the 00Z12-RH50 cyclone (figures 6.1c,d) rapidly becomes a non-frontal system with a deep warm-core (see high values of $-V_T^U$ reached in figure 6.1d) and remains, for the most of its simulated life-time, a symmetric and deep-warm core cyclone.

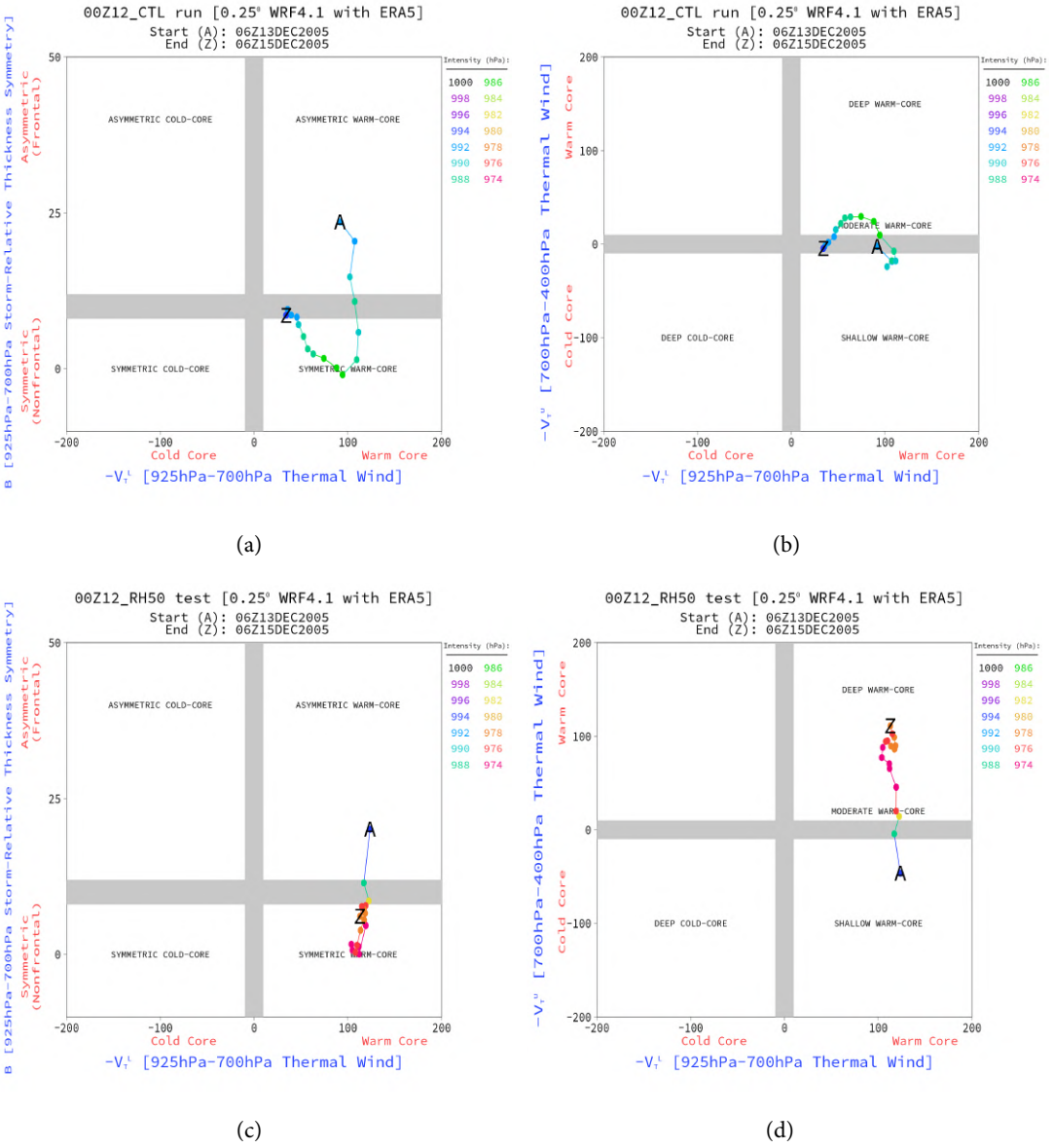

Figure 6.1: Hart's diagrams of the 00Z12-CTL run and 00Z12-RH50 test cyclones. Colors are referred to the intensity of the sea level pressure. One point every 3 hours.

With respect to Hart diagrams relative to the Medicane Cornelia, figure 6.2 shows, in the first row, the Hart's diagrams of the 12Z05-CTL run and, in the second row, the Hart's diagrams of the 12Z05-RH50 test; B, $-V_T^L$ and $-V_T^U$ values are averaged over a circle with a radius of 100 km. A comparison between figures 6.2a,c and figures 6.2b,d leads to the same conclusions previously exposed, i.e. the cyclone is symmetric in both runs but only in the sensitivity test it reaches persistently the upper troposphere.

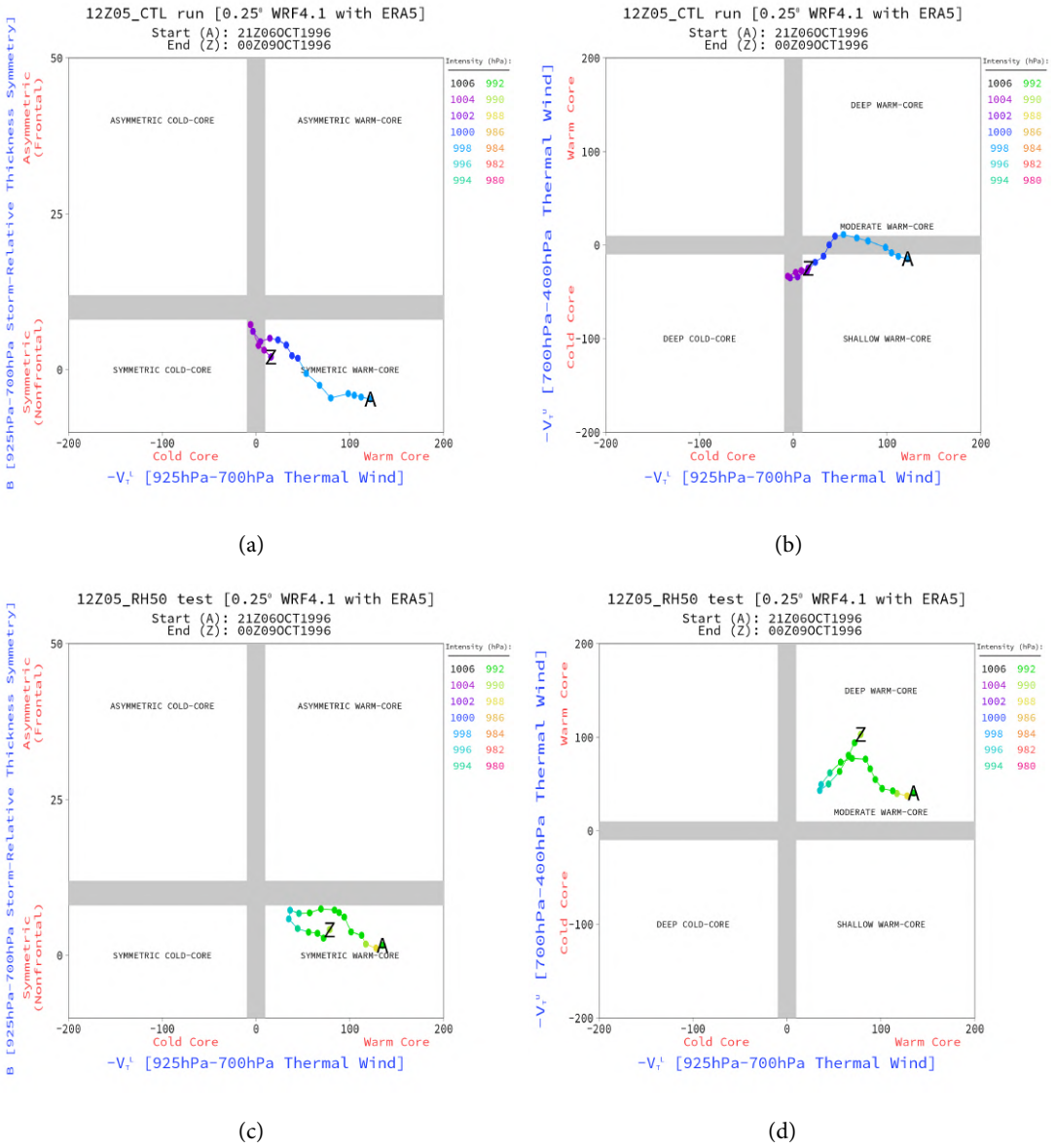

Figure 6.2: Hart's diagrams of the 12Z05-CTL run and 12Z05-RH50 test cyclones. Colors are referred to the intensity of the sea level pressure. One point every 3 hours.

An attempt to qualitatively explain how and why these types of cyclones intensify in the presence of a more humid atmosphere was performed. Figure 6.3 shows schematically the result of part of this work. The first row of figure 6.3 indicates a generic control run, as we have

referred to until now, i.e., a run where initial and boundary conditions have not been modified, and the second row refers to a RH50 test. What we have noticed is that upper-level streamers of dry air wrap around the embrional warm column (figure 6.3a) in the initial stage of the cyclone development, standing at the top of the column at the mature stage; this causes more mixing of the moist air with the dry air and weakens the development of convection near the center, intensifying the downdraft, which is known to be detrimental to the development of tropical cyclones. If in the initial phase, the intrusion of dry air were less intense, the embrional warm column could form and intensify earlier in a more favorable environment. Thus, the warm column could develop until the top of the troposphere (as TCs do), leaving the dry air at the boundary around it (figure 6.3d).

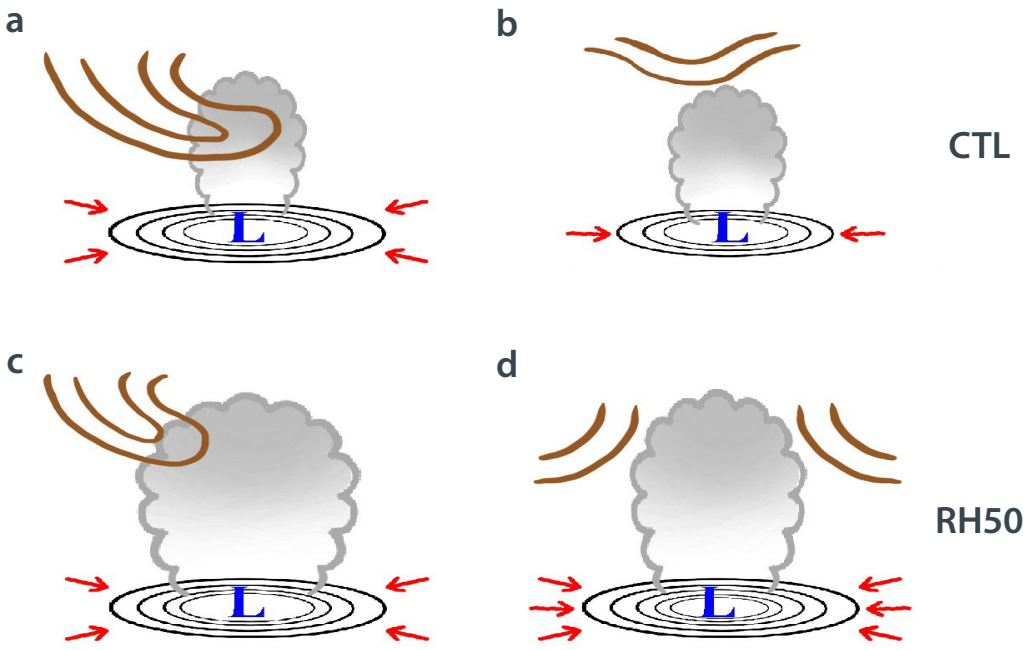

Figure 6.3: Conceptual model of the detrimental role of upper-level dry intrusions in the Mediterranean tropical like-cyclone formation

With regard to future developments of research in this area, strongly believe that additional Medicane case studies have to be analyzed. A larger amount of cases could show more clearly geographical and dynamics analogies, or differences, with the Medicanes analyzed here. In fact, due to the complex geography of the area where they form and the high number of factors that compete in their development, Mediterranean tropical like-cyclones remain an open research field. Moreover, a realistic numerical simulation of this type of cyclones remains a challenge for NWP models. It is therefore desirable to encourage further improvements in the field of numerical simulations, in the coupled use of different types of models (i.e., atmospheric, oceanographic and chemical models), in the types of parameterizations used and in the quality of input data. For what strictly concerns the results of this work, while the key role

of heat surface fluxes from the sea in the Medicanes formation finds a broad agreement in the literature, the quantitative role of dry intrusions appears stil to be unexplored. A better understanding of the main factors that compete in the dynamics of this types of cyclones will lead to a higher forecast efficiency.

Bibliography

1. Bjerknes, J., 1919: On the structure of moving cyclones. *Monthly Weather Review*, **47 (2)**, 95–99, https://doi.org/10.1175/1520-0493(1919)47<95:OTSOMC>2.0.CO;2.

2. Bjerknes, J., and H. Solberg, 1922: On the life cycle of cyclone and the polar front theory of atmospheric circulation. *Monthly Weather Review*, **50 (9)**, 468–473, https://doi.org/10.1175/1520-0493(1922)50<468:JBAHSO>2.0.CO;2.

3. Bjerknes, V., 2009: The problem of weather prediction, considered from the viewpoints of mechanics and physics. *Meteorologische Zeitschrift*, **18 (6)**, 663–667, https://doi.org/10.1127/0941-2948/2009/416.

4. Businger, S., and R. J. Reed, 1989: Cyclogenesis in cold air masses. *Weather and Forecasting*, **4 (2)**, 133–156, https://doi.org/10.1175/1520-0434(1989)004<0133:CICAM>2.0.CO;2.

5. Buzzi, A., and S. Tibaldi, 1978: Cyclogenesis in the lee of the alps: A case study. *Quarterly Journal of the Royal Meteorological Society*, **104 (440)**, 271–287, https://doi.org/10.1002/qj.49710444004.

6. Cadet, D., 1983: Tropical cyclones: Their evolution, structure, and effects. *Eos, Transactions American Geophysical Union*, **64 (4)**, 25–26, doi:\url{https://doi.org/10.1029/EO064i004p00025-04}.

7. Cassardo, C., 2015: Spaghetti plot. https://claudiocassardo.wordpress.com/tag/spaghetti-plot/.

8. Cavicchia, L., H. Von Storch, and S. Gualdi, 2013: A long-term climatology of medicanes. *Climate Dynamics*, **43**, https://doi.org/10.1007/s00382-013-1893-7.

9. Centre, H. Z. G., 2020: Data assimilation scheme. https://www.schulprojekt-klimawandel.de/institutes_platforms/coastal_research/system_analysis/data_analysis_assimilation/topics/data_assimilation/.

10. Chaboureau, J.-P., F. Pantillon, D. Lambert, E. Richard, and C. Claud, 2012: Tropical transition of a mediterranean storm by jet crossing. *Quarterly Journal of the Royal Meteorological Society*, **138 (664)**, 596–611, https://doi.org/10.1002/qj.960.

11. Charney, J. G., and A. Eliassen, 1964: On the growth of the hurricane depression. *Journal of the Atmospheric Sciences*, **21**, 68–75, https://doi.org/10.1175/1520-0469(1964)021<0068:OTGOTH>2.0.CO;2.

12. Dafis, S., J.-F. Rysman, C. Claud, and E. Flaounas, 2018: Remote sensing of deep convection within a tropical-like cyclone over the mediterranean sea. *Atmospheric Science Letters*, **19 (6)**, e823, https://doi.org/10.1002/asl.823.

13. Davolio, S., M. Miglietta, A. Moscatello, F. Pacifico, A. Buzzi, and R. Rotunno, 2009: Numerical forecast and analysis of a tropical-like cyclone in the ionian sea. *Natural Hazards and Earth System Sciences*, **9**, 551–562, https://doi.org/10.5194/nhess-9-551-2009.

14. Di Muzio, E., M. Riemer, A. H. Fink, and M. Maier-Gerber, 2019: Assessing the predictability of medicanes in ecmwf ensemble forecasts using an object-based approach. *Quarterly Journal of the Royal Meteorological Society*, **145 (720)**, 1202–1217, https://doi.org/10.1002/qj.3489.

15. Dudhia, J., 1989: Numerical study of convection observed during the winter monsoon experiment using a mesoscale two-dimensional model. *Journal of the Atmospheric Sciences*, **46 (20)**, 3077–3107, https://doi.org/10.1175/1520-0469(1989)046<3077:NSOCOD>2.0.CO;2.

16. Dudhia, J., 1996: A multi-layer soil temperature model for mm5. *Preprints, The Sixth PSU/NCAR mesoscale model users' workshop*, 22–24.

17. ECMWF, 2019: Ecmwf website. https://www.ecmwf.int/.

18. ECMWF, 2019: Ensemble forecast. https://www.ecmwf.int/en/about/media-centre/news/2017/how-pin-down-uncertainty-weather-forecasting.

19. ECMWF, 2020: Climate data store. https://cds.climate.copernicus.eu/cdsapp#!/search?type=dataset.

20. Emanuel, K., 2005: Genesis and maintenance of "mediterranean hurricanes". *Advances in Geosciences*, **2**, 217–220, https://doi.org/10.5194/adgeo-2-217-2005.

21. Emanuel, K. A., 1986: An air-sea interaction theory for tropical cyclones. part i: Steady-state maintenance. *Journal of the Atmospheric Sciences*, **43**, 585–605, https://doi.org/10.1175/1520-0469(1986)043<0585:AASITF>2.0.CO;2.

22. Ernst, J. A., and M. Matson, 1983: A mediterranean tropical storm? *Weather*, **38 (11)**, 332–337, https://doi.org/10.1002/j.1477-8696.1983.tb04818.x.

23. Evans, J. L., and M. P. Guishard, 2009: Atlantic subtropical storms. part i: Diagnostic criteria and composite analysis. *Monthly Weather Review*, **137 (7)**, 2065–2080, https://doi.org/10.1175/2009MWR2468.1.

24. Explorer, N. V. G. D., 2015: Stc katie. https://www.nnvl.noaa.gov/view/globaldata.html#TRUE.

25. Explorer, N. V. G. D., 2019: Northeastern storm. http://www.nnvl.noaa.gov/view#TRUE?timespan=daily&date=2014-03-26&lat=36.915467625897&lon=-63.857203886384&zoom=4.

26. Fita, L., and E. Flaounas, 2018: Medicanes as subtropical cyclones: the december 2005 case from the perspective of surface pressure tendency diagnostics and atmospheric water budget. *Quarterly Journal of the Royal Meteorological Society*, **144 (713)**, 1028–1044, https://doi.org/10.1002/qj.3273.

27. Fita, L., R. Romero, A. Luque, K. Emanuel, and C. Ramis, 2007: Analysis of the environments of seven mediterranean tropical-like storms using an axisymmetric, nonhydrostatic, cloud resolving model. *Nat. Hazards Earth Syst. Sci*, **7**, https://doi.org/10.5194/nhess-7-41-2007.

28. Gaertner, M. A., D. Jacob, V. Gil, M. Domínguez, E. Padorno, E. Sánchez, and M. Castro, 2007: Tropical cyclones over the mediterranean sea in climate change simulations. *Geophysical Research Letters*, **34 (14)**, https://doi.org/10.1029/2007GL029977.

29. Hart, R. E., 2003: A cyclone phase space derived from thermal wind and thermal asymmetry. *Monthly Weather Review*, **131 (4)**, 585–616, https://doi.org/10.1175/1520-0493(2003)131<0585:ACPSDF>2.0.CO;2.

30. Holton, J., and G. Hakim, 2013: *An Introduction to Dynamic Meteorology*, International Geophysics Series, Vol. 88. 5th ed., Elsevier Science, https://doi.org/10.1016/C2009-0-63394-8.

31. Homar, V., R. Romero, D. J. Stensrud, C. Ramis, and S. Alonso, 2003: Numerical diagnosis of a small, quasi-tropical cyclone over the western mediterranean: Dynamical vs. boundary factors. *Quarterly Journal of the Royal Meteorological Society*, **129 (590)**, 1469–1490, https://doi.org/10.1256/qj.01.91.

32. Hong, S.-Y., J. Dudhia, and S.-H. Chen, 2004: A revised approach to ice microphysical processes for the bulk parameterization of clouds and precipitation. *Monthly Weather Review*, **132 (1)**, 103–120, https://doi.org/10.1175/1520-0493(2004)132<0103:ARATIM>2.0.CO;2.

33. Hong, S.-Y., Y. Noh, and J. Dudhia, 2006: A new vertical diffusion package with an explicit treatment of entrainment processes. *Monthly Weather Review*, **134 (9)**, 2318–2341, https://doi.org/10.1175/MWR3199.1.

34. Jiménez, P. A., J. Dudhia, J. F. González-Rouco, J. Navarro, J. P. Montávez, and E. García-Bustamante, 2012: A revised scheme for the wrf surface layer formulation. *Monthly Weather Review*, **140 (3)**, 898–918, https://doi.org/10.1175/MWR-D-11-00056.1.

35. Kain, J. S., 2004: The kain–fritsch convective parameterization: An update. *Journal of Applied Meteorology*, **43 (1)**, 170–181, https://doi.org/10.1175/1520-0450(2004)043<0170:TKCPAU>2.0.CO;2.

36. Lorenz, E. N., 1969: The predictability of a flow which possesses many scales of motion. *Tellus*, **21 (3)**, 289–307, https://doi.org/10.1111/j.2153-3490.1969.tb00444.x.

37. Marra, A. C., and Coauthors, 2019: The precipitation structure of the mediterranean tropical-like cyclone numa: Analysis of gpm observations and numerical weather prediction model simulations. *Remote Sensing*, **11 (14)**, https://doi.org/10.3390/rs11141690.

38. Mazza, E., U. Ulbrich, and R. Klein, 2017: The tropical transition of the october 1996 medicane in the western mediterranean sea: A warm seclusion event. *Monthly Weather Review*, **145 (7)**, 2575–2595, https://doi.org/10.1175/MWR-D-16-0474.1.

39. Miglietta, M., D. Mastrangelo, and D. Conte, 2015: Influence of physics parameterization schemes on the simulation of a tropical-like cyclone in the mediterranean sea. *Atmospheric Research*, **153**, 360–375, https://doi.org/10.1016/j.atmosres.2014.09.008.

40. Miglietta, M., A. Moscatello, D. Conte, G. Mannarini, G. Lacorata, and R. Rotunno, 2011: Numerical analysis of a mediterranean 'hurricane' over south-eastern italy: Sensitivity experiments to sea surface temperature. *Atmospheric Research*, **101**, https://doi.org/10.1016/j.atmosres.2011.04.006.

41. Miglietta, M. M., S. Laviola, A. Malvaldi, D. Conte, V. Levizzani, and C. Price, 2013: Analysis of tropical-like cyclones over the mediterranean sea through a combined modeling and satellite approach. *Geophysical Research Letters*, **40 (10)**, 2400–2405, https://doi.org/10.1002/grl.50432.

42. Miglietta, M. M., and R. Rotunno, 2019: Development mechanisms for mediterranean tropical-like cyclones (medicanes). *Quarterly Journal of the Royal Meteorological Society*, **145 (721)**, 1444–1460, https://doi.org/10.1002/qj.3503.

43. Mlawer, E. J., S. J. Taubman, P. D. Brown, M. J. Iacono, and S. A. Clough, 1997: Radiative transfer for inhomogeneous atmospheres: Rrtm, a validated correlated-k model for the

longwave. *Journal of Geophysical Research: Atmospheres*, **102 (D14)**, 16 663–16 682, https://doi.org/10.1029/97JD00237.

44. Moscatello, A., M. M. Miglietta, and R. Rotunno, 2008: Numerical analysis of a mediterranean "hurricane" over southeastern italy. *Monthly Weather Review*, **136 (11)**, 4373–4397, https://doi.org/10.1175/2008MWR2512.1.

45. NASA, 2019: Modis website. https://modis.gsfc.nasa.gov/.

46. NASA, 2019: Nasa website. https://www.nasa.gov/.

47. Nastos, P., K. Karavana-Papadimou, and I. Matsangouras, 2018: Mediterranean tropical-like cyclones: Impacts and composite daily means and anomalies of synoptic patterns. *Atmospheric Research*, **208**, 156–166, https://doi.org/10.1016/j.atmosres.2017.10.023.

48. NERC, 2019: Dundee satellite receiving station website. http://www.sat.dundee.ac.uk/.

49. NHC, and CPHC, 2019: Nhc track forecast cone. https://www.nhc.noaa.gov/aboutcone.shtml.

50. NOAA, 2020: Noaa website. https://www.noaa.gov/.

51. Picornell, M. A., J. Campins, and A. Jansà, 2014: Detection and thermal description of medicanes from numerical simulation. *Natural Hazards and Earth System Sciences*, **14 (5)**, 1059–1070, https://doi.org/10.5194/nhess-14-1059-2014.

52. Pytharoulis, I., G. C. Craig, and S. P. Ballard, 2000: The hurricane-like mediterranean cyclone of january 1995. *Meteorological Applications*, **7 (3)**, 261–279, https://doi.org/10.1017/S1350482700001511.

53. Pytharoulis, I., S. Kartsios, I. Tegoulias, H. Feidas, M. Miglietta, I. Matsangouras, and T. Karacostas, 2018: Sensitivity of a mediterranean tropical-like cyclone to physical parameterizations. *Atmosphere*, **9**, 436, https://doi.org/10.3390/atmos9110436.

54. Rasmussen, E., and C. Zick, 1987: A subsynoptic vortex over the mediterranean with some resemblance to polar lows. *Tellus A*, **39A (4)**, 408–425, https://doi.org/10.1111/j.1600-0870.1987.tb00318.x.

55. Raveh-Rubin, S., 2017: Dry intrusions: Lagrangian climatology and dynamical impact on the planetary boundary layer. *Journal of Climate*, **30 (17)**, 6661–6682, https://doi.org/10.1175/JCLI-D-16-0782.1.

56. Reale, O., and R. Atlas, 2001: Tropical cyclone–like vortices in the extratropics: Observational evidence and synoptic analysis. *Weather and Forecasting*, **16 (1)**, 7–34, https://doi.org/10.1175/1520-0434(2001)016<0007:TCLVIT>2.0.CO;2.

57. Rizza, U., and Coauthors, 2017: Wrf-chem model simulations of a dust outbreak over the central mediterranean and comparison with multi-sensor desert dust observations. *Atmospheric Chemistry and Physics*, **17**, 93, https://doi.org/10.5194/acp-17-93-2017.

58. Robert Houze, J., 2014: *Cloud Dynamics*, International Geophysics Series, Vol. 104. 2nd ed., Elsevier Science, 496 pp., https://doi.org/10.1016/B978-0-12-374266-7.00011-1.

59. Rotunno, R., and K. Emanuel, 1987: An air–sea interaction theory for tropical cyclones. part ii: Evolutionary study using a nonhydrostatic axisymmetric numerical model. *J. Atmos. Sci.*, **44**, 542–561, https://doi.org/10.1175/1520-0469(1987)044<0542:AAITFT>2.0.CO;2.

60. Shapiro, M. A., and D. Keyser, 1990: Fronts, jet streams and the tropopause. *Extratropical cyclones*, Springer, 167–191.

61. Skamarock, W. C., and Coauthors, 2019: A description of the advanced research wrf version 4. *NCAR Tech. Note NCAR/TN-556+STR*, 145 pp, https://doi.org/10.5065/1dfh-6p97.

62. Storer, L. N., P. D. Williams, and P. G. Gill, 2019: Aviation turbulence: Dynamics, forecasting, and response to climate change. *Pure and Applied Geophysics*, **176**, 2081–2095, https://doi.org/10.1007/s00024-018-1822-0.

63. Tous, M., and R. Romero, 2013: Meteorological environments associated with medicane development. *International Journal of Climatology*, **33 (1)**, 1–14, https://doi.org/10.1002/joc.3428.

64. WMO, 2020: Meteoterm. https://public.wmo.int/en/resources/meteoterm.

65. Zehnder, J. A., 2019: Tropical cyclone. https://www.britannica.com/science/tropical-cyclone.